The Effect of Shielding Gas Composition on Weld Bead Geometry during Short-circuit GMA Welding of Inconel625 Alloy

Yupeng Zhao

M.Sc. Thesis

August, 2016

The effect of shielding gas composition on the weld bead geometry during short-circuit GMA welding of Inconel625 alloy

By

Yupeng Zhao

in partial fulfilment of the requirements for the degree of

Master of Science
in Aerospace Engineering

at the Delft University of Technology,
to be defended publicly on Friday August 26, 2016 at 2:00 PM.

Student number:	4409620
Project duration:	October 19, 2015 - August 26, 2016
Thesis committee:	Prof. dr. S. van der Zwaag, TU Delft
	Dr. ir. M.J.M. Hermans, TU Delft
	Ir. M. Potjer IWE, Allseas Engineering B.V.
	Ir. J. Sinke, TU Delft

This thesis is confidential and cannot be made public until August 26, 2016.

TU Delft

Abstract

Recently, X65 carbon steel pipes internally clad with a thin Inconel625 alloy lining are highly used. However, during welding the Inconel625 lining in the root pass, the weld bead is uneven. To avoid weld defects in the successive passes, an additional grinding procedure is always required to flatten the weld bead. It is known that as an indispensable component in GMAW, the shielding gas can protect the liquid metal from oxidation and defects in the atmosphere. The shielding gas composition greatly determines the characteristics of the welding arc which plays a significant role in the heat, mass transfer during welding and flow motion in the weld pool. It is proposed that the uneven weld bead can possibly be improved by changing the shielding gas composition during welding the Inconel625 lining. Therefore, it is necessary to study the effect of shielding gas composition on the weld bead geometry during short-circuit gas metal arc welding (GMAW) of Inconel625 alloy.

In this research, short-circuit GMAW of the Inconel625 lining was reproduced in a laboratory scale. Three kinds of gas, argon (Ar), helium (He) and carbon dioxide (CO_2) were considered and two types of experimental configurations, bead-on-plate welding and U-shaped groove butt welding were performed. It was found that the shielding gas composition could make a great influence on the arc voltage, power of the heat source (welding arc), flow motion in the weld pool and the resultant geometry of the weld bead. For the Ar-He shielding gas mixtures, the arc voltage is increased as the He content is increased, which is attributed that the ionisation potential of He is higher than that of Ar. As a consequence, with an increase of the He content, the heat source (the welding arc) becomes more powerful and more heat is transferred to the workpiece. A larger fusion area is created. For the Ar-CO_2 shielding gas mixtures, it was found that adding 3.3% CO_2 to Ar could raise the arc voltage and lead to a more powerful welding arc. More importantly, the presence of oxygen which is dissociated from CO_2 can largely reduce the surface tension of the liquid metal. The temperature gradient of the surface tension can be changed from negative to positive and the direction of the Marangoni convection which is driven by the surface tension force will be changed from outward and upward to inward and downward. The efficiency of the heat transfer from the surface of the weld pool to the bottom is greatly enhanced. Consequently, addition of 3.3% CO_2 to Ar can deepen the penetration and enlarge the fusion area.

Acknowledgements

The wonderful journey in this lovely country comes to the end. I do believe that every piece of experience in the past two years will become my treasured memory. I think I will never forget the beauty of tulip fields, tranquillity of Giethoorn and fascination of the “girl with a pearl earring”. Besides, I feel really lucky to meet and work with such many kind and smart people. Without their help, I cannot finish my master study and this thesis smoothly. So, I would love to express my heartfelt gratitude to who have supported me through this journey.

At the beginning, many thanks are given to Rangan Dutta, He Gao and Mark Potjer, my supervisors in Allseas Engineering B.V. who offered me this interesting project and brought me to the field of welding technology. Especially my daily supervisor, Rangan Dutta, his professionalism, enthusiasm to work and intelligence leave me great impression.

I express my deep appreciation to Prof. Sybrand van der Zwaag and Dr. Marcel Hermans. With the extensive knowledge and deep understanding of welding, they taught me how to think the practical problems like a researcher, how to design appropriate experiments to explain them and how to analyse the experimental results to understand the mechanism lying behind them.

Then, I thank Jurriaan Slingerland and Sander van Asperen, the technicians in 3ME department who provided me much technical support in the laboratory. Special thanks are given to Prof. Ian Richardson who taught me the physics of arc welding. Up to now, I still enjoy the discussion with him about the helium arc plasma.

Last but not the least, I would love to express my great thanks for the support and encouragement from my parents, Wenqi Bi and Haiquan Zhao. I love you.

Yupeng Zhao

Delft, August 2016

Table of contents

List of figures

List of tables

Chapter 1. General introduction

1.1 Thesis description

In the aerospace, offshore, defence and transportation industries, application of Corrosion Resistant Alloys (CRAs) has rapidly grown. Due to superior corrosion resistance, CRAs protect metal assets in production, exploration, refineries, and processing plants against aggressive environments. In the offshore oil and gas industry, the CRA pipes are also serving a more and more important role. Recently, Allseas Engineering B.V. uses the X65 carbon steel pipes internally clad with a thin Inconel625 alloy (a kind of CRAs, more details in Section 2.5) lining to provide a highly economical alternative to the solid CRA pipes. In the pipeline production, multi-pass welding is performed. During welding the Inconel625 lining in the root pass, it is caused that the shape of the weld bead is uneven (Figure 1-1). In order to avoid weld defects in the successive passes, an additional grinding procedure is required to flatten the weld bead, which is expensive and time-consuming.

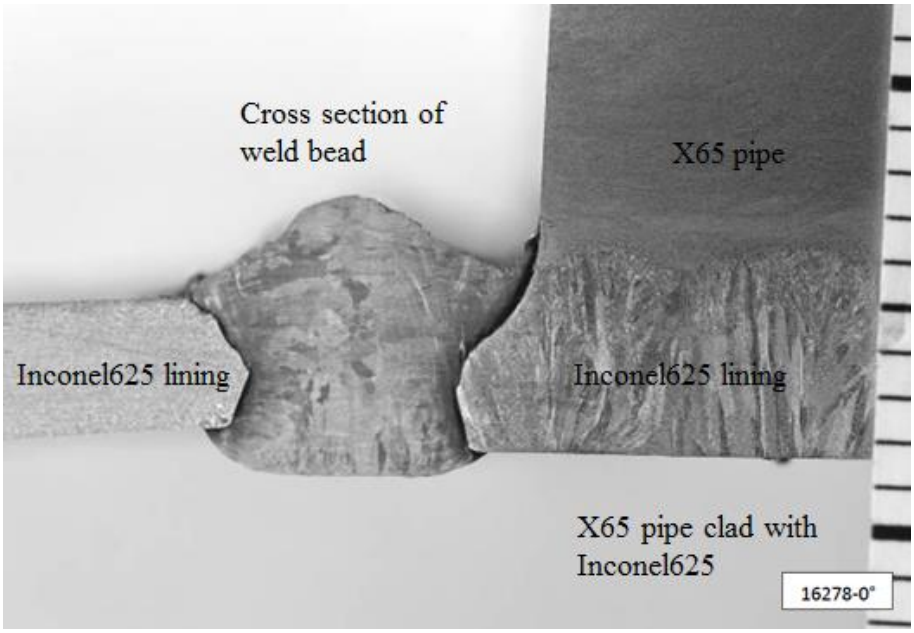

Figure 1-1 The cross section of the weld bead during welding Inconel625 lining in the root pass. This picture is provided by Allseas Engineering B.V..

Featuring a high material deposition rate and a high welding speed, gas metal arc welding (GMAW) is highly used in the pipeline construction [1, 2]. As an indispensable component in GMAW, shielding gas can protect the liquid metal from oxidation and defects in the atmosphere. The shielding gas composition greatly determines the properties of the welding arc which has a significant influence on heat transfer, metal transport and liquid flow motion in the weld pool during welding [3-7]. The resultant shape of the weld bead can be affected to some extent. Therefore, it is proposed whether the

uneven weld bead during the root-pass welding of the Inconel625 lining can be flattened by changing the shielding gas composition. If it works, the additional grinding procedure can be eliminated. To verify the feasibility of this approach, the effects of the different shielding gases on welding need to be revealed. In fact, extensive studies of the effects of the shielding gas on the welding arc, the liquid droplets transfer and the weld pool dynamics have been accomplished in the past decades. However, most of research was focused on welding steel and the effect of the shielding gas on welding Inconel625 alloy was limitedly investigated. Above all, it is necessary to carry out this research.

The highlight of this research focuses on three aspects. First of all, three kinds of shielding gases, argon (Ar), helium (He) and carbon dioxide (CO_2) are investigated. To sufficiently reveal the effects of these three gases, Ar, He and CO_2 should be studied separately. Secondly, during GMA welding of the Inconel625 lining the short-circuit metal transfer mode is employed. It should be mentioned that in GMAW, three metal transfer modes exist (short-circuit transfer, globular transfer and spray transfer) and the short-circuit metal transfer mode is characterised by a frequent contact between the welding wire and the workpiece. Unlike the relatively stable current and voltage in the globular transfer and the spray transfer, the welding current and voltage in the short-circuit mode is periodically changed which increases the complexity of research. Thirdly, welding the Inconel625 lining in offshore is reproduced in a laboratory scale. To realise it, two simplifications are made:

1) In practice, the pipes are welded in 5G position (pipes are fixed horizontally and welding is done overhead, vertical and flat with a full transition of all positions) (Figure 1-2). As the position is changed, the welding parameters keeps changing to maintain an optimal welding condition. For simplicity, only the twelve-o'clock location (the flat position) is reproduced. It is achieved by using the Inconel625 plates in the same thickness of the Inconel625 lining to simulate welding the pipes. The welding parameters used are the parameters specific to the twelve-o'clock location for welding the pipes.
2) As shown in Figure 1-1, the majority of the weld bead remains in the region of Inconel625 lining and the X65 pipe acts as heat sink in the root pass. During the butt welding experiments, a X65 metal block should be placed on the Inconel625 plate.

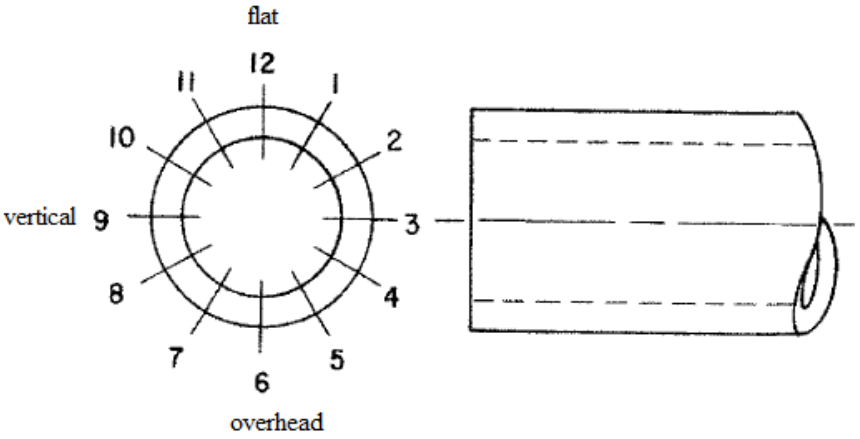

Figure 1-2 Schematic presentation of 5G welding [1, 2].

1.2 Research goals and approaches

The primary objective of this research is to study the effect of the shielding gas composition on the weld bead geometry during short-circuit GMAW of Inconel625 alloy. Three underlying questions emerge:

1) Whether the shielding gas composition can influence the welding parameters such as welding current, arc voltage and heat input and affect the short-circuit transfer parameters such as the short-circuit time, the arc time and the short-circuit frequency.
2) Whether the shielding gas composition can influence the thermophysical properties of the arc plasma, for instance of the electrical conductivity.
3) Whether the shielding gas composition can affect the flow motion of the liquid metal in the weld pool.

To address these questions, this research is carried out in three approaches. In the first step, to obtain a basic understanding of GMAW process, the preliminary bead-on-plate welding is performed. The shielding gas used is Ar and the wire feed rate is varied. It should be clarified that as a key welding parameter, the wire feed rate makes a significant influence on the manner of short-circuit metal transfer mode. Before investigating the shielding gas, the features of short-circuit GMA welding of Inconel625 alloy must be understood. In the second step, the bead-on-plate welding in He and the mixtures of Ar and CO_2 is carried out in the completely same welding conditions with that in the first step. After the second step, the effects of Ar, He and CO_2 on welding Inconel625 alloy can be generally disclosed. In the third step, the welding configuration is changed to the butt welding with a U-shaped groove, the dimension of which is the same with the Inconel625 lining of the pipe. In this step, the shielding gas composition is the unique variable and several gas mixtures are tested.

1.3 Outline of the thesis

The outline of the thesis is as follows. In chapter 2, the gas metal arc welding and its short-circuit metal transfer mode are described. The physics of arc plasma and the mechanism of the flow motion in the weld pool are introduced. Besides, a brief introduction of Inconel625 alloy is given. In chapter 3, the experimental procedure, equipment and the welding conditions are provided. In chapter 4, the results obtained from the experiments are presented. Chapter 5 mainly explains the experimental results and discusses the research questions. Finally, the general conclusions and recommendations for the future work are presented in chapter 6.

Chapter 2. Background

In this chapter, the fundamentals of gas metal arc welding and especially the short-circuit metal transfer mode are described. An introduction to the shielding gas, arc plasma and flow motion in the weld pool is provided. Besides, the basic information of Inconel625 alloy is presented.

2.1 Gas metal arc welding

Gas metal arc welding (GMAW), which is also known as metal inert gas (MIG) or metal active gas (MAG) welding, is being widely applied for joining metals in industry. In this process, an arc plasma is created between a continuously feed wire and a workpiece [3]. Both the arc plasma and the liquid weld pool are protected from the air by a shielding gas. During GMAW, the heat produced by the arc plasma and marginally by Joule heating of the electrode extension is consumed by melting the wire and the workpiece. The welding equipment and an enlarged welding area are schematically shown in Figure 2-1. It should be mentioned that for GMAW, a direct current is normally employed with a positive wire electrode (DCEP) [6].

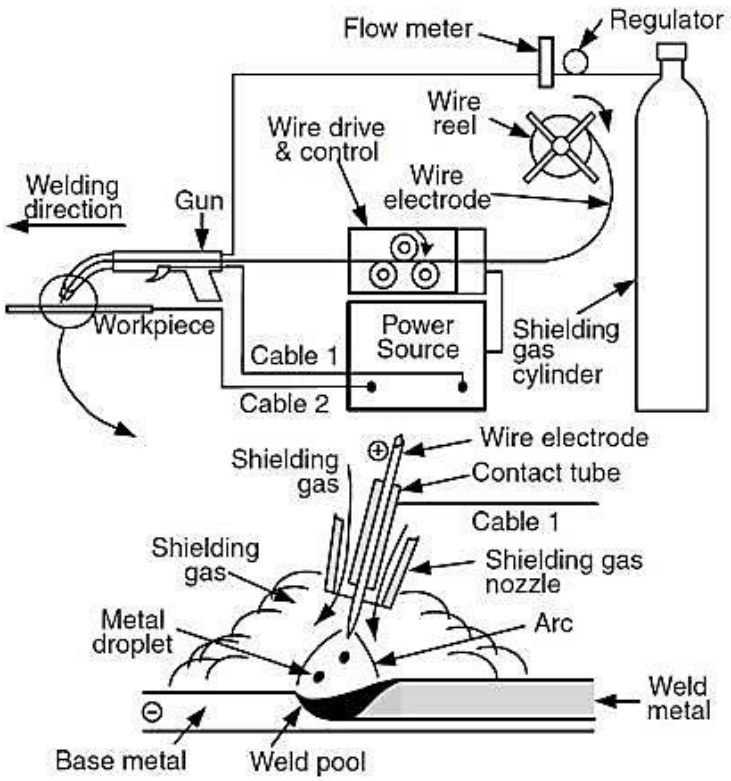

Figure 2-1 Schematic presentation of GMAW [6].

2.1.1 Principles of operation

A feature of GMAW is that the feed wire is deposited to the weld pool in the form of liquid droplets. The mode of the droplet transport mainly depends on welding conditions, especially the welding current and the arc voltage. Three major modes exist in GMAW which are the short-circuit transfer (also known as dip transfer), globular transfer, and spray transfer (Figure 2-2). In the case of a low welding current and a low arc voltage, the short-circuit transfer occurs [6]. It is characterised by a regular contact between the electrode and the workpiece. During the contact (the short-circuit period), the arc is extinguished and a liquid bridge is formed between the electrode and the workpiece. When the liquid bridge ruptures, the metal transfer is completed and the welding arc reignites. This marks the beginning of the arc period [1]. More details on short-circuit transfer are presented in Section 2.2.

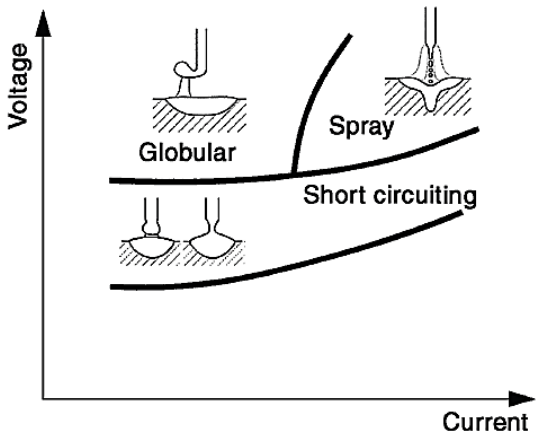

Figure 2-2 Schematic illustration of metal transfer modes in different welding conditions [8].

The globular transfer encompasses a low current but a high arc voltage. A large liquid droplet is formed at the tip of the electrode [9]. This feature can be attributed to a low wire feed rate and a long welding arc. The droplet is provided with the sufficient space to grow and is finally detached by gravity. Accordingly, spatter loss can be severe and the process stability is poor. The application of this transfer mode is very limited in practice [8].

When the current increases above a critical value (spray transition current), spray transfer occurs. In this mode, the small discrete droplets are formed and travel across the arc at a much higher frequency and speed relative to the globular transfer [9]. This transfer mode is stable and spatter free. The welding current and the arc voltage are in such a high level that the heat input is relatively high. The spray transfer is commonly used for welding thick sections [1]. To overcome the thickness limitation of the workpiece in the spray transfer, pulsed gas metal arc welding (P-GMAW) is designed. The welding current of this process is switched regularly between a low background current and a superimposed pulsing current (higher than the spray transition current) (Figure 2-3). The low

background current is used to sustain the arc, while the high pulsing current causes one or more droplets to be formed and transferred [10, 11]. Therefore, the stable spray transfer can be applied at a low average current level. Compared with the short-circuit transfer and the globular transfer, P-GMAW offers a much lower spatter level [12].

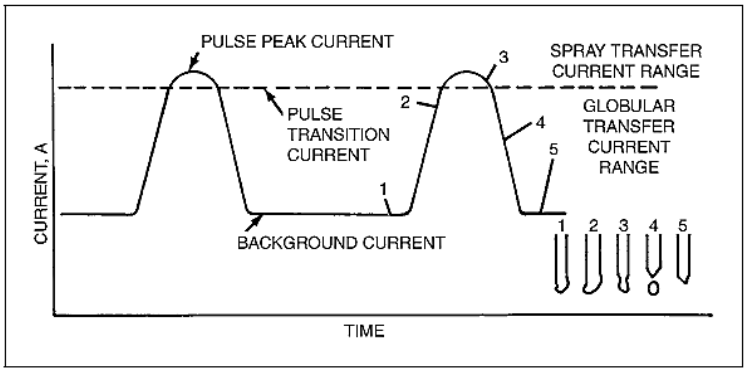

Figure 2-3 The current characteristics of Pulsed-GMAW [1].

2.1.2 Process variables

Wire feed rate

The amount of material deposited in the weld pool depends on the wire feed rate which is equal to the average wire melting rate under a stable welding condition. For various feeding wire, the empirical relationship between the wire feed rate and the average welding current has been obtained. For example of the 300-series stainless steel wire, it can be seen in Figure 2-4 that a positive correlation exists between the wire feed rate and the welding current. Moreover, a larger wire diameter requires an increased current when the wire feed rate is constant.

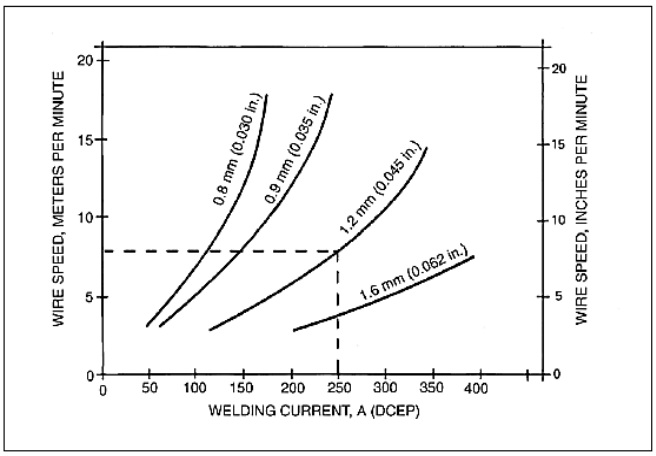

Figure 2-4 Burn-off characteristics for 300-series stainless steel wire [3].

However, it should be clarified that the welding current determines the wire melting rate (MR) rather than the wire feed rate. The relationship between the instantaneous MR and the instantaneous current can be expressed as [1]

$$MR = \alpha I + \frac{\beta l I^2}{a} \tag{2.1}$$

where I is the welding current (A), l is the electrode or wire extension (mm) (the distance between the end of the contact tip and the end of the electrode), a is the cross-section area of the wire (mm^2), α and β are constants. In equation 2.1, the first term is attributed to the arc heating effect and the second term represents the Joule heating of the electrode extension.

Arc voltage

A welding arc is developed between the feeding wire and the top surface of the workpiece. The voltage drop in the arc, termed arc voltage, greatly influences the amount of power input. It should be noted that arc voltage is nonlinearly distributed along the arc. It is commonly divided into three regions which are cathode sheath, arc column and anode sheath (Figure 2-5) [13]. The anode sheath and the cathode sheath are extremely thin but employing a high voltage drop. In practice, the arc voltage is bound up with the arc length, a critical parameter which should be carefully controlled. On the one hand, a long welding arc leads to large droplets forming at the tip of wire and the spatter loss can dramatically rise. On the other hand, an excessively short arc may cause the wire stubbing into the weld pool [3]. More details on the welding arc are provided in Section 2.3.

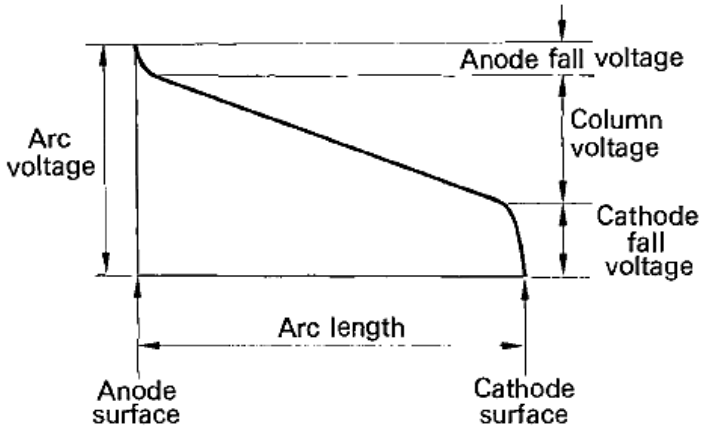

Figure 2-5 Schematic presentation of the anodic region, the arc column, and the cathodic region [13].

Travel speed and heat input

Travel/welding speed is the linear velocity at which the welding arc moves along the workpiece. Incorporating the travel speed with the welding current and voltage, the heat input (the amount of heat entering the workpiece per unit length of weld pool) to the joint can be calculated by [14]

$$\boldsymbol{H = \eta_p \cdot \frac{\int_0^{t_{weld}} U \cdot I \cdot dt}{D}} \tag{2.2}$$

where U is the arc voltage (V), I is the welding current (A), η_p is the efficiency of heat source, t_{weld} is the welding time (s) and D is the welding distance (mm). As the travel speed increases and other parameters are maintained, the heat input is reduced. A shallow penetration and a small fusion zone can be expected. On the contrary, if the travel speed is very low, the high heat input may cause the workpiece burned through [15-17].

Torch orientation and weld joint position

The welding torch can normally be fixed in three orientations, *i.e.* forehand (pushing), perpendicular and backhand (dragging) which can affect the weld bead geometry. Compared with the backhand welding, the forehand welding can produce a wider but shallower weld bead (Figure 2-6) [3]. Besides, several practical weld joint positions are tabulated in Table 2-1. Four basic welding positions are flat, horizontal, vertical and overhead. Welding the pipelines can experience the transition from one position to another due to its round shape [18].

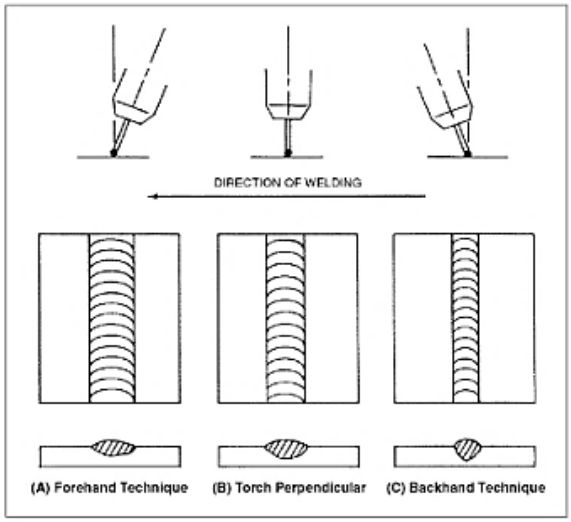

Figure 2-6 Influence of the torch orientation on the weld bead geometry [3].

Table 2-1 Welding positions for the plate and the pipeline [18].

Plate		Pipeline	
1	Flat position	1	Pipe is in horizontal position and rolled.
2	Horizontal position	2	Pipe is fixed in vertical position. Welding is done horizontally.
3	Vertical position	5	Pipe is fixed in horizontal position. Welding is done overhead, vertical, and flat with a full transition of all positions.
4	Overhead position	6	Pipe is fixed in 45^{o} position.
F	Fillet weld	R	Pipe is fixed in the restricted position.
G	Groove weld	F or G	Fillet or groove.

2.1.3 Shielding gas

In the presence of oxygen at high temperature, metal rapidly oxidises and defects such as slag inclusion and porosity can be caused. To protect the liquid metal from contaminants in the air, a shielding gas is applied. Besides, the shielding gas determines the thermophysical property of the welding arc which has a great influence on heat and mass transfer, weld bead geometry and the mechanical properties of the welds [7, 19-24]. The shielding gas composition is an important parameter in arc welding. Depending on material and dimension of the workpiece to be welded, argon, helium, carbon dioxide, and mixtures of them are frequently used [1]. Their basic properties are shown in Table 2-2.

Table 2-2 Basic properties of the shielding gases [25].

	Argon	Helium	Carbon Dioxide
Atomic number	18	2	-
Molecular weight (g/mol)	39.95	4.00	44.01
Density (kg/m^3) at 0°C and 1.01 bar, air=1.29	1.78	0.18	1.98
First ionisation energy (eV)	15.75	24.58	13.78

Approximately one percent of the atmosphere is composed of argon (Ar) which is colourless, odourless and nontoxic. Relative to other shielding gases, Ar can be easily ignited during welding due to a low ionisation potential and its inertness leads to no chemical reaction with metals. Hence, it commonly serves as the basic gas in the shielding gas mixture. Nevertheless, a disadvantage of using pure Ar as the shielding gas is the low heat flux to the workpiece [5, 26]. During welding the thick workpieces or metals with high thermal conductivity, lack of penetration may occur.

High heat input can be achieved by using helium (He) or mixture of Ar and He as the shielding gas. Compared with Ar, He generates a more contracted arc plasma with a higher power density [4, 5, 27, 28]. The main reason is that the ionisation potential of helium is much larger than that of argon. The higher ionisation potential requests a greater power input to ignite and sustain the arc plasma. Larger fusion area and a higher welding speed can be achieved [5]. However, in comparison with Ar, He is more expensive and due to its low density He requests a higher gas flow rate to ensure proficient shielding effect [3].

Carbon dioxide (CO_2) is chemically reactive at high temperature, which is mainly used in welding steel [6]. CO_2 molecules can dissociate and release carbon monoxide and free oxygen atoms. The dissociation energy is 5.5 eV [29]. The presence of oxygen substantially decreases the surface tension of the liquid metal. This can change the direction of the Marangoni convection to deepen the weld pool [30-32]. The high content of CO_2 can produce heavy welding fume and cause the airborne issue [3, 33]. Another shortcoming of using CO_2 is that the metal transfer can become irregular and severe spatter may arise [14, 34].

2.2 Short-circuit gas metal arc welding

Short-circuit gas metal arc welding (S-GMAW) encompasses a low range of welding current and voltage. The low heat input makes it mainly used for joining the thin sections, out-of-position welding and bridging root openings [3]. A feature of this process is the periodical contact between the feeding wire and the workpiece (Figure 2-7). During the arc period, the arc plasma is formed and the length decreases continuously for the reason that the wire is fed at a faster rate than it is melted. When the droplet on the tip of the electrode contacts the weld pool, the arc is extinguished and a liquid bridge emerges which marks the beginning of short-circuit period [35, 36]. The current rises immediately but the voltage descends to a low level. The liquid droplet is transported from the wire to the weld pool. The short-circuit period ends up with the explosive rupture of the liquid bridge and the arc reignites marking the arc period starts over [14].

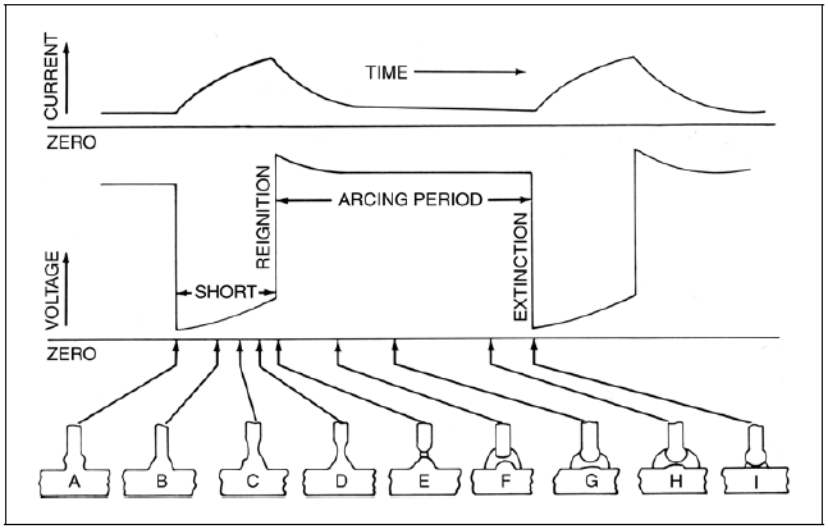

Figure 2-7 Schematic presentation of the short-circuit transfer [3].

2.2.1 Heat transfer

Heat transfer is an important aspect for welding. The amount of heat transferred from the heat source to the workpiece can have a great influence on the shape, microstructure and properties of the welds. In S-GMAW, both the arc heating and the Joule heating of the electrode extension serve as the heat source to melt the filler wire and the workpiece [14].

Heat flow in the electrode anode

In S-GMAW, the heat transferred to the anode comes from the arc heating and the Joule heating in the arc period and the Joule heating in the short-circuit period. This can be expressed as

$$\boldsymbol{Q_{electrode} = Q_{an-a} + Q_{r-a} + Q_{r-sc}} \tag{2.3}$$

where $Q_{electrode}$ is the total heat generated in the anode (J), Q_{an-a} is arc heating in the electrode anode (J), Q_{r-a} is the Joule heating in the arc period (J) and Q_{r-sc} is the Joule heating in the short-circuit period (J).

During the arc period, the arc heating is contributed by the heat generated in the anode sheath, thermal conduction from the arc column, the work function energy released by the electron condensation and the heat received from the hot electrons (Thomson effect) [7, 37, 38]. This can be expressed as

$$\boldsymbol{Q_{an-a} = \left[c_a U_{col} + U_a + \varphi_w + \frac{3k(T_{col} - T_a)}{2e}\right] \cdot I_a \cdot t_a \cdot f_s \cdot t_{weld}} \tag{2.4}$$

where c_a is the fraction of heat transferred from the arc column, U_{col} is the voltage drop of the arc column (V), U_a is the voltage drop of the anode sheath (V), φ_w is the work function of the anode metal (V), k is Boltzmann constant (J/K), T_{col} is the temperature of the arc column (K), T_a is the temperature of the anode (K), e is the charge of an electron (C), I_a is the average arc current (A), t_a is the average arc time (s), f_s is the average short-circuit frequency (Hz) and t_{weld} is the total welding time. During the arc period, the Joule heating can be calculated by

$$\boldsymbol{Q_{r-a} = U_w \cdot I_a \cdot t_a \cdot f_s \cdot t_{weld}} \tag{2.5}$$

where U_w is the average voltage drop through the wire extension in the arc period (V). During the short-circuit period, the Joule heating can be expressed as

$$\boldsymbol{Q_{r-sc} = U_{sc} \cdot I_c \cdot t_c \cdot f_s \cdot t_{weld}} \tag{2.6}$$

where U_{sc} is the average voltage drop through the wire extension in the short-circuit period (V), I_c is the average short-circuit current (A), and t_c is the average short-circuit time (s). It should be noted that the Joule heating also depends on the electrical resistance, diameter and the extension length of the filler wire.

Heat flow in the workpiece cathode

The heat source of the workpiece cathode includes the arc heating in the arc period and the energy carried by the arriving liquid droplets. The Joule heating of the workpiece can be neglected due to the low current density. This can be expressed as

$$\boldsymbol{Q_{workpiece} = Q_{ca-a} + Q_{droplets}} \tag{2.7}$$

where Q_{ca-a} is arc heating in the workpiece cathode (J) and $Q_{droplets}$ is the heat carried by the droplets (J).

During the arc period, the arc heating is contributed by the cathode sheath heating and thermal conduction from the arc column. Besides, a certain amount of energy is consumed by the emission of electrons (the work function) and elevating the temperature of electrons to the temperature of arc column [19, 38]. The arc heating can be expressed as

$$\boldsymbol{Q_{ca-a} = \left[c_c U_{col} + U_c - \varphi_w - \frac{3k(T_{col} - T_c)}{2e}\right] \cdot I_a \cdot t_a \cdot f_s \cdot t_{weld}} \tag{2.8}$$

where c_c is the fraction of heat transferred from the arc column, U_c is the voltage drop of the cathode sheath (V), φ_w is the work function of the anode metal (V), k is Boltzmann constant (J/K), T_{col} is the temperature of the arc column (K), and T_c is the temperature of the cathode (K). The heat carried by the droplets ($Q_{droplets}$) approximately equals the heat generated in the electrode ($Q_{electrode}$). It should be mentioned that the heat loss caused by the radiation and the influence of metal vapour from the wire and the weld pool is not considered in this study.

2.2.2 Metal transport

Metal transport is an important feature of GMAW and the transport manner can greatly affect the welding process and the quality of welds [39].

Droplets formation and transport

In short-circuit GMAW, the metal transport starts with the droplets being formed and pending on the tip of the electrode. Subsequently, the contact takes places between the droplet and the weld pool. The transportation ends up with the rupture of the liquid bridge. This process is governed by a balance of forces which are the surface tension force (F_γ), the electromagnetic force (also termed Lorentz force) (F_{em}), the gravity (F_g), the vapour jet force (F_V) and the viscous dragging force (F_d) by the shielding gas flow (Figure 2-8) [40-42].

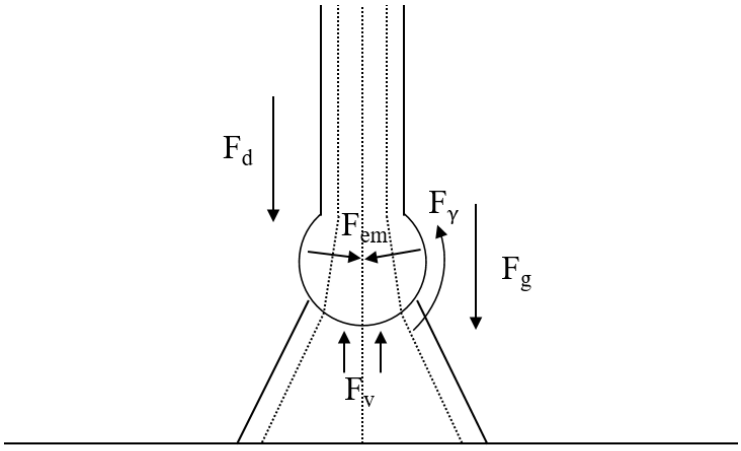

Figure 2-8 Forces on the droplets in GMAW [1].

During the arc period, the electromagnetic force, the gravity and the gas dragging force normally act as the detaching force, while the surface tension and the vapour jet force counteract the detachment. This relationship can be expressed as [1]

$$\boldsymbol{F_{em} + F_g + F_d - F_\gamma - F_V = 0} \tag{2.9}$$

During the short-circuit period, the inward component of the electromagnetic force squeezes the liquid bridge which becomes constricted gradually. This phenomenon is known as “the pinch effect”. In the final stage of this period, the surface tension turns to promote the droplets detaching.

The surface tension force plays a significant role in the metal transport and the weld pool dynamics. It can be given by [1]

$$\boldsymbol{F_\gamma = 2\pi r_w \gamma} \tag{2.10}$$

where r_w is the wire radius and γ is the surface tension. It should be noted that surface tension is temperature dependent and can be dramatically influenced by the surface active elements .

The welding current produces a magnetic field and the electromagnetic force is generated [43]. The force direction strongly depends on the current path (Figure 2-9). A contractive current distribution can change the axial component from downward to upward. The magnitude of this force can be calculated by [8]

$$\boldsymbol{F_{em} = \frac{\mu I^2}{4\pi} \ln \frac{r^2}{R}} \tag{2.11}$$

where μ is the magnetic permittivity of the wire material, I is the current, r and R are respectively the “exit” and “entry” radius of the current path.

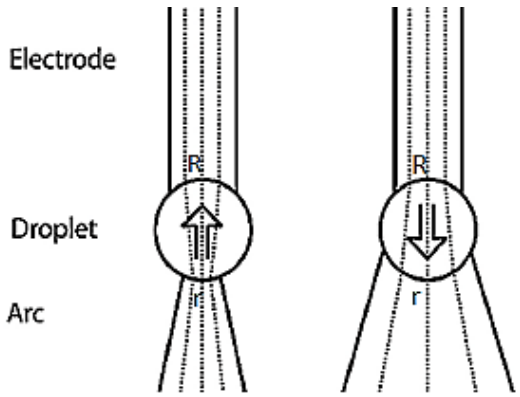

Figure 2-9 Influence of the current path on the electromagnetic force [8].

The gravity is given by the product of the droplet mass and the gravitational acceleration. Its direction relies on the welding torch orientation and the specific joint position. The vapour jet force is caused by the evaporation of the liquid droplet, which becomes remarkable at high current levels. Besides, the shielding gas flow can exert a dragging force on the pending droplet. Its magnitude depends on the gas velocity, density, and the droplet dimension. In S-GMAW, the vapour jet force and the aerodynamic dragging force are quite small and negligible [1].

Spatter generation

Spatter is an undesirable type of mass transport. In short-circuit GMAW, the spatter originates in the explosive rupture of the liquid bridge at the last moment of the short-circuit period. This is attributed to an abruptly increased welding current, *i.e.* a large dI/dt, which rapidly increases the electromagnetic pinch force. Severe spatter generation can induce lack of fusion, porosity in the weld bead and a turbulent shielding gas flow, which are detrimental to the weld quality. As an indication of the process stability, spatter loss must be limited [44].

2.3 Arc plasma

The welding arc is an electrical discharge between the negative cathode and the positive anode. In comparison with the dark discharge and glow discharge, arc discharge employs a higher current (>0.1 A) but a lower voltage (<100 V). In welding, the properties of the arc plasma strongly depend on the shielding gas composition and the welding parameters.

2.3.1 Basics of arc plasma

As one of the fundamental states of matters, plasma consists of unbound positive and negative particles [45]. Arc plasma can be divided into three regions, *i.e.* the cathodic region (also termed cathode sheath), the arc column, and the anodic region (also termed anode sheath) (Figure 2-5). The cathodic and anodic regions are extremely thin layers above the electrode surface where strong electrical fields are present. Due to the current contraction at the electrode surfaces, the current density is higher than that in arc column [46].

The cathodic region requires a flow of positive ions into it and the extraction of electrons from the outer shell of metal atoms (work function). Extra energy is consumed for heating the electrons. In arc welding, the voltage drop in the cathodic region (V_c) depends on the cathode material and the welding current [13]. The electrically neutral arc column consists of ions, electrons, and the neutral atoms and molecules in both excited and non-excited states. When the electrons travel across the arc column,

they strike the anode and release the kinetic energy and heat by condensation. The voltage drop in the anodic region which is mainly determined by the ionisation energy of the anode metal vapour is lower than that in the cathodic region [13, 47].

In the plasma, two gaseous chemical reactions, dissociation (if polyatomic molecules exist) and ionisation take place. As the gas temperature increases, the valence bonds are ruptured and the molecules are dissociated due to the severe rotation and vibration of atoms. With further increase in temperature, one or more outer electrons are prone to escape the electron bands making the atoms ionised. The energy level of ionisation is substantially higher than that of dissociation. For a specific gas, the plasma temperature and pressure determine the degree of dissociation and of ionisation [13]. It should be noted that when the degree of ionisation is larger than 1%, the plasma is considered to be highly ionised [13]. In arc welding a highly ionised plasma is the case.

As the plasma is at atmosphere pressure, a locally quasi-thermodynamic equilibrium exists where the temperature of electrons is close to the gas temperature. In other words, the arc temperature is unique in each point of the plasma [7, 48]. With a flow of positive and negative particles, the arc plasma comes down to a process of thermal diffusion [49], which can be characterised by the transport coefficients such as thermal conductivity, electrical conductivity and viscosity.

2.3.2 Comparison among Ar, He and CO_2 arc plasma

As mentioned in section 2.1.3, the thermophysical properties of the welding arc can be greatly affected by the shielding gas composition. In this part, a comparison is made among Ar, He and CO_2 arc plasma.

Ar-He arc plasma

The thermophysical properties of the Ar-He arc plasma are presented in Figure 2-10 [4]. In Figure 2-10 a, the specific heat is plotted as a function of temperature. It can be seen that the specific heat of the ionised gas is increased with the He content. This is because the specific heat can be greatly increased by ionisation and the ionisation energy of He is much higher than that of Ar [13].

The electrical conductivity (Figure 2-10 b), thermal conductivity (Figure 2-10 c) and viscosity (Figure 2-10 d) of the Ar-He gas mixtures were also assessed [27, 50]. It was found that at temperature below 22000 K, the electrical conductivity is reduced as the He content is elevated. However, at temperature above 22000 K, the case is opposite. This is attributed that at low temperature, the ionisation degree of He is much lower than that of Ar. As for the thermal conductivity and viscosity, a higher helium

content can lead to a greater value. It should be mentioned that the high thermal conductivity of He makes the energy more uniformly distributed in the He arc plasma.

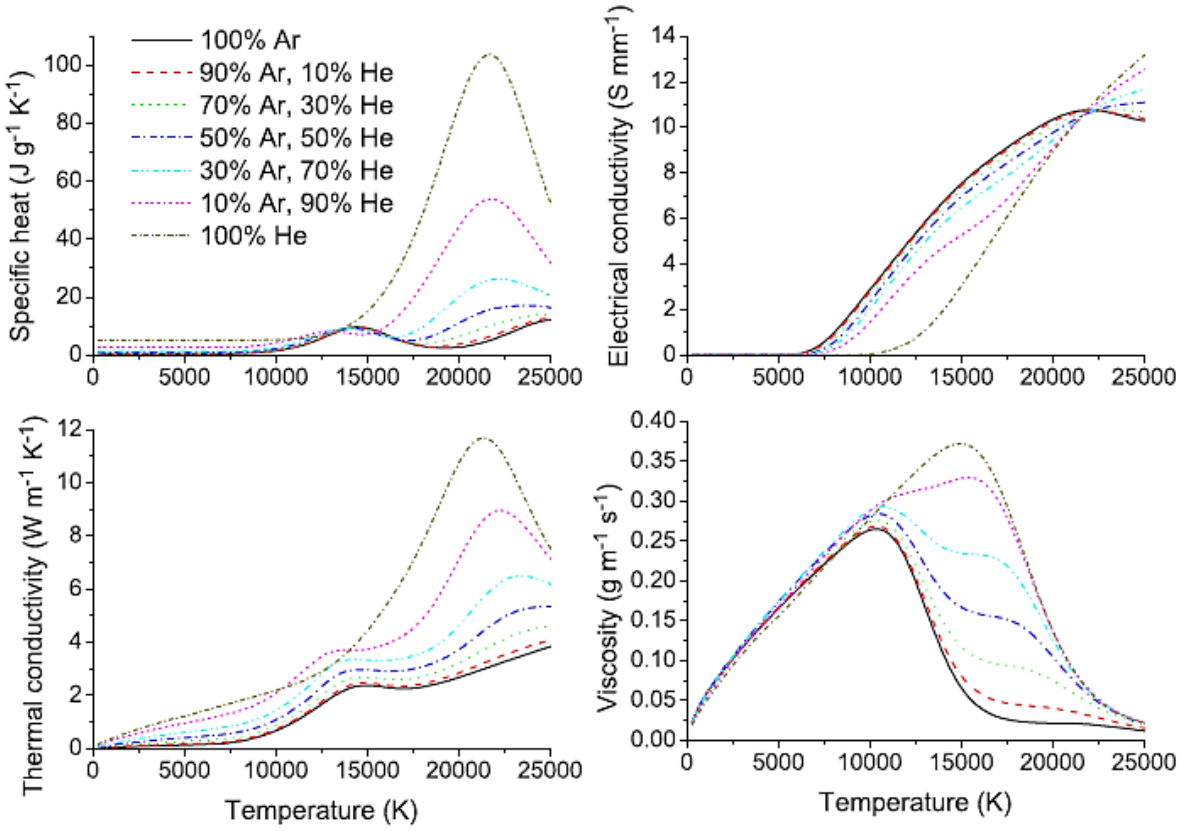

Figure 2-10 The thermophysical properties of the argon-helium mixtures. (a) The specific heat; (b) electrical conductivity; (c) thermal conductivity; (d) viscosity. The data were calculated under a pressure of 101.3 kPa [4, 27].

By using TIG welding and the water-cooled copper workpiece, the arcs in the argon-helium mixtures were compared (Figure 2-11) [4]. It can be seen that with the same arc length and welding current, an increased helium content leads to higher arc voltage and temperature. Besides, compared with the argon arc, the helium arc is more constricted. This can be explained by the "thermal pinch" effect [28]. It is argued that an increased enthalpy h results in a decreased arc cross-section area A. At the axial position, the enthalpy of the plasma is close to the product of the welding current I and arc voltage V. A relationship is proposed as [4]

$$\boldsymbol{IV = \rho h v A} \tag{2.12}$$

where ρ is density, v is the plasma velocity. It is noted the specific heat C_p is equivalent to the enthalpy due to $C_p = \partial h/\partial T$. Compared with argon, the higher specific heat of helium makes the arc

cross-section area smaller. This result is in agreement with Nemchinsky who reported that compared with in argon, the arc constriction in helium should be stronger [51].

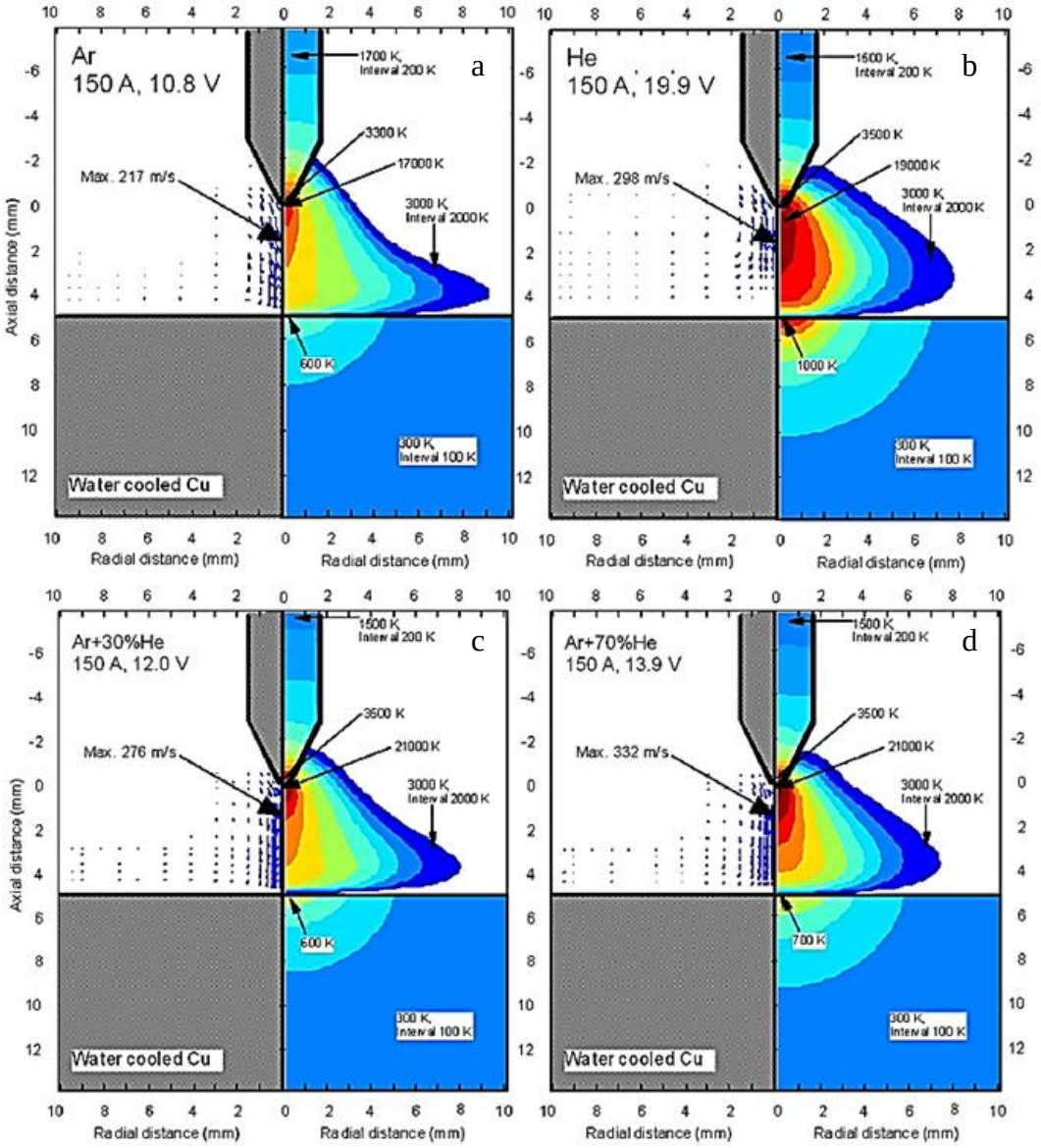

Figure 2-11 Temperature fields for the argon-helium arc plasma. (a) Ar; (b) He; (c) Ar+30% He; (d) Ar+70% He [4].

Ar-CO_2 arc plasma

The arc plasma of the argon-CO_2 mixtures in GMAW were investigated [32, 52]. The thermophysical properties of the gas mixtures are provided in Figure 2-12. As the CO_2 content is increased, the specific heat is raised. It is because as the temperature is increased, CO_2 molecules can dissociate which costs energy. The arc voltage in a high CO_2 content is higher than that in Ar. Due to the

"thermal pinch" effect, the presence of CO_2 produces a contractive arc which can lead to a high current density.

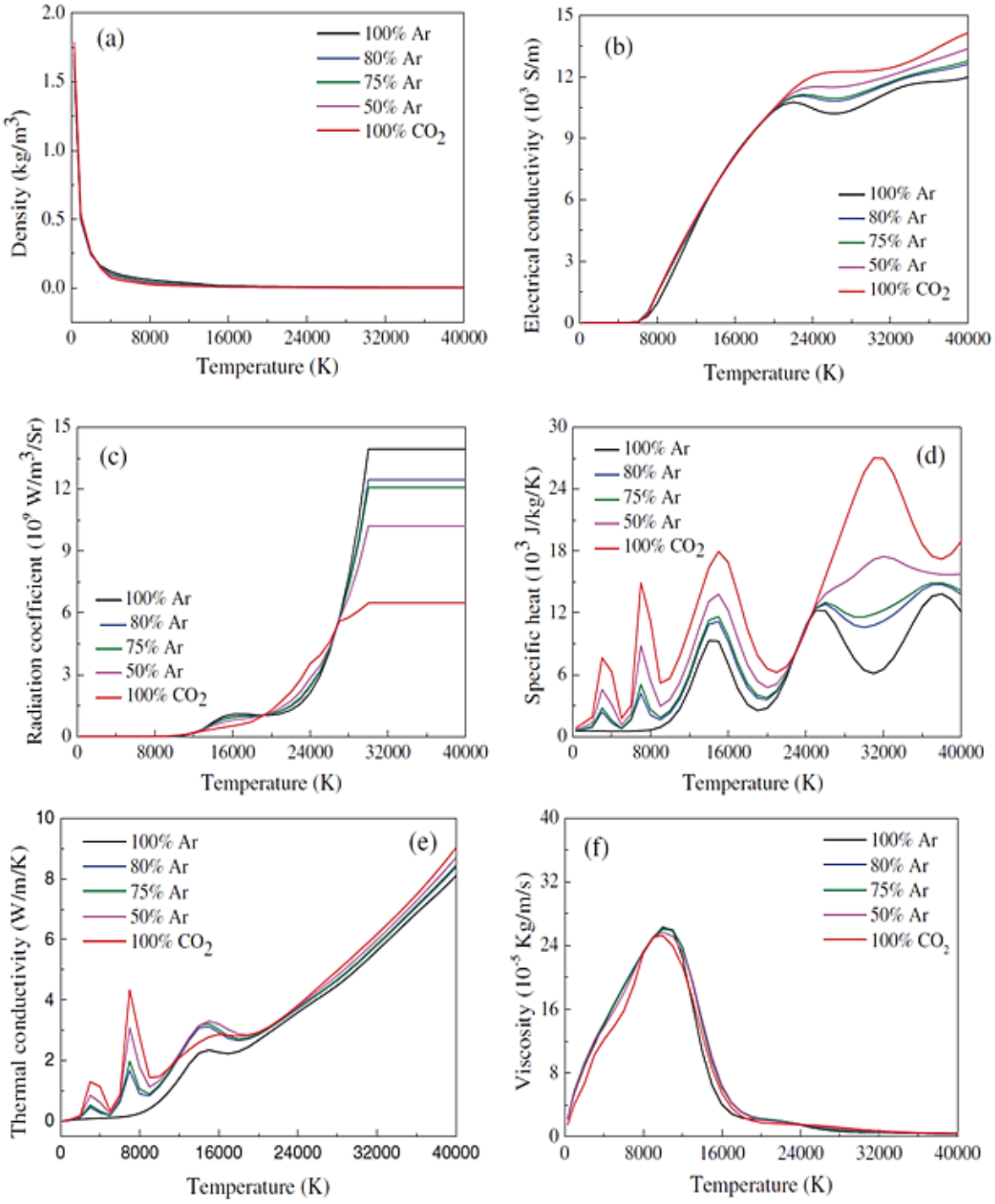

Figure 2-12 Thermophysical properties of the Ar-CO_2 gas mixtures. (a) Density; (b) electrical conductivity; (c) radiation coefficient; (d) specific heat; (e) thermal conductivity; (f) viscosity [32].

2.4 Fluid flow in the weld pool

When heat is transferred from the welding arc to the workpiece, the base metal is melted and a weld pool is created. The heat reaching the workpiece is dissipated through conduction and convection. In the weld pool, flow of the liquid metal occurs which plays a significant role in transferring the energy from the surface of weld pool to the bottom [53-57]. This process is driven by a balance of forces, *i.e.* buoyancy, electromagnetic force, surface tension force, and shear stress by arc plasma [58, 59]. In GMAW, the droplets impingement also makes a contribution [60]. The dynamics in the weld pool can greatly influence the heat distribution and geometry of the solidified weld bead. In this section, the mechanism for the weld pool dynamics is briefly described.

2.4.1 Driving forces

Buoyancy

Buoyancy can propel the liquid to fall along the weld pool boundary and rise along the central axis (Figure 2-13 a and b). This is caused by a density gradient in the weld pool. The closer to the pool boundary, the cooler the liquid is. Since a high temperature leads to a low density, the heavy liquid on the boundary tends to sink to the central bottom, while the low-density liquid is forced to move upwards [6, 61]. The magnitude of buoyancy can be calculated by [62]

$$\boldsymbol{F_b = \rho g \beta (T - T_0)} \tag{2.13}$$

where ρ is the density of liquid metal, g is the gravity acceleration, β is the thermal expansion coefficient, T is the temperature of the liquid metal, and T_0 is the reference temperature. Eisazadeh *et al.* [63] investigated the effect of buoyancy on the weld bead geometry. It was found the buoyancy-driven convection can produce a wide but shallow weld pool. When the welding current is greater than 100A, the buoyancy becomes much smaller than the electromagnetic force and the surface tension force.

Electromagnetic force

When an electric current passes through the workpiece, a magnetic field and the electromagnetic force (also termed the "Lorentz force") are induced. The electromagnetic force $\vec{F}_{em}$ can be expressed as [62]

$$\boldsymbol{\vec{F}_{em} = \vec{J} \times \vec{B}} \tag{2.14}$$

where $\vec{J}$ is the current density vector and $\vec{B}$ is the magnetic flux vector in the weld pool. According to the left-hand rule, the force direction is inward and downward. The liquid is pushed down along the pool axis and rises along the pool boundary (Figure 2-13 c and d). If the welding current is very high, the electromagnetic force can dominate the flow motion. A deep but narrow weld pool can be expected [64].

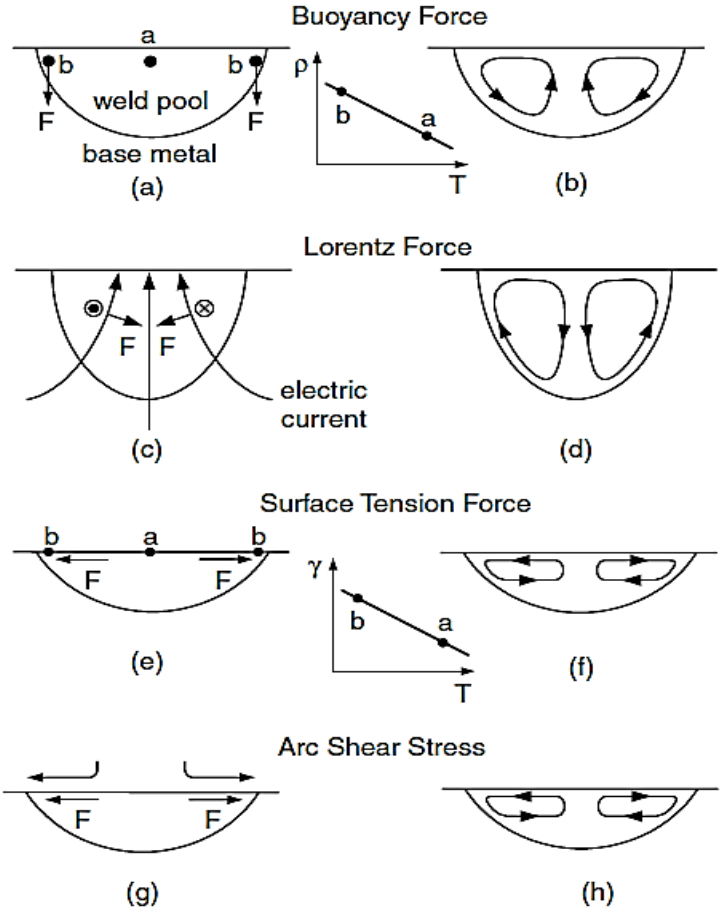

Figure 2-13 The driving forces for the weld pool convection: (a, b) buoyancy; (c, d) electromagnetic force; (e, f) surface tension; (g, h) shear stress caused by arc plasma [6].

Surface tension force

The surface tension force τ (also termed the Marangoni force) can greatly influence the liquid convection in the weld pool [65]. This force is attributed to a surface tension gradient along the surface of weld pool. The surface tension γ of a pure liquid metal decreases with the increasing temperature, *i.e.* $\partial\gamma/\partial T < 0$. The liquid with a high surface tension pulls the surrounding more strongly than the liquid with a low surface tension [6]. Consequently, the liquid on the surface tends to flow from centre (the low-surface-tension region) to periphery (the high-surface-tension region) (Figure 2-13 e and f).

This circulation is called the Marangoni convection [30, 66]. The surface tension force τ can be described by [67]

$$\boldsymbol{\tau = \frac{\partial \gamma}{\partial T}\frac{\partial T}{\partial r} + \frac{\partial \gamma}{\partial C}\frac{\partial C}{\partial r}} \quad (2.15)$$

Where T is the temperature, r is the distance along the surface from the heat source, and C is the concentration of surface active elements. In equation 2.15, the first term indicates the influence of temperature on the surface tension while the second term indicates the influence of the surface active elements. For a pure liquid metal, $\partial C/\partial r$ is zero and the second term can be neglected. The effect of surface active elements is introduced in section 2.4.2.

Shear stress and arc pressure induced by plasma jet

The plasma moves outward at a high speed along the surface of the weld pool. An outward shear stress is exerted on the pool surface and causes the liquid metal to radially flow from the pool centre to the edge (Figure 2-13 g and h). The arc pressure on the surface of weld pool is generated by the impingement of the plasma jet. High arc pressure can strongly depress the pool surface and deepen the welding penetration [68].

Droplets impingement

In GMAW, when a droplet carrying heat reaches the surface of weld pool, it tends to push surrounding fluid away and sink. The droplets impingement can make the heat transfer more efficiently from the surface of weld pool to the bottom [60].

2.4.2 Surface active elements

Besides temperature, the surface active elements (*e.g.*, O, S, Se, Te) have a strong influence on the Marangoni convection [69-74]. These elements can change the temperature coefficient of surface tension ($\partial\gamma/\partial T$) from negative to positive. The direction of the Marangoni convection is changed from outward to inward (Figure 2-14). In practice, these surface active elements can be added in two approaches. One is through the addition of oxide particles (*e.g.*, TiO, TiO_2, Al_2O_3, SiO_2, Fe_2O_3) [75]. This can be achieved by using the doped feeding wire or smearing the active flux on the surface of the joint. The other way is to mix the reactive gas (*e.g.*, CO_2, O_2) in the shielding gas during welding [76].

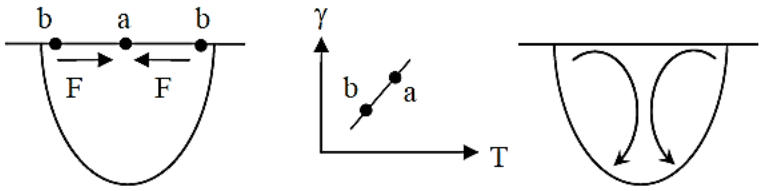

Figure 2-14 The inward flow caused by the positive temperature coefficient of surface tension [67].

The surface tension in the iron-oxygen system is quantified (Figure 2-15) [31, 77]. It is found that without oxygen, the surface tension of the liquid metal is reduced as the temperature is increased, *i.e.* the temperature gradient $\partial\gamma/\partial T$ is negative. The direction of liquid flow in the weld pool is outward and upward. With 0.03 wt.% oxygen in the Fe-O system, $\partial\gamma/\partial T$ becomes positive at temperature below 2240 K, *i.e.* the temperature gradient $\partial\gamma/\partial T$ is positive, while at temperature above 2240 K, the temperature gradient $\partial\gamma/\partial T$ is still negative. Consequently, if the maximal temperature of the weld pool is lower than 2240 K, an inward and downward flow will appear which can result in a deep but narrow weld pool. If the maximal temperature of the weld pool is higher than 2240 K, a double-cell convection with an outward, upward flow inside and an inward, downward flow outside will appear.

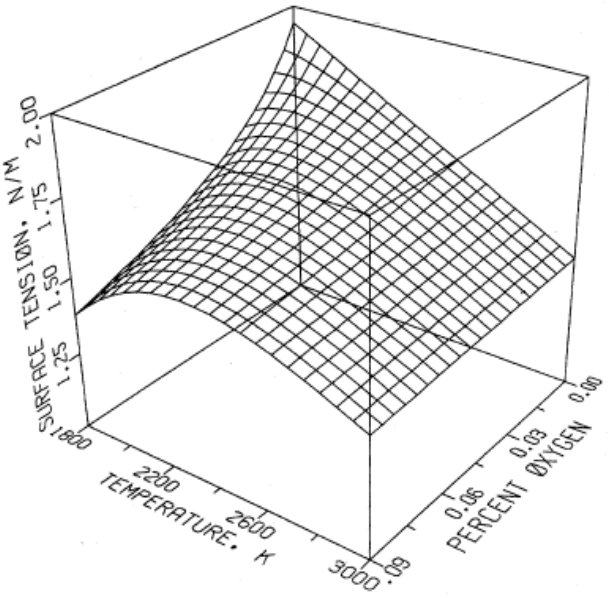

Figure 2-15 The surface tension of Fe-O system as a function of temperature and oxygen concentration [77].

2.5 Inconel625 alloy

Known for the outstanding corrosion resistance, nickel-chromium alloy 625 (Inconel625) is being widely used in the offshore, aerospace, defence and transportation industries. Inconel625 is a solid-solution alloy with the face-centred-cubic (FCC) structure. The chemical composition is shown in Table 2-3. Due to a high solubility in nickel (Ni), chromium (Cr) is the most important alloying element in many Ni-base alloys. A dense passive Cr_2O_3 layer is formed on the alloy surface to protect it against the aggressive environment. A small amount of molybdenum (Mo) is added to enhance the resistance to the pitting and crevice corrosion.

The melting temperature of Inconel625 alloy is 1290~1350 ℃. After welding, the solidification starts with the Ni-rich FCC austenite γ phase. As the temperature decreases, the solubility of Cr and Mo in Ni reduces and the intermediate compounds such as σ and P phases can be formed. Various carbides may appear in the form of MC, M_6C, and $M_{23}C_6$. Besides, niobium (Nb) can strengthen the alloy by the precipitation of the γ-Ni_3Nb phase. The presence of these phases has a great influence on the mechanic properties of Inconel625 alloy and thus the welding process requires a careful control [78].

Table 2-3 The chemical composition of Inconel625 alloy [41].

wt%	Ni	Cr	Mo	Fe	Nb	C	Mn	Si	Al
Alloy 625	58 min	20~23	8~10	5 max	3.15~ 4.15	0.1 max	0.5 max	0.5 max	0.4 max

Chapter 3. Experimental procedure

In this chapter, the experimental materials, setup and procedure are provided. To obtain the general characteristics of short-circuit GMA welding of Inconel625 alloy, bead-on-plate welds were made. Then, as an approach to welding Inconel625 lining offshore, butt welding with a U-shaped groove was carried out. With the shielding gas composition changed, the welding current and the welding voltage were monitored and the cross-section geometry of the weld bead was inspected.

3.1 Materials and consumables

The bead-on-plate welding were carried out on Inconel625 plates with the dimension of 200×75×3 mm^3. An Inconel625 wire with a diameter of 1.0 mm was used as the consumable welding wire. The chemical composition of the Inconel625 plates and wire is listed in Table 2-3. The butt welding were performed on Inconel625 plates (200×75×3 mm^3) which were milled a U-shaped groove on the long edge and tack welded on both ends (Figure 3-1). The industrially pure Ar, He, CO_2 and their mixtures were used as the shielding gas.

Figure 3-1 The tack welded workpiece in the butt welding.

3.2 Welding experiments

3.2.1 Welding system

A schematic representation of the welding setup is shown in Figure 3-2. A constant-voltage power source (Fronius™ Transpuls Synergic 5000) (Figure 3-3 a) was operated in the GMAW Standard Manual mode. The welding wire was supplied by the Fronius VR 7000 wire feeder (Figure 3-3 b) and

the RCU 5000i remote controller (Figure 3-3 c) was connected with the power source to adjust the welding parameters. Before welding, the gases were firstly injected into a mixing chamber (Figure 3-3 d). The flow rate of each gas indicated on the flowmeters can be adjusted to obtain a uniform gas mixture with a certain composition (volume fraction, %). A total gas flow rate of 15 l min^{-1} was kept constant. During welding, the signals of current and voltage were recorded by an oscilloscope.

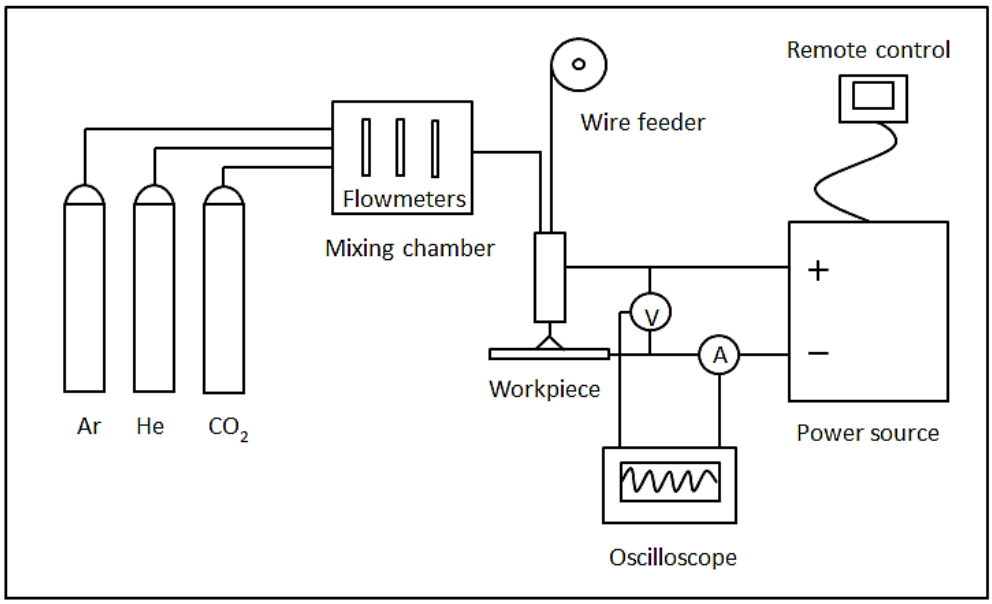

Figure 3-2 Schematic presentation of the experimental setup.

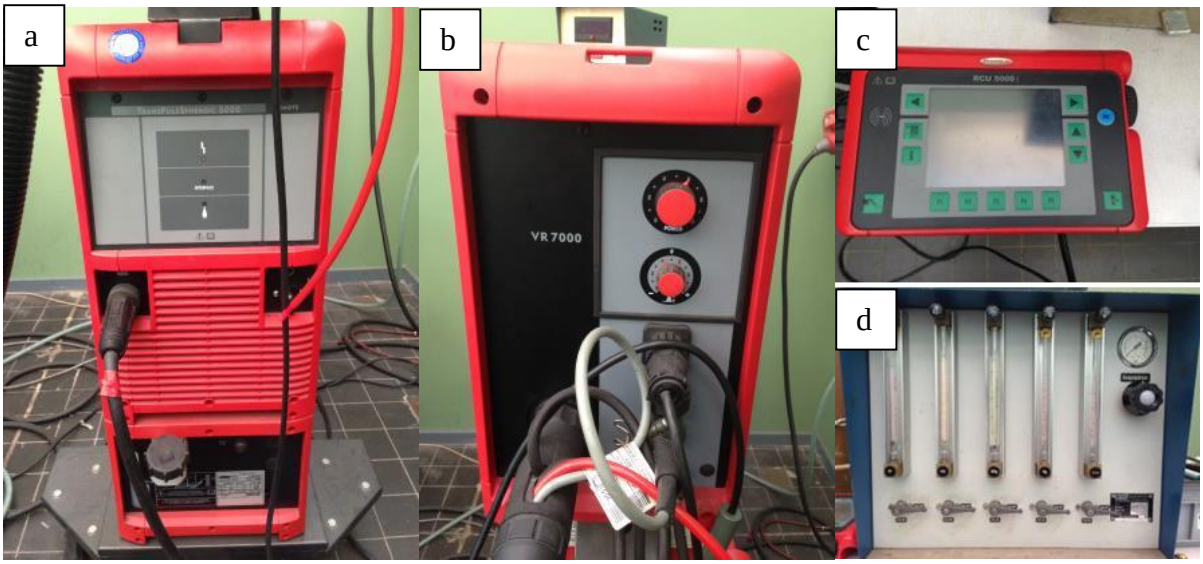

Figure 3-3 (a) Fronius™ Transpuls Synergic 5000 power source; (b) VR 7000 wire feeder; (c) RCU 5000i remote controller; (d) Mixing chamber with flowmeters.

3.2.2 Bead-on-plate welding

Configuration

The configuration of the bead-on-plate welding is presented in Figure 3-4. The Inconel625 plate was clamped and supported by a steel backing plate.

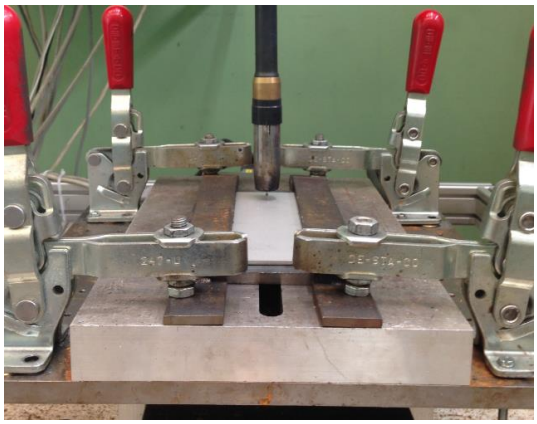

Figure 3-4 The configuration of bead-on-plate welding.

Welding conditions

Table 3-1 provides the fixed welding conditions in this configuration. The experimental variables are shown in Table 3-2. Four shielding gas compositions (Ar, He, Ar+3.3% CO_2 and Ar+6.7% CO_2) were used. For Ar and He, the wire feed rate was increased gradually from 6 to 9 m min^{-1}. It should be stated that as a critical welding parameter, the wire feed rate can greatly affect the GMAW process. To obtain the general features of welding Inconel625 alloy in the short-circuit transfer mode, the effect of the wire feed rate on the short-circuit manner is necessary to elucidate. Then, the results under different gas compositions but in the same welding conditions (including the wire feed rate) were compared. The total gas flow rate is lower than that during the offshore production (30 l min^{-1}).

Table 3-1 The fixed welding conditions of the bead-on-plate welding.

Metal transfer mode	Short-circuit transfer
Voltage setting [V]	17.3
Travel speed [mm s^{-1}]	4.3
Total gas flow rate [l min^{-1}]	15
Standoff distance [mm]	10
Contact-tube-to-workpiece distance [mm]	15
Gas pre-flow time [s]	2
Gas post-flow time [s]	2

Table 3-2 The experimental variables of the bead-on-plate welding.

Group number	Shielding gas composition (volume fraction, %)	Wire feed rate [m min^{-1}]
1	Ar	6
		7
		8
		9
2	He	6
		7
		8
		9
3	Ar+3.3% CO_2	8
4	Ar+6.7% CO_2	8

3.2.3 U-groove butt welding

Configuration

The presentations of the butt welding configuration are shown in Figure 3-5 a and b respectively. The tack welded Inconel625 workpiece was clamped and supported by two steel plates. A ceramic backing strip was placed under the U-shaped groove. Two metal blocks used as the heat sink were placed on the workpiece. The dimension of the U-shaped groove which is provided in Appendix A is the same with that of the Inconel625 lining in the pipe. It should be mentioned that there is a 2-mm gap between the workpiece and the ceramic backing. The reason for this design is that as stated in section 2.4, the presence of oxygen in CO_2 can change the direction of the Marangoni flow from outward to inward which induces a strong downward flow from the top surface to the bottom. If the backing is tightly attached on the bottom of the workpiece to block the liquid flow, it is difficult to identify the effect of CO_2.

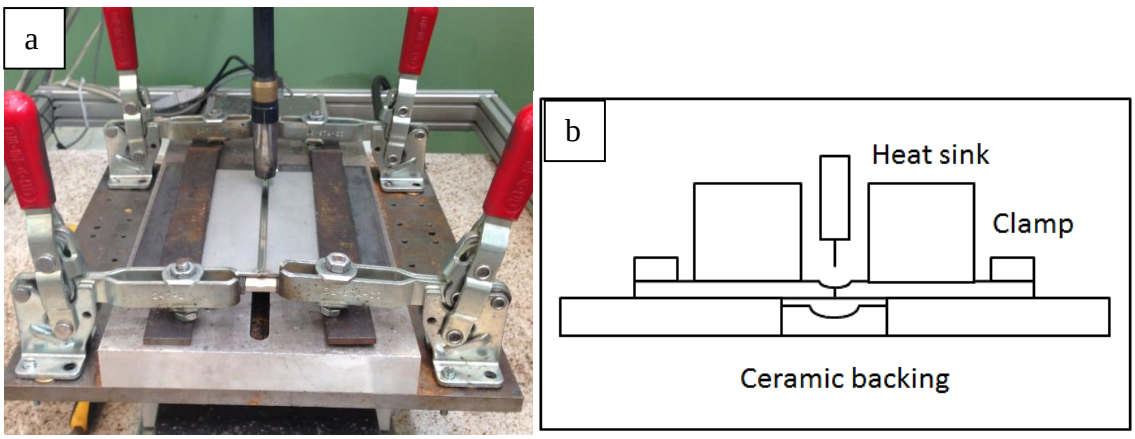

Figure 3-5 The configuration of butt welding. (a) Physical presentation; (b) schematic presentation.

During the offshore welding of the pipelines, a copper backing ring is used. To completely reproduce the practical welding, the butt welding with a tightly attached copper backing was also performed, the results of which are provided in Appendix B.

Welding conditions

The welding conditions are listed in Table 3-3 and Table 3-4. The shielding gas composition is the unique variable in the butt welding and eight compositions were used.

Table 3-3 The fixed welding conditions of the U-groove butt welding.

Metal transfer mode	Short-circuit transfer
Wire feed rate [m min^{-1}]	6
Voltage setting [V]	13
Travel speed [mm s^{-1}]	4.3
Total gas flow rate [l min^{-1}]	15
Standoff distance [mm]	10
Contact-tube-to-workpiece distance [mm]	15
Gas pre-flow time [s]	2
Gas post-flow time [s]	2

Table 3-4 The experimental variables of the U-groove butt welding.

Group number	Shielding gas composition (volume fraction, %)
1	Ar
	Ar+20% He
	Ar+40% He
	Ar+60% He
	Ar+80% He
	He
2	Ar+3.3% CO_2
	Ar+40% He+3.3% CO_2

3.3 Logging of electrical welding signals and temperature

By using an oscilloscope (DL750 ScopeCorder YOKOGAWA) (Figure 3-6 a), the welding current and voltage were collected with a measuring time of 10 s and a sampling frequency of 1 kHz during all welding experiments. The measurement accuracy of the DL750 oscilloscope is $\pm 0.25\%$. The welding current was measured by an ampere meter (Pico AC/DC Current Clamp) (Figure 3-6 b). The measurement accuracy of the ampere meter is $\pm(2\% \, reading + 2 \text{ A})$. It should be noted that the voltage which is measured between the contact tube and the workpiece is the sum of the voltage drop across the arc plus the drop in the electrode extension. Due to a high accuracy of the voltage

measurement, the error ($\pm 0.25\%$) is negligible. However, for the current measurement, the error is considerable and the error bar is inserted.

Besides, during the bead-on-plate welding, the temperature of the bottom surface of the workpiece is measured for the cases of Ar, He and Ar+3.3% CO_2 at the wire feed rate of 8 m min^{-1}. The measurement is done by means of an oscilloscope (DL750 ScopeCorder YOKOGAWA) connected with a K-type thermocouple (OMEGA). The thermocouple is attached on the bottom surface of the workpiece straight under the centre of the weld pool. The measurement lasts for 300 s with a sampling frequency of 20 Hz. The error of the K-type thermocouple is ± 2.2 ℃.

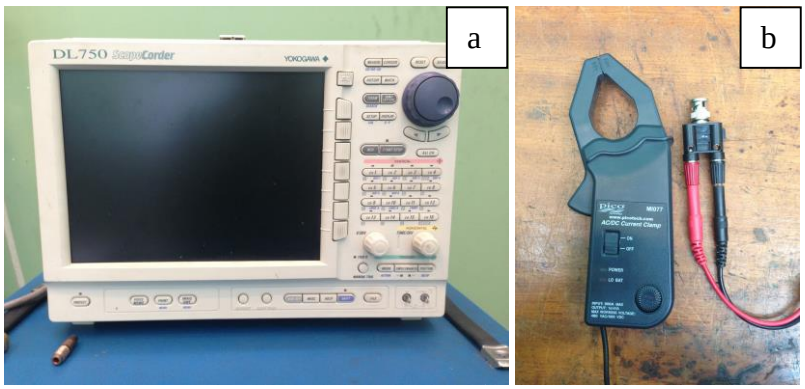

Figure 3-6 (a) DL750 ScopeCorder YOKOGAWA oscilloscope; (b) Pico AC/DC Current Clamp.

3.4 Weld bead geometry and optical microscopy

The weld cross-sections were obtained by transversely cutting the weld bead and embedding the samples in the DuroFast thermosetting epoxy resin. The samples were ground from 80 to a 2000 grit finish and polished to 1 µm. Then, by using the "Waterless Kalling's" etchant (5 g of copper chloride dissolved in a solution of 100 ml of hydrochloric acid and 100 ml of ethanol), the samples were immersed and etched for about 15 s. By means of the VHX-5000 KEYENCE optical microscope, the macrostructures of the samples were observed and the dimensions of the weld bead cross-sections were measured. Each cross-section was measured for three times to reduce the measuring error.

During measuring the weld bead cross-sections, two cases, the partial penetration and the full penetration are separately considered. For the partial penetration, the width, height, depth, area of the top reinforcement (A1) and area of the fusion/penetration zone (A2) were measured. For the full penetration, a bottom reinforcement can be formed and its area (A3) is also measured. These geometrical parameters are schematically shown in Figure 3-7. Besides, two angles θ_1 and θ_2 are reported as shown in Figure 3-8.

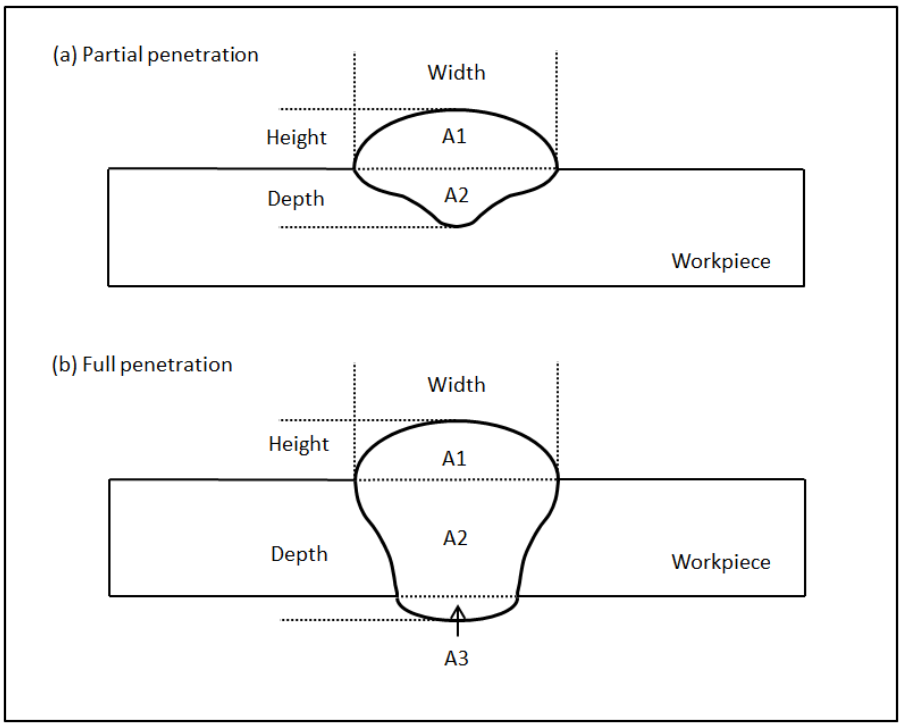

Figure 3-7 Definition of the geometrical parameters for the weld bead cross-section. (a) Partial penetration; (b) Full penetration.

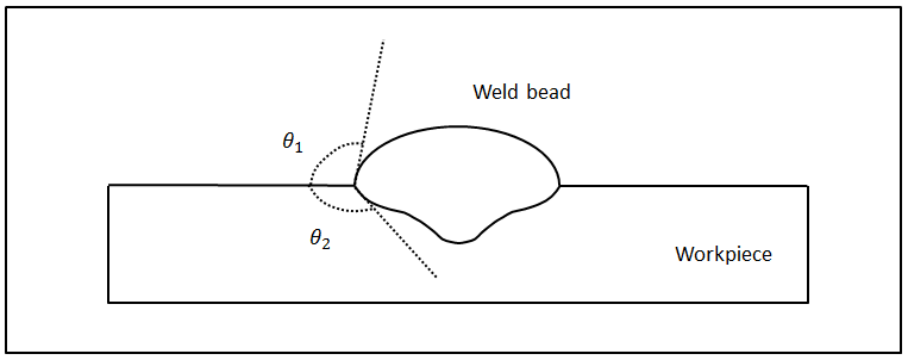

Figure 3-8 Definition of the angles measured in this thesis.

Chapter 4. Results

In this chapter, the results of the bead-on-plate welding and the U-groove butt welding are provided. To obtain an adequate understanding of the influence of shielding gas composition, the Ar-He mixtures and the Ar-CO_2 mixtures are separately presented.

4.1 Bead-on-plate welding

In this section, the results of the bead-on-plate welding including the electrical parameters (voltage and current), the short-circuit parameters (arc time, short-circuit time and short-circuit frequency) and the weld bead geometry are described. A photograph of three welds produced in Ar, He and Ar+3.3% CO_2 is shown in Figure 4-1.

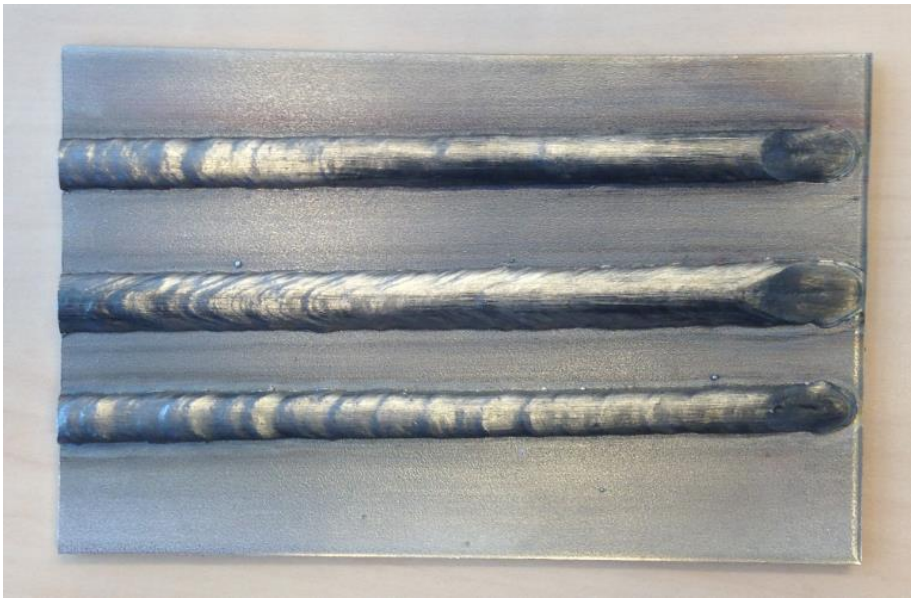

Figure 4-1 The appearance of weld beads at the wire feed rate of 8 m min^{-1} for the cases of He (top), Ar (middle) and Ar+3.3% CO_2 (bottom).

4.1.1 Voltage and current data

The 100-millisecond sections of the measured voltage and current are presented in Figure 4-2, Figure 4-3 and Figure 4-4. The solid lines denote the welding current and the dash lines denote the welding voltage. The measurements demonstrate that short-circuit GMAW is a dynamic process along with the variation of voltage and current. In short-circuit GMAW, a short-circuit cycle encompasses an arc period and a short-circuit period, which can be distinguished by the voltage signal. A sharply increased voltage represents the beginning of the arc period and subsequently a voltage plateau is reached. The

completion of the arc period is marked by a dramatic voltage drop and the short-circuit period featured by a low level of voltage starts. In terms of the current signal, the current keeps growing during the short-circuit period and a maximum is reached. In the arc period, the current decreases from the peak to a low level.

Argon and helium

Figure 4-2 and Figure 4-3 present the measurement of voltage and current in Ar and He respectively at different wire feed rates. It can be seen that for both Ar and He, more short-circuit cycles appear as the wire feed rate increases.

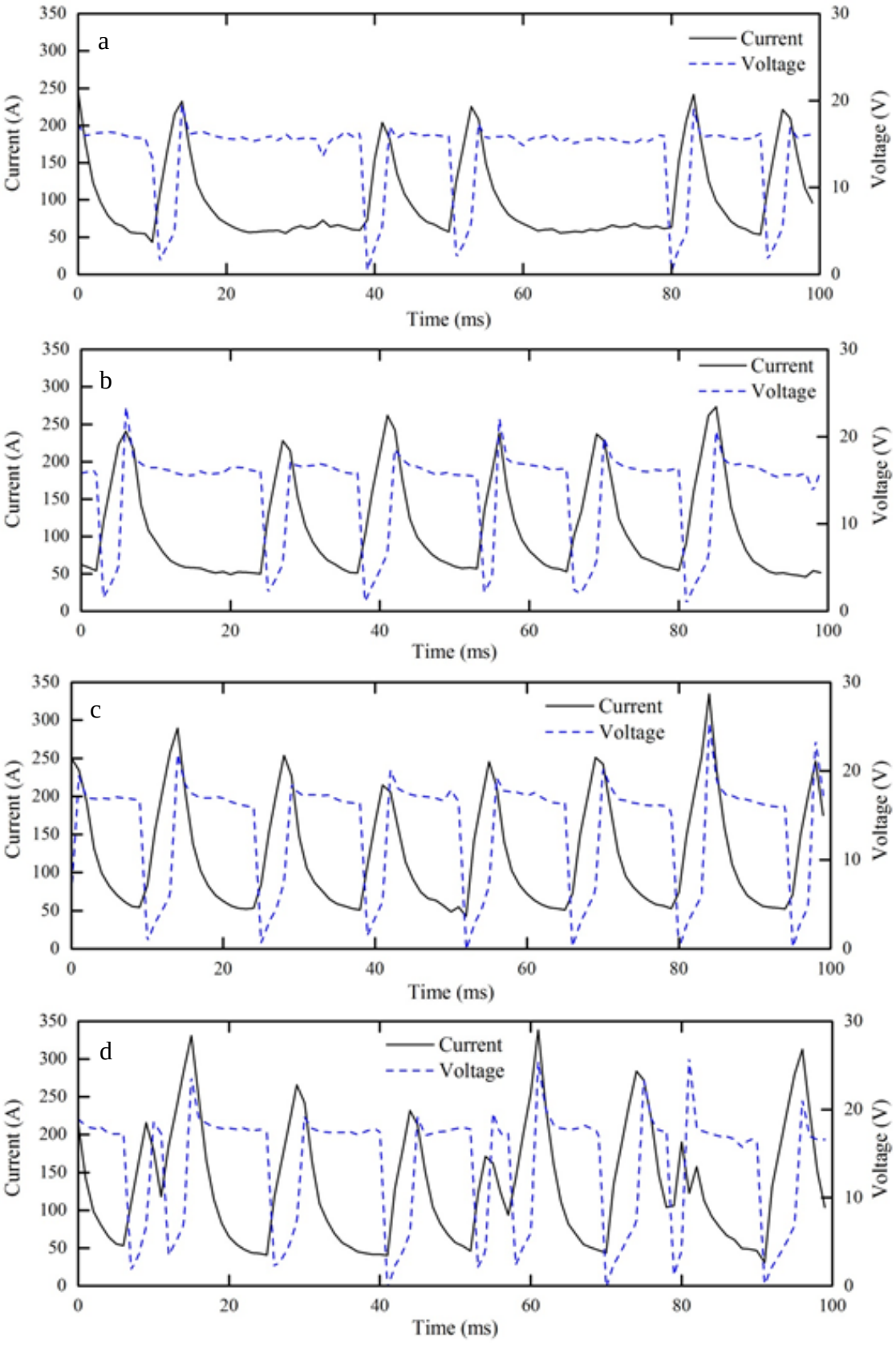

Figure 4-2 The 100-millisecond sections of the voltage and current data in Ar at the wire feed rate of (a) 6 m min^{-1}; (b) 7 m min^{-1}; (c) 8 m min^{-1}; (d) 9 m min^{-1}.

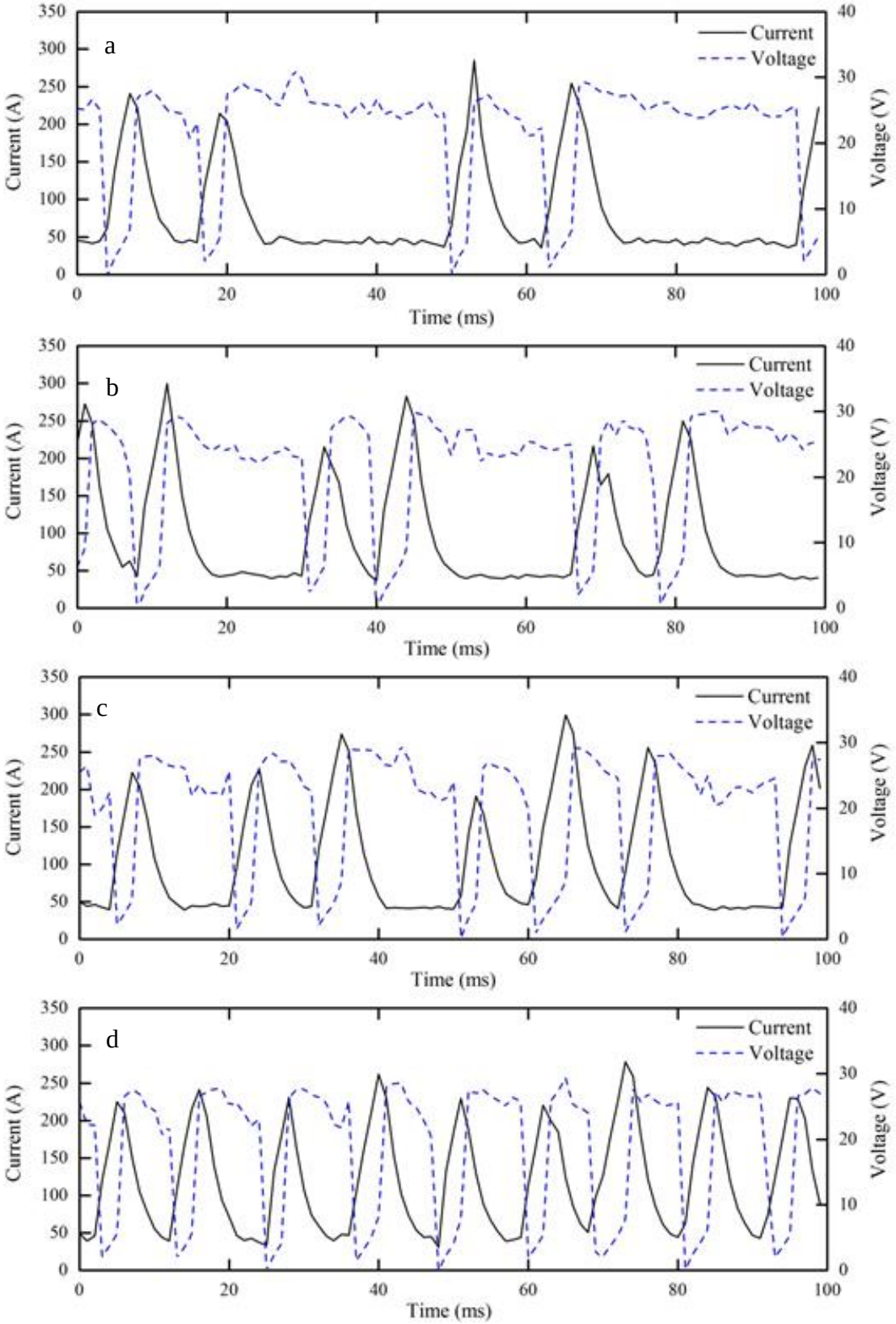

Figure 4-3 The 100-millisecond sections of the voltage and current data in He at the wire feed rate of (a) 6 m min^{-1}; (b) 7 m min^{-1}; (c) 8 m min^{-1}; (d) 9 m min^{-1}.

Argon and CO_2

Figure 4-4 a and b shows the measurement of voltage and current at the wire feed rate of 8 m min^{-1} in Ar+3.3% CO_2 and Ar+3.3% CO_2.

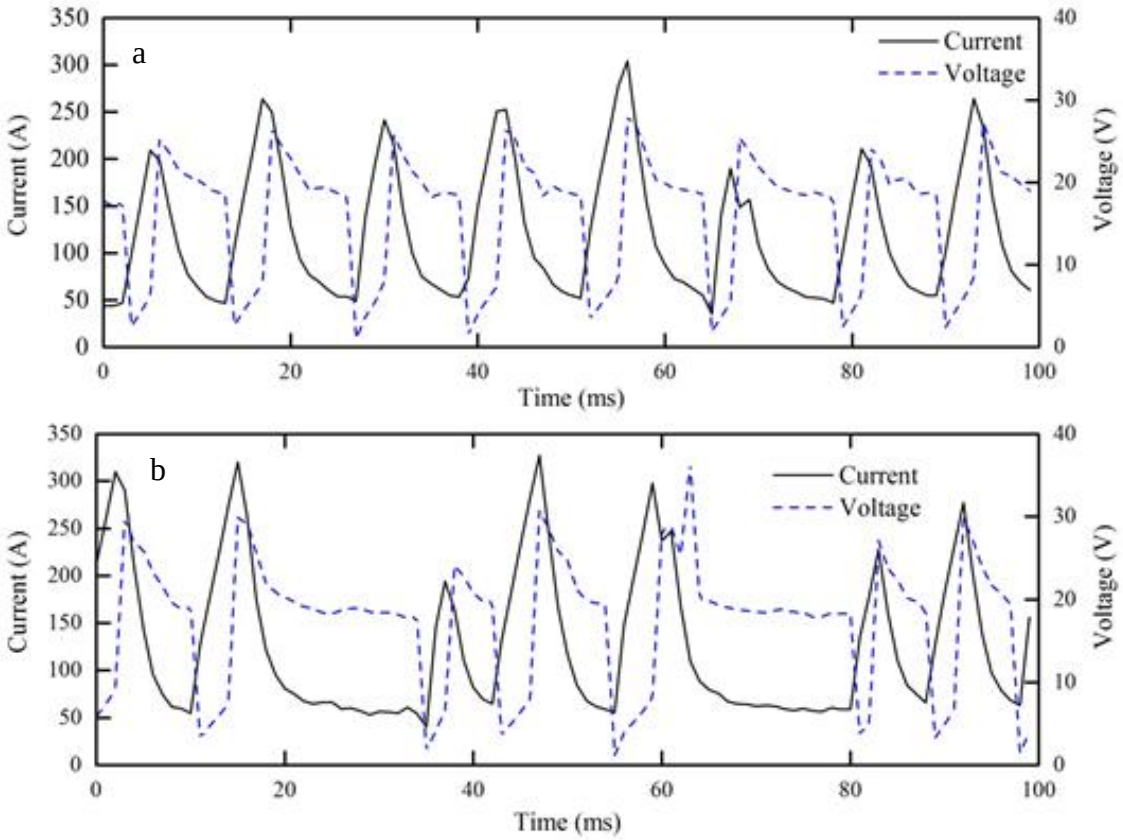

Figure 4-4 The 100-millisecond sections of the voltage and current data at the wire feed rate of 8 m min^{-1} in (a) Ar+3.3% CO_2;(b) Ar+6.7% CO_2.

4.1.2 Average voltage, average current and power of heat source

After obtaining the transient voltage and current and distinguishing the arc period and the short-circuit period, the average voltage (including average arc voltage and average short-circuit voltage) and the average current (average arc current and average short-circuit current) can be calculated. The nominal power of different heat sources is also provided.

Argon and helium

Figure 4-5 a and b present the average welding voltage and current as a function of the wire feed rate. For both Ar and He, as the wire feed rate increases, the voltage decreases but the current increases significantly. It can also be seen that compared with those of Ar, the voltage of He is higher while the current of He is lower.

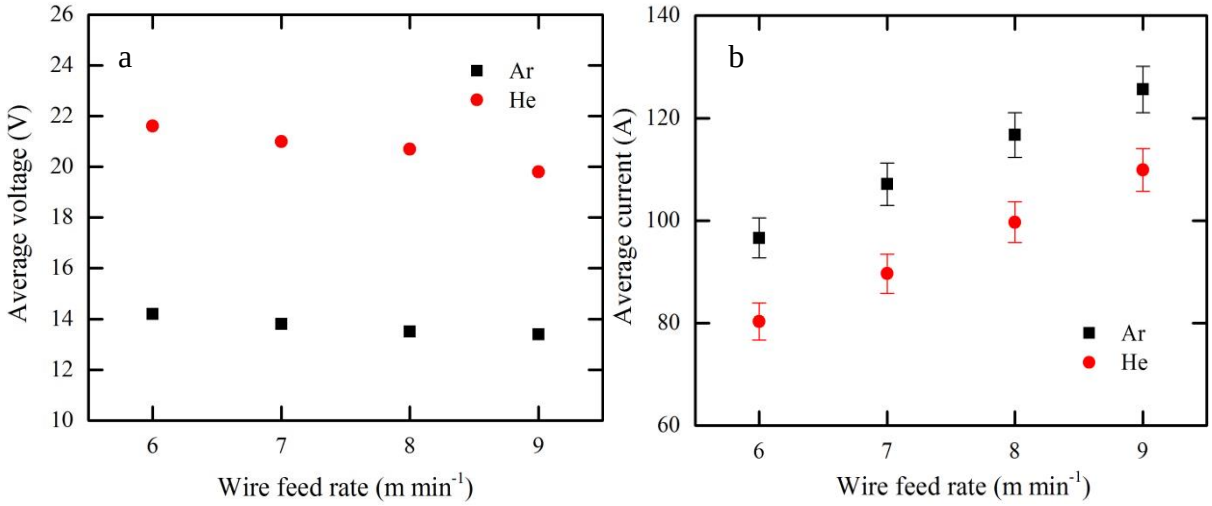

Figure 4-5 (a) The average voltage; (b) The average current, in Ar and He as a function of the wire feed rate.

Furthermore, the average voltage and current in the arc period and the short-circuit period can be described quantitatively. In Figure 4-6 a and b, the average arc voltage and the average short-circuit voltage in Ar and He respectively are plotted. Firstly, it can be observed that for both Ar and He, as the wire feed rate increases, the average arc voltage slightly increases and the average short-circuit voltage almost keeps unchanged which maintains approximately 4 V for all cases. Secondly, it is clear that the arc voltage in He (about 25 V) is higher than that in Ar (about 17 V).

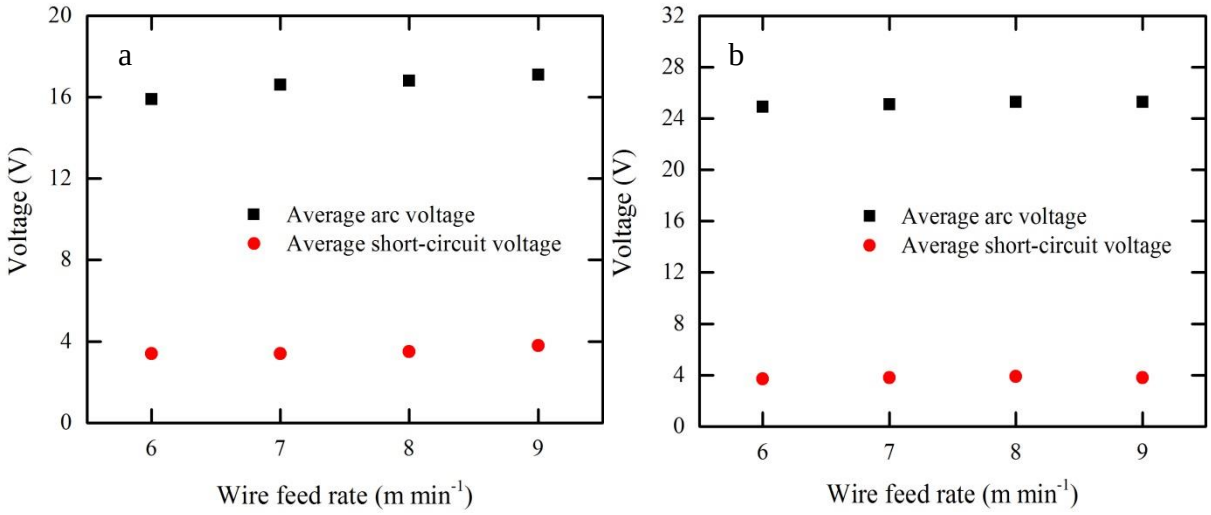

Figure 4-6 The average arc voltage and the average short-circuit voltage as a function of the wire feed rate in (a) Ar; (b) He.

Concerning the current, with the wire feed rate increased, the average arc current and the average short-circuit current increases in both cases of Ar and He (Figure 4-7 a and b). Besides, it is also shown that at the same wire feed rate, the average arc current of Ar is about 20 A higher than that of He.

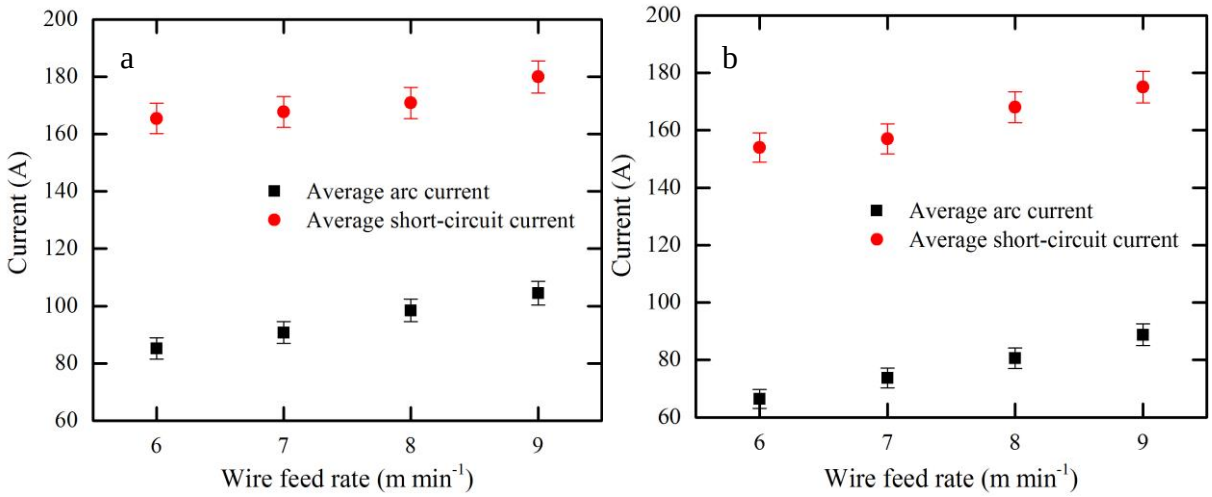

Figure 4-7 The average arc current and the average short-circuit current as a function of the wire feed rate in (a) Ar; (b) He.

The voltage-current diagrams for Ar and He at the wire feed rate of 8 m min^{-1} are depicted in Figure 4-8 a and b. In short-circuit GMAW, points are concentrated on two regions. The upper region represents the arc period due to the high voltage while the lower region is the short-circuit period. It can be seen that the difference between Ar and He mainly focuses on the arc period or rather the arc voltage.

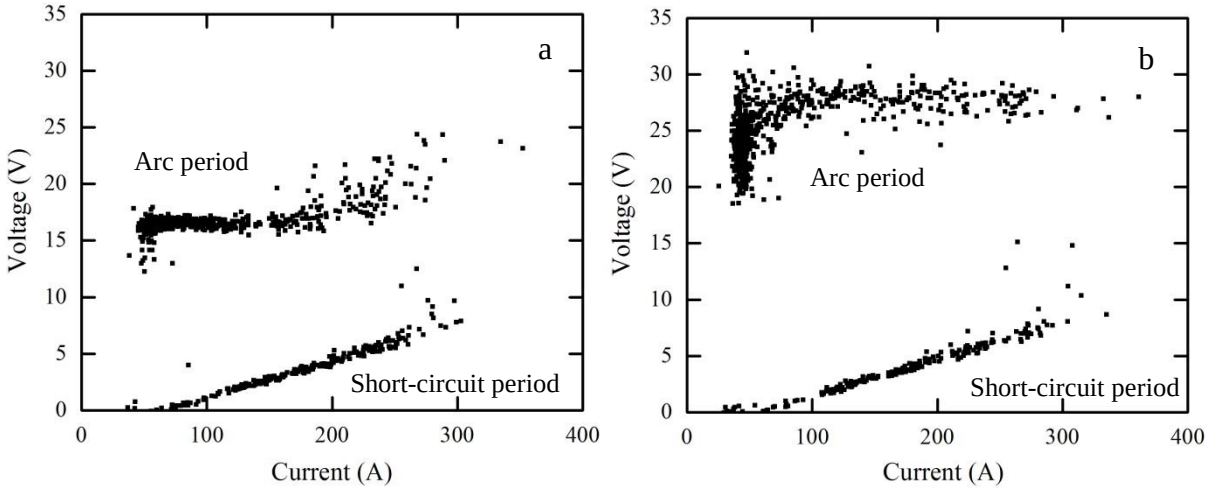

Figure 4-8 The voltage-current diagrams at the wire feed rate of 8 m min^{-1} for (a) Ar; (b) He.

In a certain welding time t_{weld} (s), with incorporating voltage and current, the heat Q generated by the heat source (J) can be calculated by

$$\boldsymbol{Q = \int_0^{t_{weld}} U(t) \cdot I(t) \cdot dt} \tag{4.1}$$

where U is the voltage (V), I is the current (A) and dt is the time interval which is 1 ms in this research. Furthermore, the nominal power $P_{nominal}$ of the heat source (W) can also be obtained as

$$\boldsymbol{P_{nominal} = \frac{Q}{t_{weld}} = \frac{\int_0^{t_{weld}} U(t) \cdot I(t) \cdot dt}{t_{weld}}} \tag{4.2}$$

It should be noted that as shown in Figure 4-2, Figure 4-3 and Figure 4-4, the welding voltage and current is changed periodically over time in short-circuit GMAW. The nominal power of the heat source determines the amount of heat generated per unit time during welding and significantly influences the amount of heat entering the workpiece per unit time.

In Figure 4-9, the nominal power in Ar and He is plotted as a function of wire feed rate. It is shown that for both Ar and He, with the wire feed rate increased, the nominal power increases. Besides, the power in He is greater than that in Ar at the same wire feed rate.

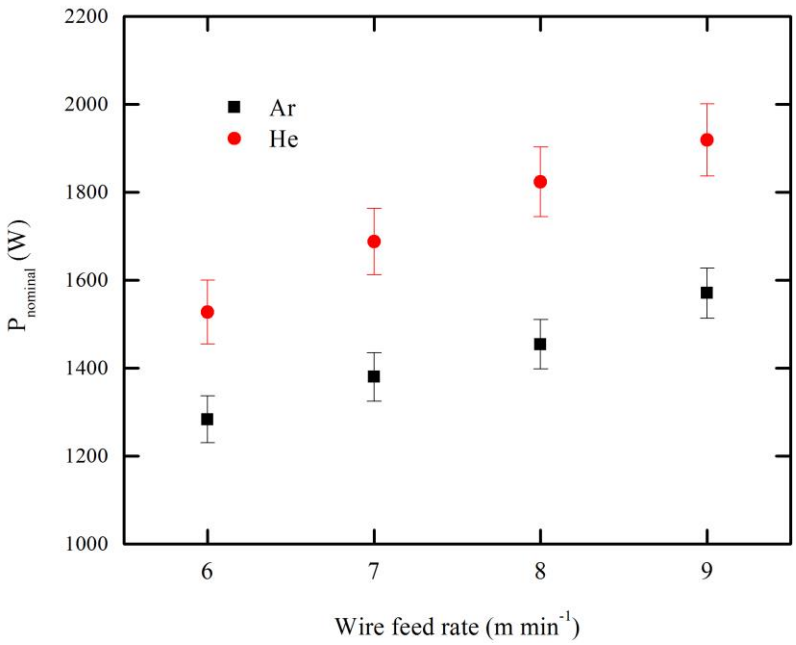

Figure 4-9 The nominal power of the heat source in Ar and He as a function of the wire feed rate.

Argon and CO_2

To begin with, it should be mentioned again that the results of Ar+3.3% CO_2 and Ar+6.7% CO_2 at the wire feed rate of 8 m min^{-1} are contrasted with the results of Ar at the same wire feed rate. In other words, the CO_2 content is the unique variable in this part.

As for the voltage, it can be seen in Figure 4-10 a that the presence of CO_2 raises the average voltage and especially the average arc voltage which increases by about 4 V. Figure 4-10 b describes the current for these three gas compositions. It is shown that the average current lies in the same level while Ar+6.7% CO_2 gives a slight increase of current. Comparing the voltage-current diagrams for Ar+3.3% CO_2 (Figure 4-11 a) and Ar+6.7% CO_2 (Figure 4-11 b) with that for Ar (Figure 4-8 a), it is also demonstrated that the arc voltage is increased by the addition of CO_2. The nominal power of the is provided in Figure 4-12 and it is evident that the presence of CO_2 makes the power increase.

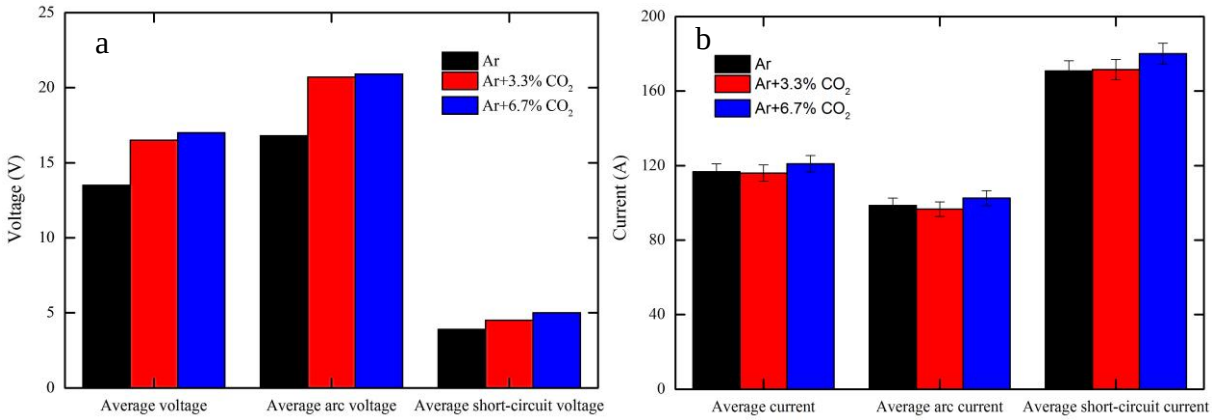

Figure 4-10 (a) The average voltage; (b) the average current, in Ar, Ar+3.3% CO_2 and Ar+6.7% CO_2.

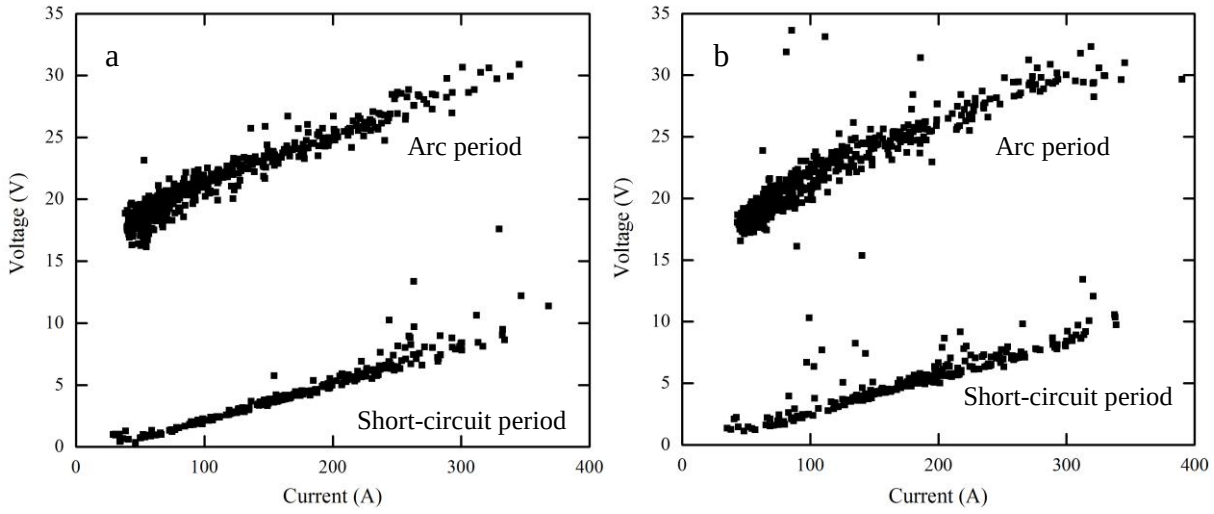

Figure 4-11 The voltage-current diagrams for (a) Ar+3.3% CO_2; (b) Ar+6.7% CO_2.

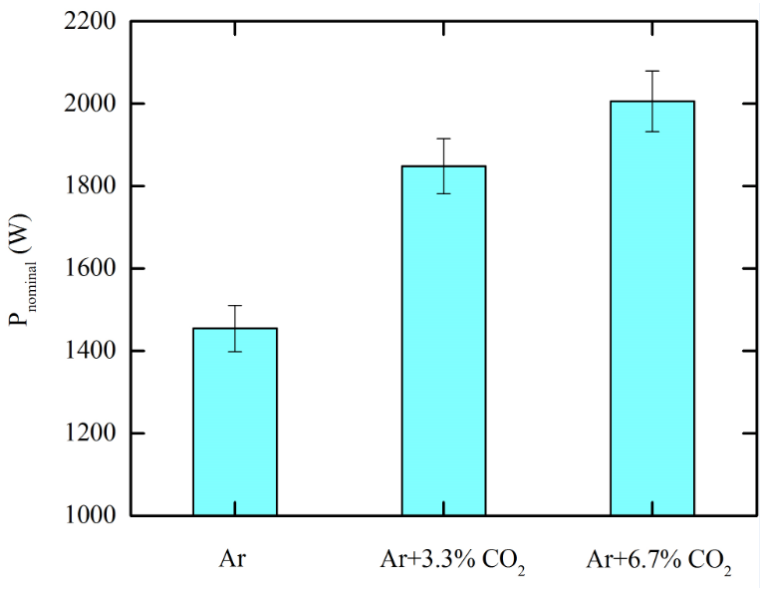

Figure 4-12 The nominal power for Ar, Ar+3.3% CO_2 and Ar+6.7% CO_2.

4.1.3 Temperature measurement

The temperature measurements in Ar, He and Ar+3.3% CO_2 at the wire feed rate of 8 m min^{-1} are plotted as a function of time in Figure 4-13 a, b and c. It is distinct that the peak temperature in Ar, He and Ar+3.3% CO_2 is different. The maximal temperature in Ar is 1024.3±2.2 °C, while the maximum in He is 1146.7±2.2 °C.

The maximal temperature measured in Ar+3.3% CO_2 is 1338.4±2.2 °C. Nevertheless, some points in the measurement are missing. The reason for the lost points is that the temperature range of the K-type thermocouple is -200~1260 °C and the extension grade of this range is 0~200 °C. The melting range of the Inconel625 alloy is 1290~1350 °C. During welding in Ar+3.3% CO_2, the workpiece is fully penetrated (Figure 4-23 a) and the probes of the thermocouple touch the liquid metal for few seconds, during which the measurement cannot be done. Therefore, it must be stated that the measured peak temperature (1338.4±2.2 °C) may not be the actual peak temperature reached in Ar+3.3% CO_2.

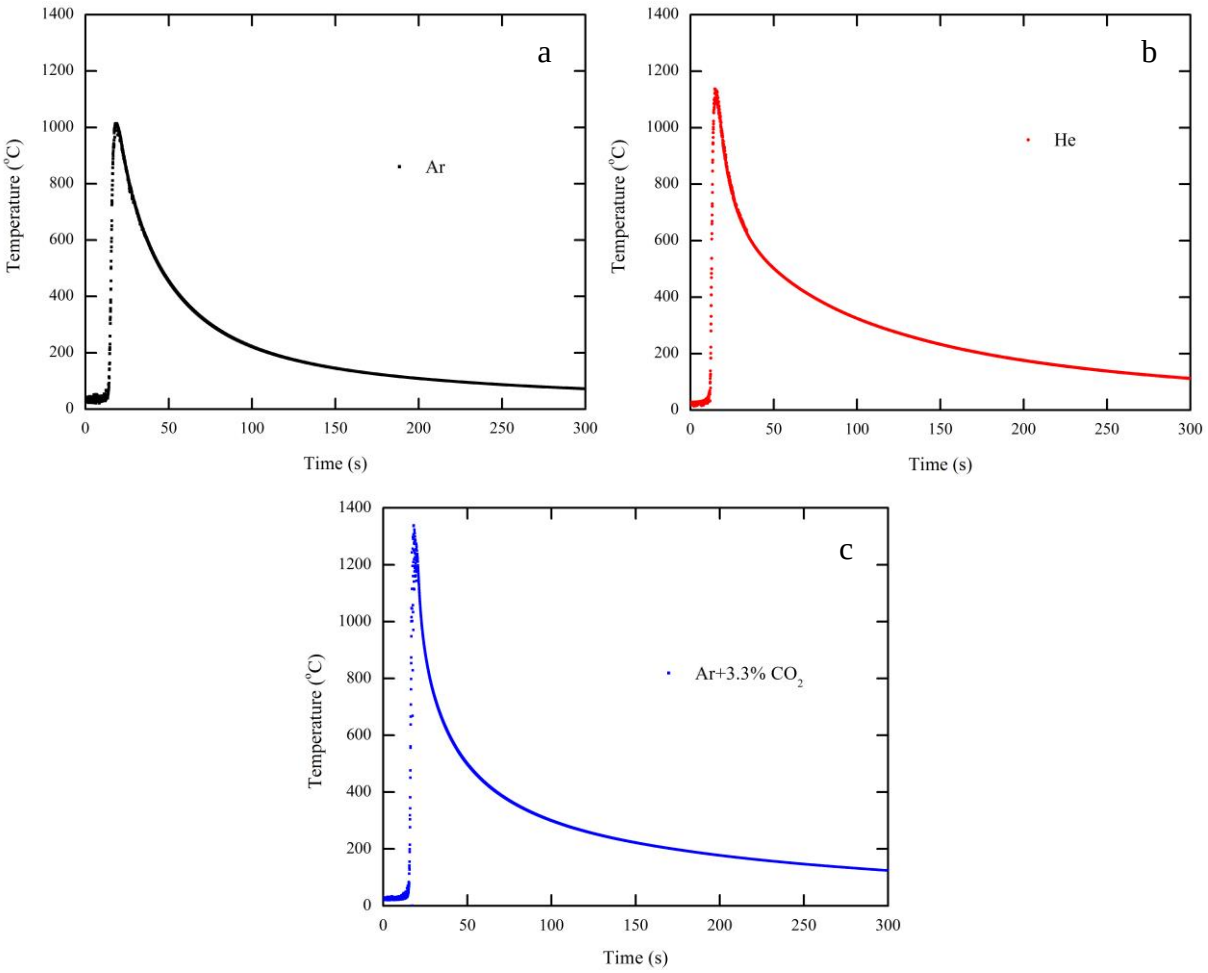

Figure 4-13 Temperature measurements as a function of time at the wire feed rate of 8 m min^{-1} in (a) Ar, (b) He and (c) Ar+3.3% CO_2.

4.1.4 Arc time, short-circuit time and short-circuit frequency

It is known that a short-circuit cycle is comprised of an arc period and a short-circuit period. The duration of each period and the short-circuit frequency are important characteristics of short-circuit GMAW. The arc time and short-circuit time can be derived from the voltage and current signals. The frequency is equal to the quotient of the number of the short-circuit cycles and the measurement time.

Argon and helium

The diagrams of average arc time and the average short-circuit time as a function of the wire feed rate for the cases of Ar and He are presented in Figure 4-14 a and b respectively. It can be seen that for both Ar and He, as the wire feed rate increases, the average arc time decreases while the average short-circuit time almost keeps constant (about 4 ms). In other word, the ratio between the arc time and the short-circuit time is reduced. Figure 4-15 depicts the short-circuit frequency for Ar and He. With the wire feed rate increased, the frequency is raised and the growth rate of Ar is higher than that of He.

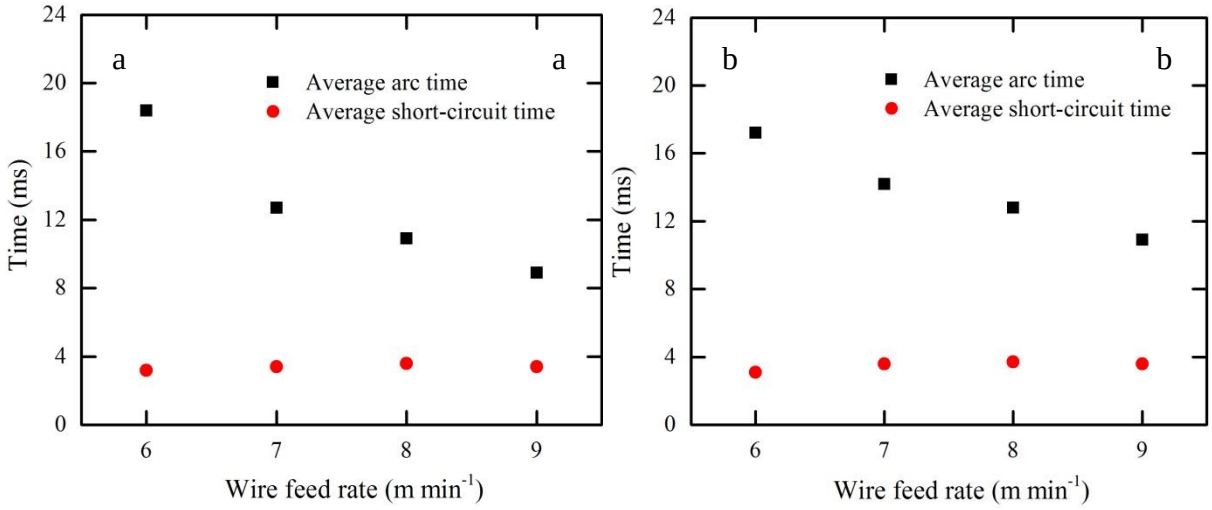

Figure 4-14 The average arc time and short-circuit time as a function of the wire feed rate in (a) Ar; (b) He.

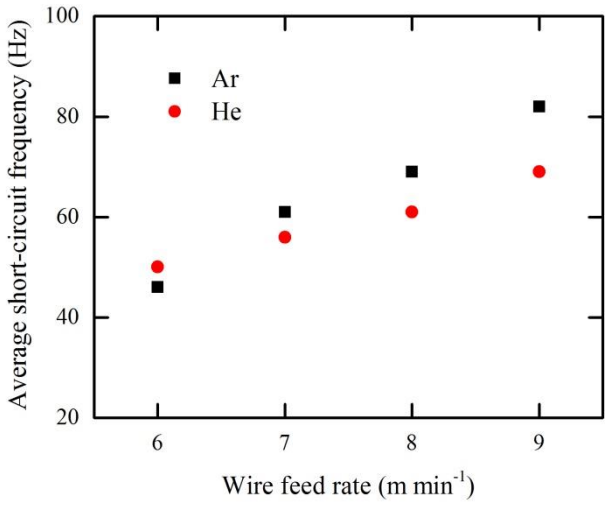

Figure 4-15 The short-circuit frequency as a function of the wire feed rate in Ar and He.

Argon and CO_2

The average arc time, short-circuit time and short-circuit frequency for Ar and Ar-CO_2 mixtures are presented in Figure 4-16. It is observed that with the presence of CO_2, the average arc time is reduced and the short-circuit frequency is raised.

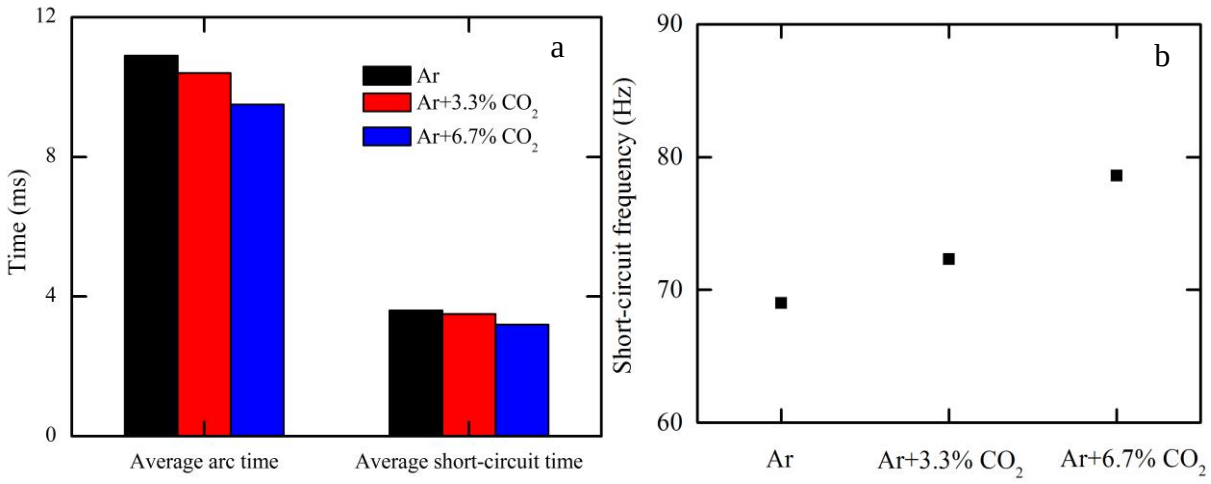

Figure 4-16 (a) The average arc time and short-circuit time; (b) The short-circuit frequency, for Ar, Ar+3.3% CO_2 and Ar+6.7% CO_2.

4.1.5 Standard deviation in arc time and short-circuit time

The arc time and the short-circuit time are important features of short-circuit GMAW. The variation of them which is characterised by the standard deviation can serve as the criterion for the process regularity. Comparing Figure 4-2 c with Figure 4-2 a, it can be seen that the short-circuit cycles in Figure 4-2 c are similar and all the arc periods almost lasts for the same time. In other word, the voltage and current signals in Figure 4-2 c is more regular than those in Figure 4-2 a. It is stated that a high process regularity will lead to a low spatter loss and increase the process efficiency [14, 34].

Argon and helium

The standard deviation of the arc time and the short-circuit time as a function of the wire feed rate for Ar and He is given in Figure 4-17 a and b. For Ar, with the wire feed rate increased, the standard deviation of the arc time decreases firstly and then increases while a minimum is found at the wire feed rate of 8 m min^{-1}. For He, the standard deviation of the arc time is continuously reduced as the wire feed rate increases. The standard deviation of the short-circuit time for both Ar and He remains in a low level (about 0.8 ms) as the wire feed rate is changed.

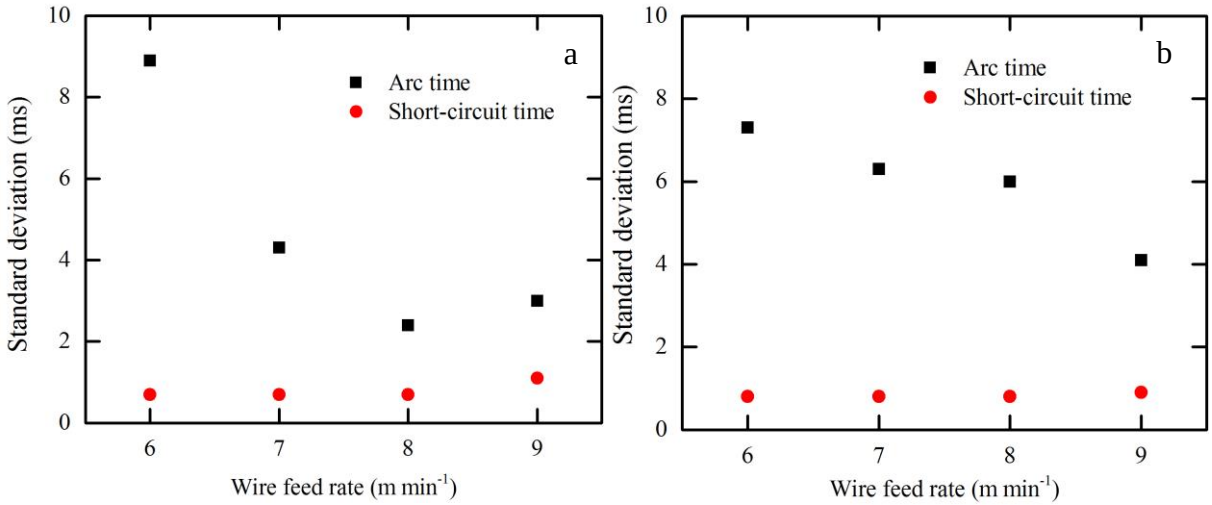

Figure 4-17 The standard deviation of the arc time and the short-circuit time as a function of the wire feed rate in (a) Ar; (b) He.

Argon and CO_2

Figure 4-18 depicts the standard deviation of the arc time and the short-circuit time for the cases of Ar, Ar+3.3% CO_2 and Ar+6.7% CO_2. It is shown that the presence of CO_2 makes the standard deviation of the arc time increase. In other words, the process becomes irregular as a certain amount of CO_2 is present. However, the standard deviation of the short-circuit time almost keeps unchanged.

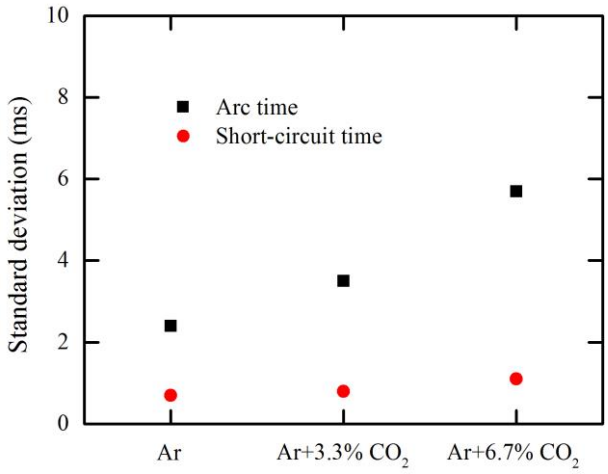

Figure 4-18 The standard deviation of the arc time and the short-circuit time in Ar, Ar+3.3% CO_2 and Ar+6.7% CO_2.

4.1.6 Weld bead geometry

In this part, the cross-sections of the weld beads obtained from the bead-on-plate welding are provided. Several geometrical parameters such as the width, height, depth, reinforcement area and fusion area are considered. The definition of these values is shown in Figure 3-7.

Argon and helium

The cross-sections of the weld beads in Ar and He are presented in Figure 4-19 and Figure 4-20 respectively. It is shown that the weld beads in Ar are characterised by the narrow, finger-like penetration while the penetration zone in He is relatively broad and parabolic.

In Figure 4-21, the height, width and depth of the weld beads in Ar and He are plotted as a function of the wire feed rate. As the wire feed rate is increased, the weld beads in both Ar and He widen and deepen. Moreover, at the same wire feed rate, the width of weld beads in Ar is larger than that in He. As for the depth, at the wire feed rate of 6 and 7 m min^{-1}, the weld beads in Ar is deeper than those in He. Nevertheless, the contrary is the case at 8 and 9 m min^{-1}.

The reinforcement area in Ar and He is described as a function of the wire feed rate in Figure 4-22 a. It should be firstly mentioned that a theoretical value of the reinforcement area denoted by the dash line can be derived as

$$\boldsymbol{A_{reinforcement} = \frac{V_{wire} \cdot A_{wire}}{V_{travel}}} \tag{4.3}$$

where $A_{reinforcement}$ is the reinforcement area, V_{wire} is the wire feed rate, A_{wire} is the cross-sectional area of the wire and V_{travel} is the travel speed. Due to a spatter loss in welding, the actual reinforcement area is smaller than the theoretical area. The deviation between these two values can be used to determine the severity of spatter. Figure 4-22 a shows that there is little difference of reinforcement area between Ar and He.

In Figure 4-22 b, the fusion/penetration area in Ar and He is provided. It can be observed that with the wire feed rate increased, the fusion zone in both Ar and He is enlarged. Moreover, the fusion area of He is larger than that of Ar at the same wire feed rate.

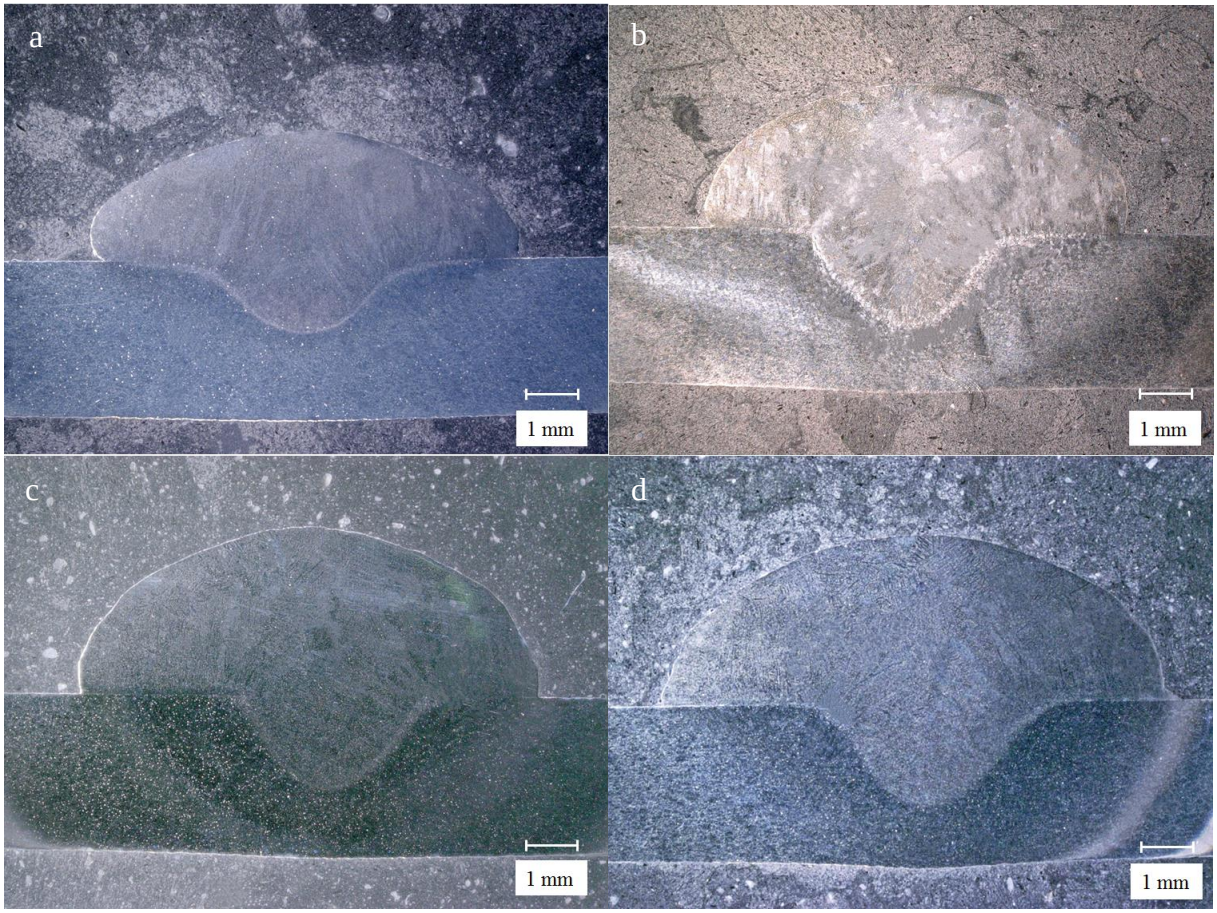

Figure 4-19 The cross-sections of the weld beads in Ar at the wire feed rate of (a) 6 m min^{-1}; (b) 7 m min^{-1}; (c) 8 m min^{-1}; (d) 9 m min^{-1}.

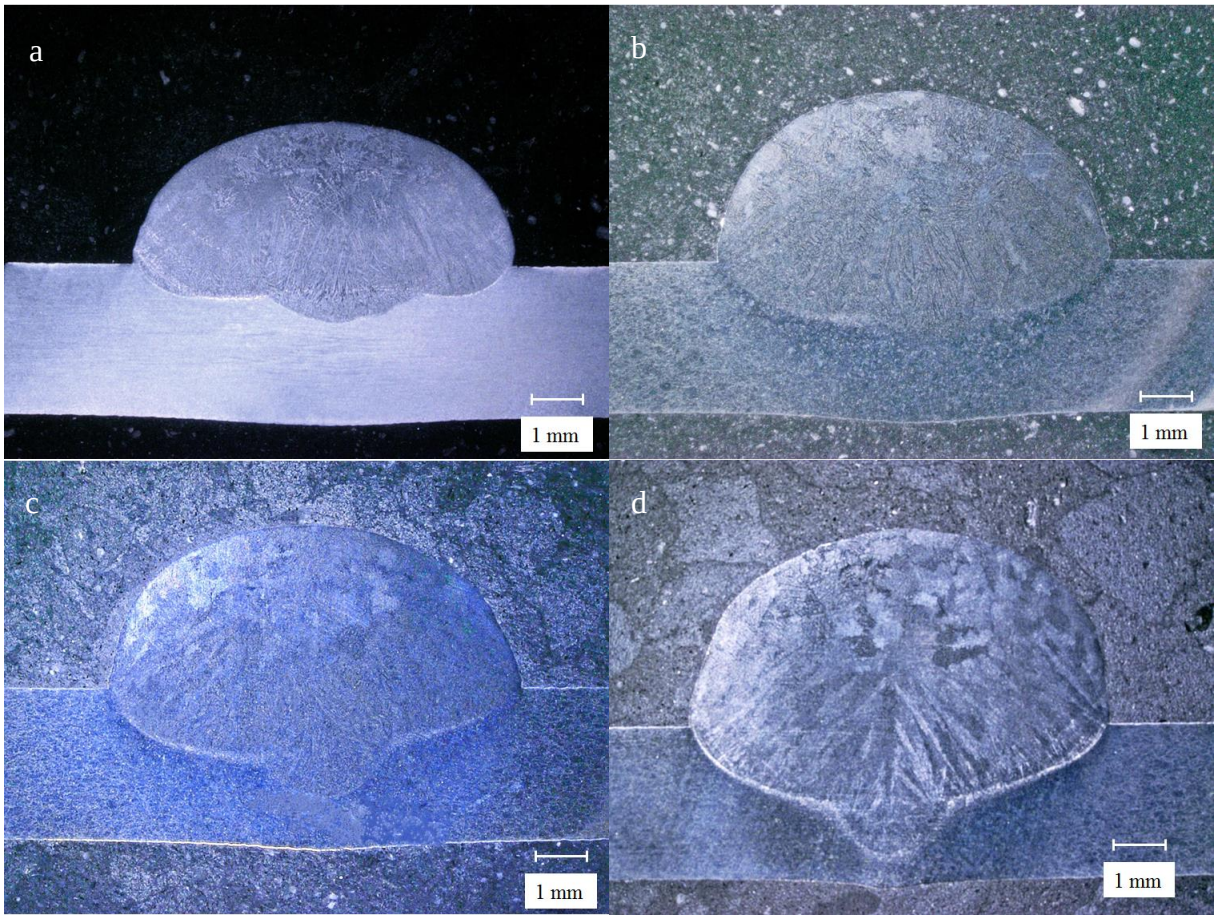

Figure 4-20 The cross-sections of the weld beads in He at the wire feed rate of (a) 6 m min^{-1}; (b) 7 m min^{-1}; (c) 8 m min^{-1}; (d) 9 m min^{-1}.

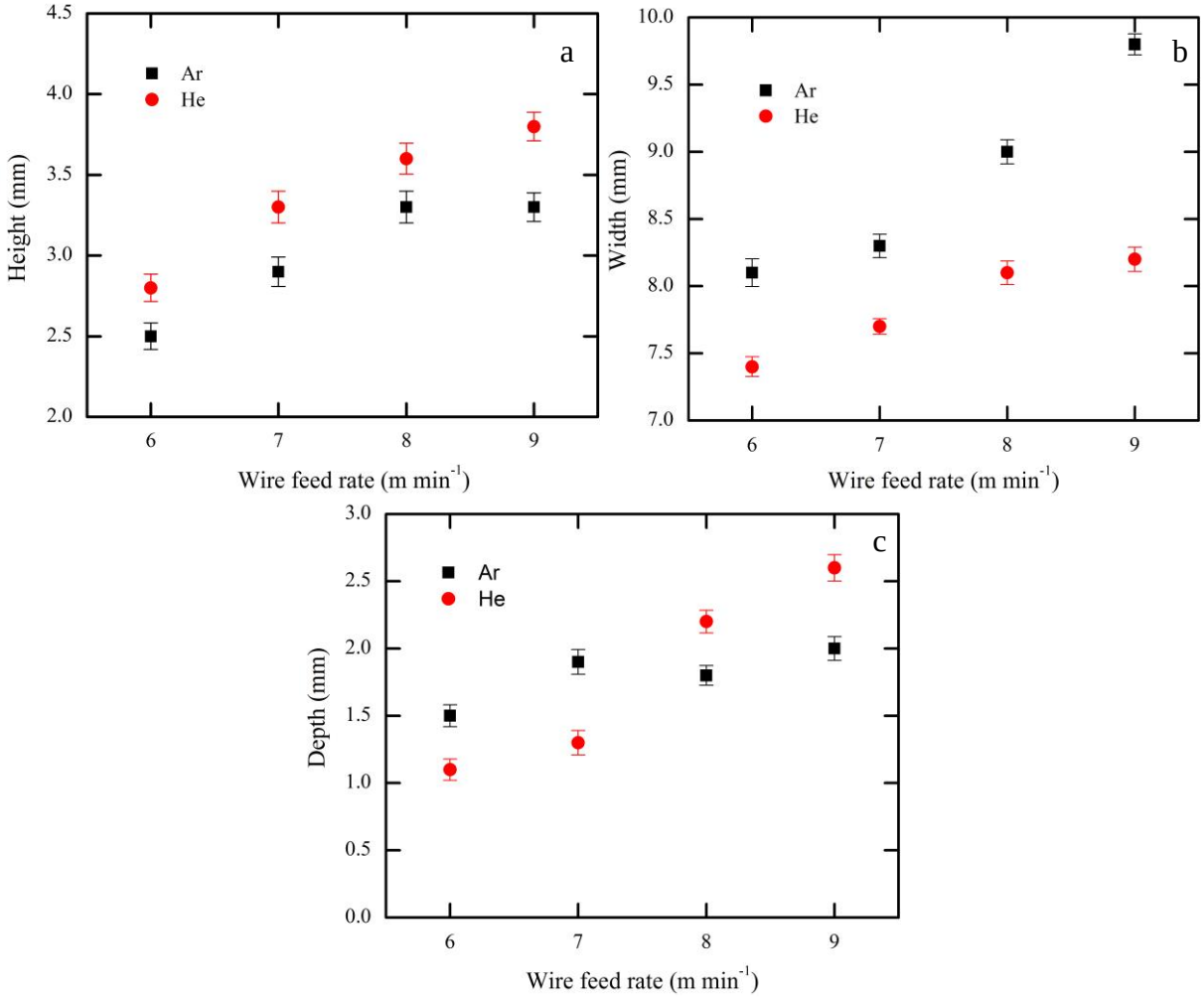

Figure 4-21 The cross-sectional dimensions of the weld beads in Ar and He: (a) Height; (b) Width; (c) Depth.

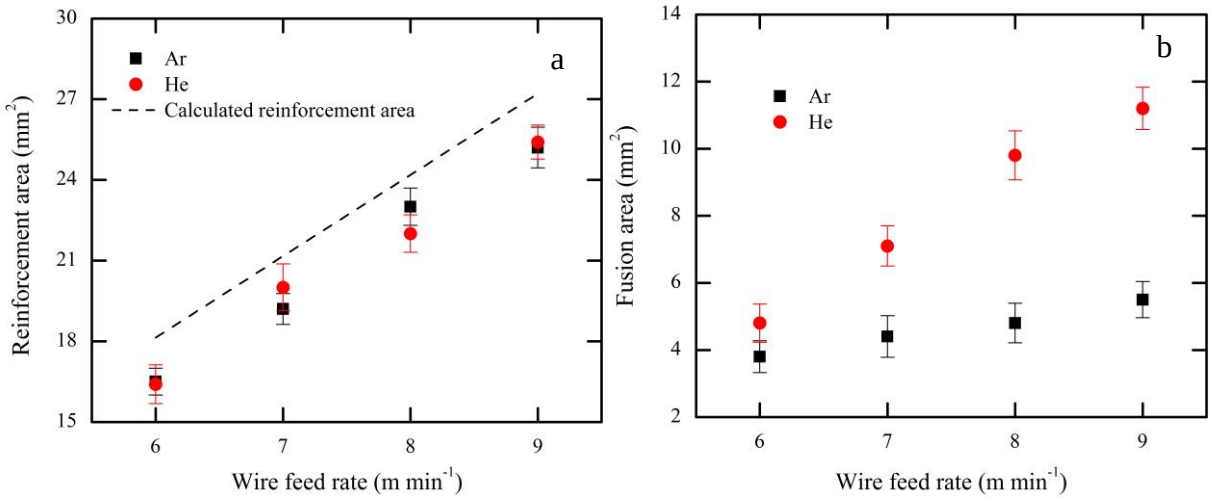

Figure 4-22 The cross-sectional area of the weld beads in Ar and He: (a) Reinforcement area; (b) Fusion area.

Argon and CO_2

The cross-sections of the weld beads in Ar+3.3% CO_2 and Ar+6.7% CO_2 at the wire feed rate of 8 m min^{-1} are presented in Figure 4-23. It is distinct that compared with the weld bead in Figure 4-19 c, the weld beads get fully penetrated in the Ar-CO_2 gas mixtures. The height, width and depth of the weld beads in Ar, Ar+3.3% CO_2 and Ar+6.7% CO_2 are plotted in Figure 4-24 a. It is shown that with the presence of CO_2, the height is almost unchanged while the width is reduced and the depth is increased. In Figure 4-24 b, the reinforcement area and the fusion area of the weld beads are described. It can be seen that the reinforcement area in both Ar+3.3% CO_2 and Ar+6.7% CO_2 is less than that in Ar. With respect to the fusion zone, this area is significantly enlarged as the CO_2 content is increased.

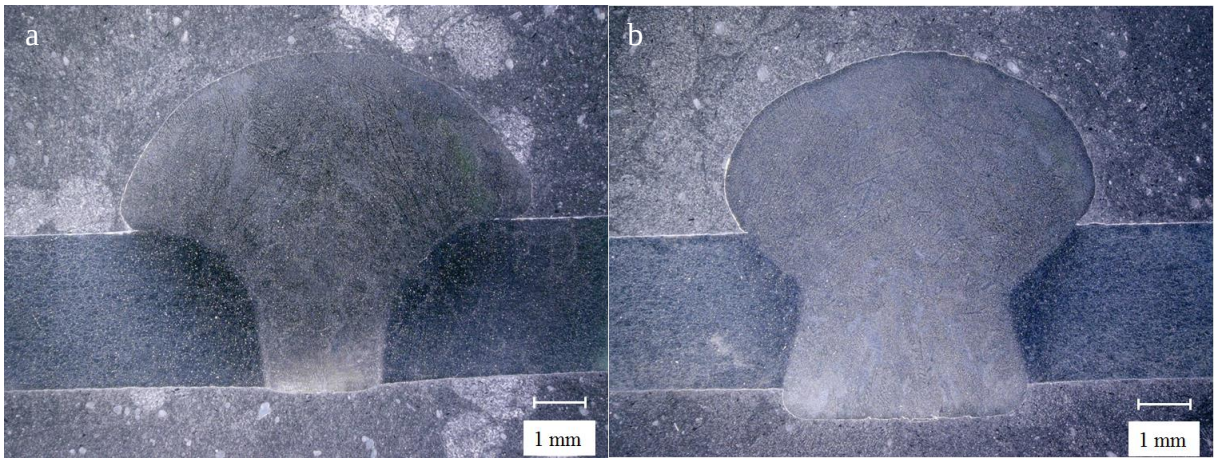

Figure 4-23 The cross-sections of the weld beads in (a) Ar+3.3% CO_2 and (b) Ar+6.7% CO_2 at the wire feed rate of 8 m min^{-1}.

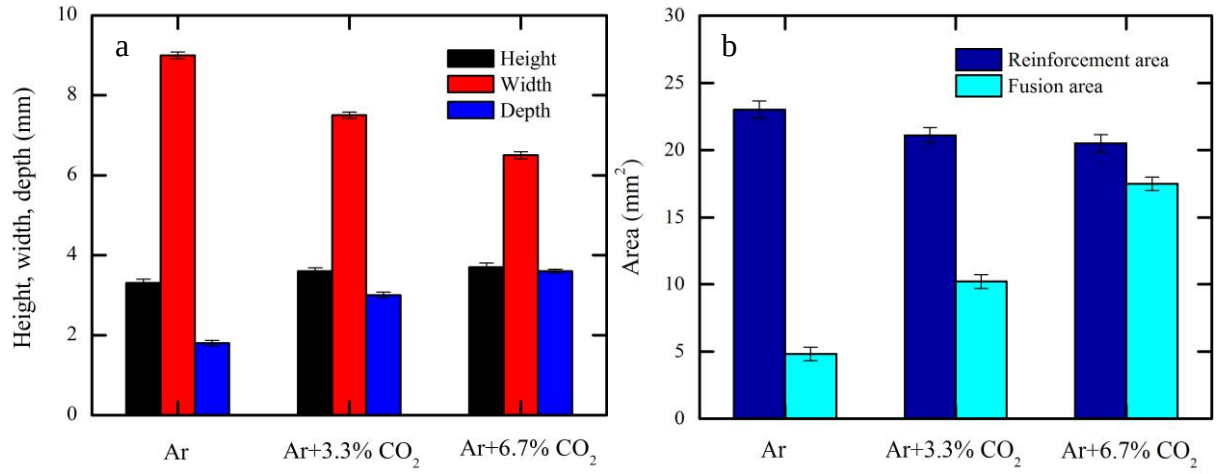

Figure 4-24 The cross-sectional geometry of the weld beads in Ar, Ar+3.3% CO_2 and Ar+6.7% CO_2: (a) Dimensions; (b) Area.

4.1.7 Angle measurement

In this section, two angles θ_1, θ_2 measured at the weld toe are provided and the definition of the angles is shown in Figure 3-8.

Argon and helium

In Figure 4-25 a, it can be seen that as the wire feed rate is elevated, θ_1 in both Ar and He is increased except for the case of He at 9 m min^{-1}. Moreover, at the same wire feed rate, θ_1 in Ar is smaller than that in He. With regard to the angle θ_2, it can be seen in Figure 4-25 b that θ_2 in Ar is 180° whatever the wire feed rate is. θ_2 in He is smaller than 180° and reduced as the wire feed rate is elevated.

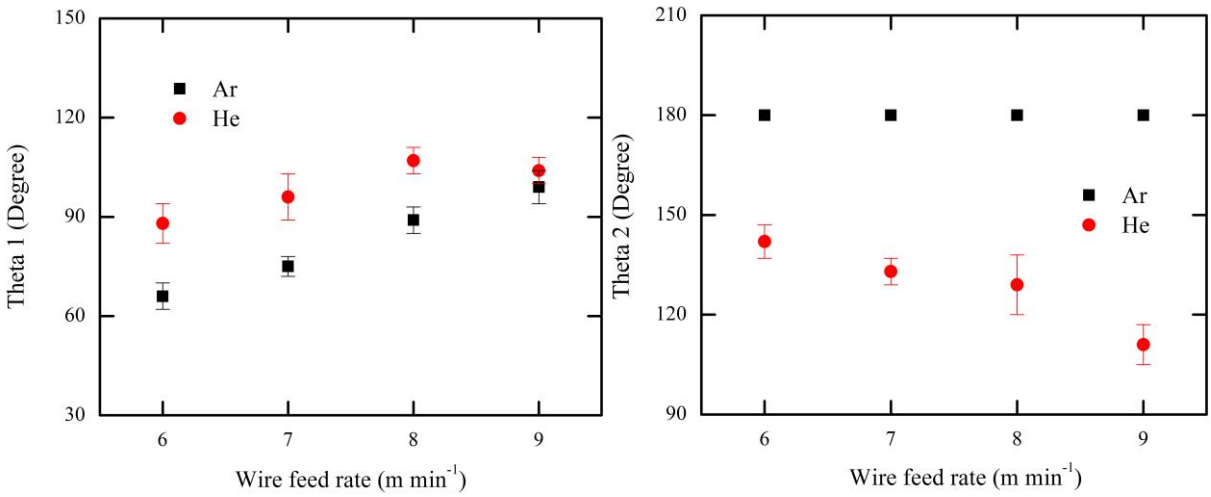

Figure 4-25 The angles measured at the weld toe in Ar and He as a function of the wire feed rate. (a) θ_1; (b) θ_2.

Argon and CO_2

In Figure 4-26, the angle θ_1 and θ_2 in Ar, Ar+3.3% CO_2 and Ar+6.7% CO_2 at the wire feed rate of 8 m min^{-1} are described. It can be seen that with the presence of CO_2, θ_1 is less than 90°. Besides, θ_2 in both Ar and Ar+3.3% CO_2 are 180° while that in Ar+6.7% CO_2 is 135°.

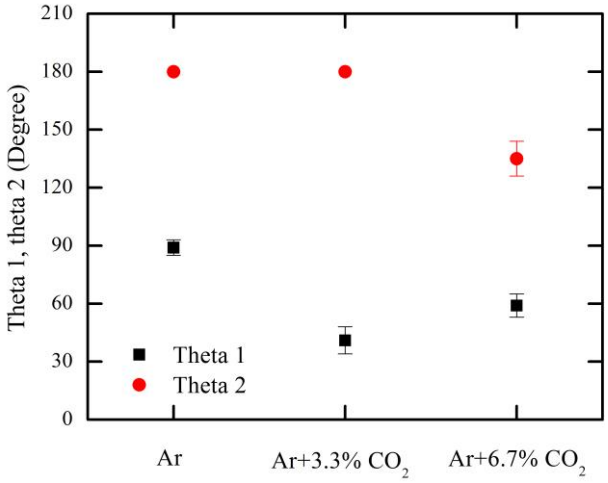

Figure 4-26 The angle measured at the weld toe in Ar, Ar+3.3% CO_2 and Ar+6.7% CO_2 at the wire feed rate of 8 m min^{-1}.

4.2 Butt welding with a U-shaped groove

In this section, the results of the U groove butt welding including the electrical parameters (voltage and current), the short-circuit parameters (arc time, short-circuit time and short-circuit frequency) and the weld bead geometry are described. A photograph of two welds produced in Ar and Ar+3.3% CO_2 is shown in Figure 4-27.

Figure 4-27 The appearance of weld beads for the cases of Ar (left) and Ar+3.3% CO_2 (right).

4.2.1 Average voltage, average current and power of heat source

Argon and helium

The diagrams of average voltage, average current and power of the heat source as a function of the He fraction are presented in Figure 4-28. With an increase of He content, both the average voltage and the average arc voltage increase firstly and then a voltage plateau is reached at the He content of 60%, while the average short-circuit voltage almost keeps unchanged (Figure 4-28 a). In Figure 4-28 b, it can be seen that as the He content is elevated, the average current and the average arc current gradually decrease. Figure 4-28 c indicates the change of the nominal power of the heat source. It is shown that with the He content increased, the power sharply increases at first but then slightly decreases. The maximum lies in the range of 60% ~ 80% He.

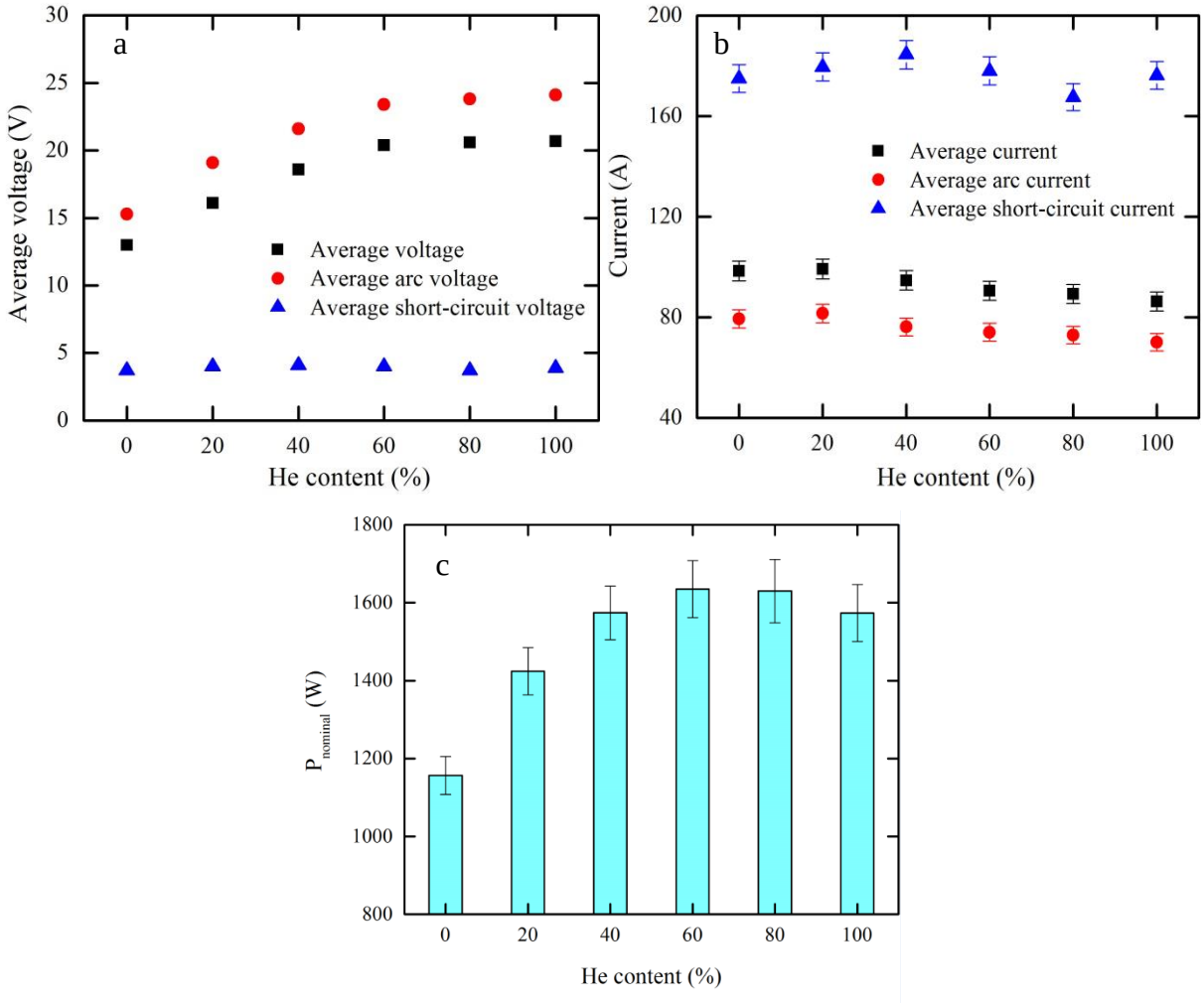

Figure 4-28 The diagrams of (a) the average voltage (including the average arc voltage and short-circuit voltage), (b) the average current (including the average arc current and short-circuit current) and (c) the nominal power as a function of the He content.

Argon, helium and CO_2

The average voltage, the average current and power of the heat source in the Ar-He-CO_2 mixtures are plotted in Figure 4-29. For the convenience of comparison, the results of Ar and Ar+40% He are presented again. As for the voltage, it should be noted that the average arc voltage increases with the presence of CO_2 (Figure 4-29 a) but the change of the average short-circuit voltage is small. In Figure 4-29 b, it is shown that the average current and the average arc current slightly decreases. In Figure 4-29 c, the nominal power of Ar+3.3% CO_2 is much higher than that of Ar, while the power of Ar+40% He+3.3% CO_2 is slightly lower than that of Ar+40% He.

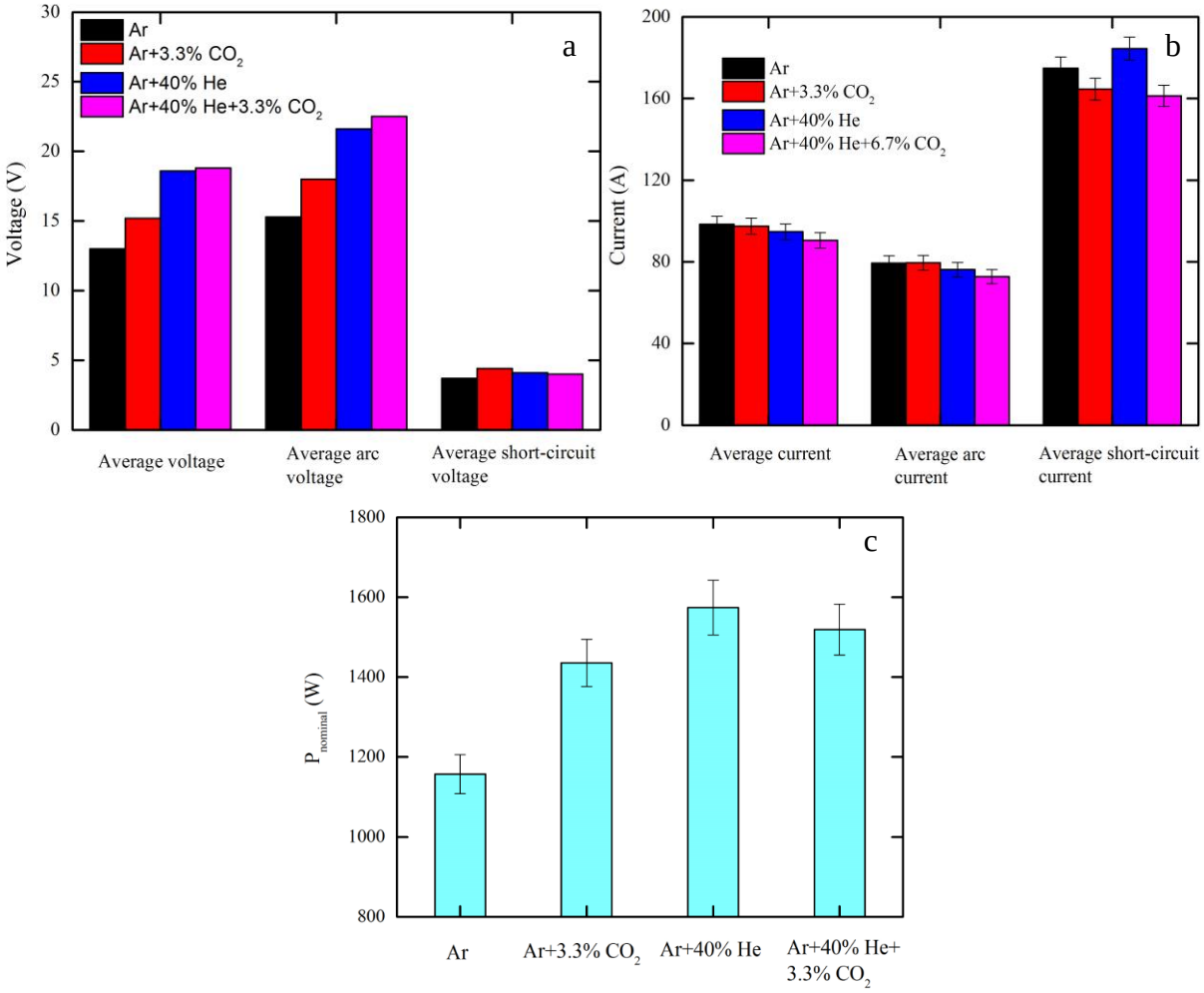

Figure 4-29 The diagrams of (a) the average voltage (including the average arc voltage and short-circuit voltage), (b) the average current (including the average arc current and short-circuit current) and (c) the nominal power, for Ar, Ar+3.3% CO_2, Ar+40% He and Ar+40% He+3.3% CO_2.

4.2.2 Arc time, short-circuit time and short-circuit frequency

Argon and helium

Figure 4-30 a describes the average arc time and the average short-circuit time as a function of the He content. It can be seen that with the He content increased, the arc time does not change largely which is around 16.5 ms for all cases. The short-circuit time almost keeps constant at approximately 3.8 ms. Figure 4-30 b plots the short-circuit frequency in the Ar-He mixtures. It is shown that with an increase of He fraction, the short-circuit frequency is around 50 Hz for all cases.

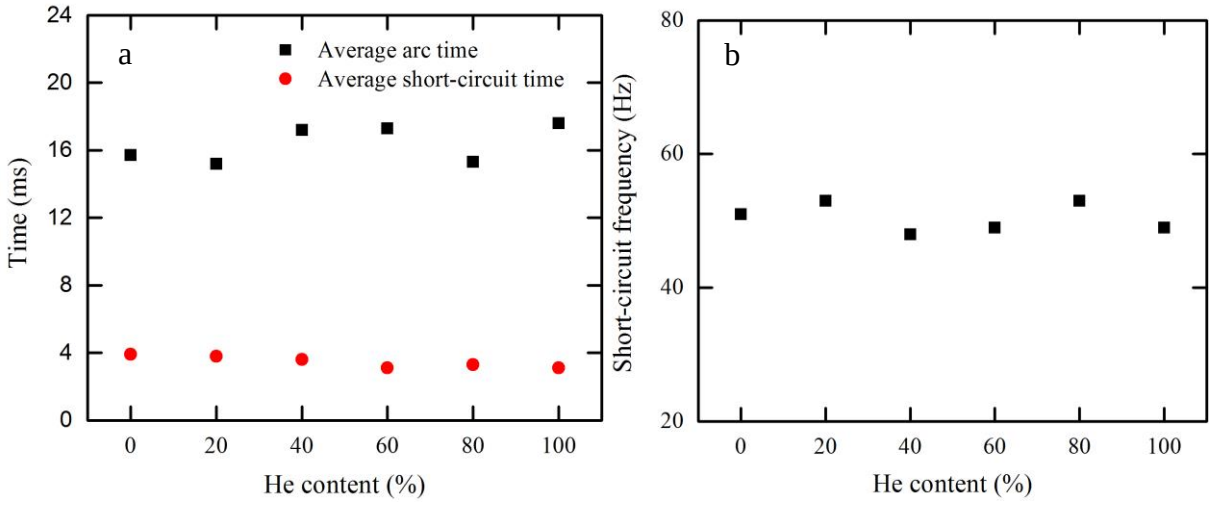

Figure 4-30 (a) The average arc time and short-circuit time; (b) The short-circuit frequency as a function of the wire feed rate.

Argon, helium and CO_2

In Figure 4-31 a and b, it can be clearly seen that with addition of 3.3% CO_2, the average arc time is reduced while the short-circuit frequency is increased. The average short-circuit time almost keeps unchanged.

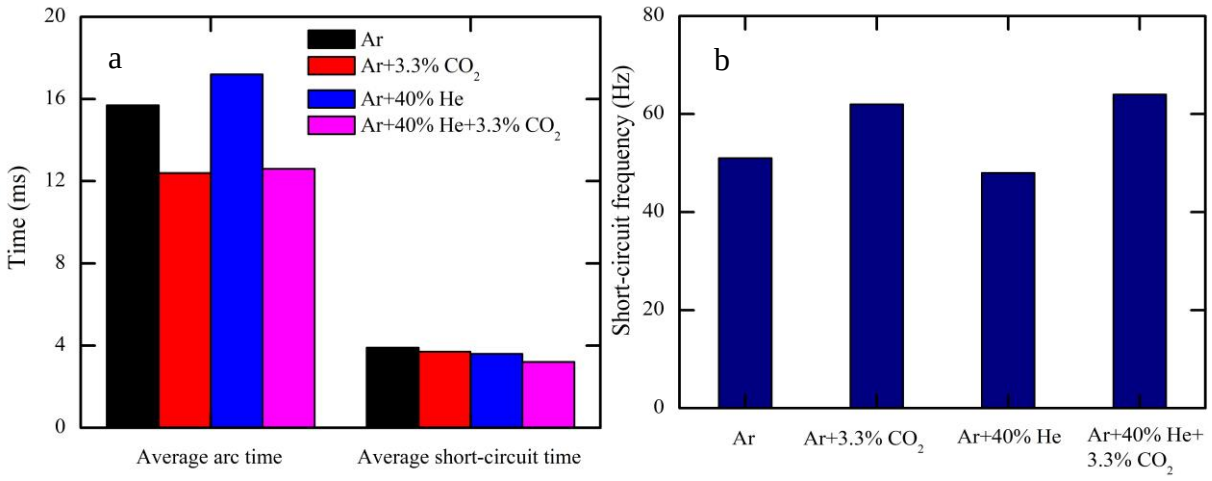

Figure 4-31 (a) The average arc time and short-circuit time; (b) The short-circuit frequency for Ar, Ar+3.3% CO_2, Ar+40% He and Ar+40% He+3.3% CO_2.

4.2.3 Weld bead geometry

In this part, the cross-sections of the weld beads obtained from the butt welding are provided. Several geometrical parameters such as the width, height, depth, top reinforcement area, bottom reinforcement area and fusion area are considered. The definition of these values is shown in Figure 3-7.

Argon and helium

The cross-sections of the weld beads in the Ar-He gas mixtures are presented in Figure 4-32. It is evident that the weld bead geometry can be greatly influenced by the Ar-He gas composition.

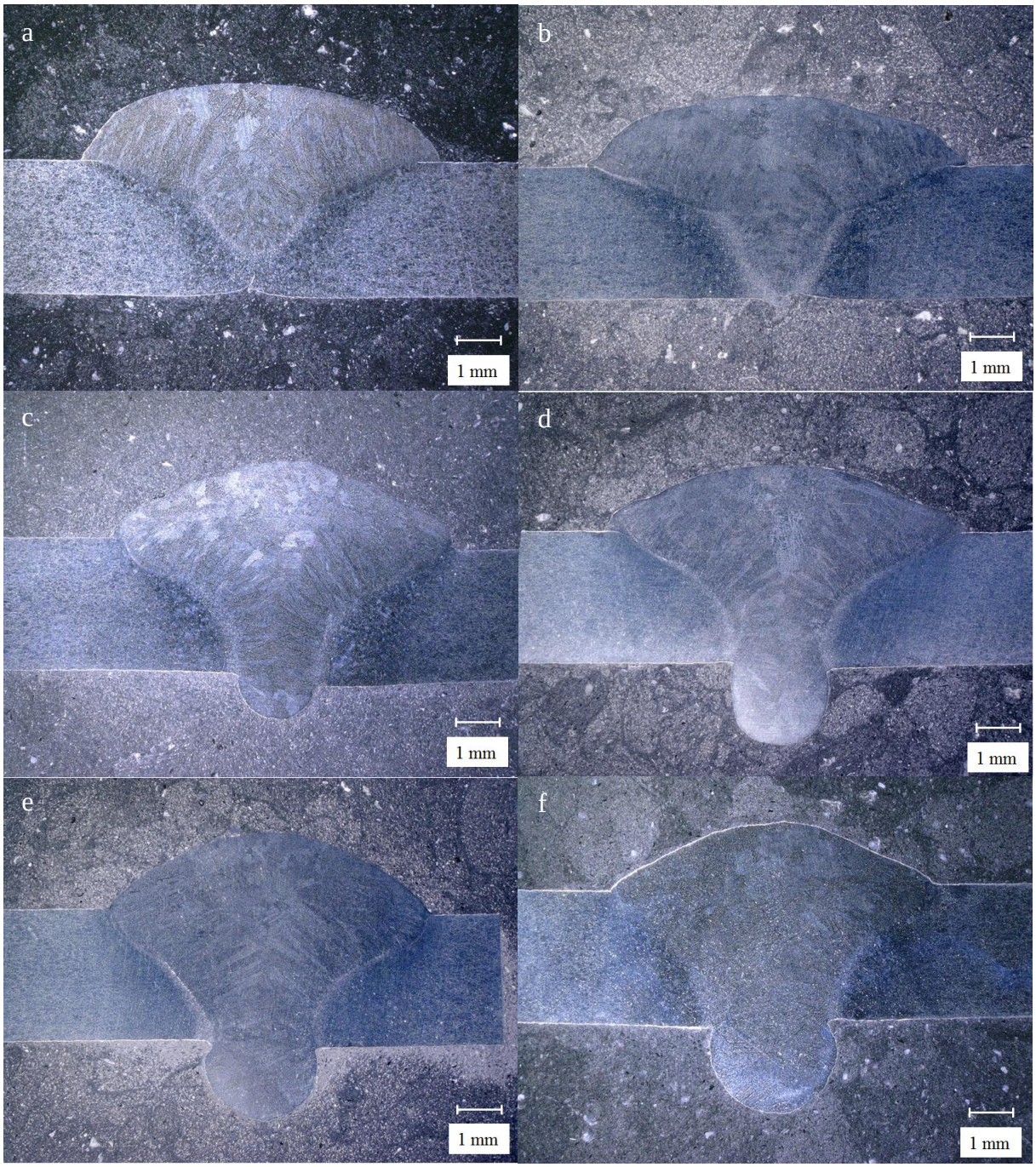

Figure 4-32 The cross-sections of the weld beads obtained in the Ar-He mixtures: (a) Ar; (b) Ar+20% He;(c) Ar+40% He; (d) Ar+60% He; (e) Ar+80% He; (f) He.

In Figure 4-33, the height, width and depth of the weld beads as a function of the He content are described. As the He content is elevated, the width is gradually reduced while the height is almost maintained in the same level (Figure 4-33 a). Concerning the depth, it can be seen that except for the weld bead in pure Ar, all the others get fully penetrated (Figure 4-33 b). The reinforcement area and the middle fusion area are plotted as a function of the He content in Figure 4-34. In Figure 4-34 a, it is shown that with the He content increased, the top reinforcement area is decreased and the bottom reinforcement area is increased. The total reinforcement area which is close to the theoretical value (12.5 mm^2) is slightly changed. In Figure 4-34 b, it is clear that as the He content is raised, the middle fusion area is continuously enlarged.

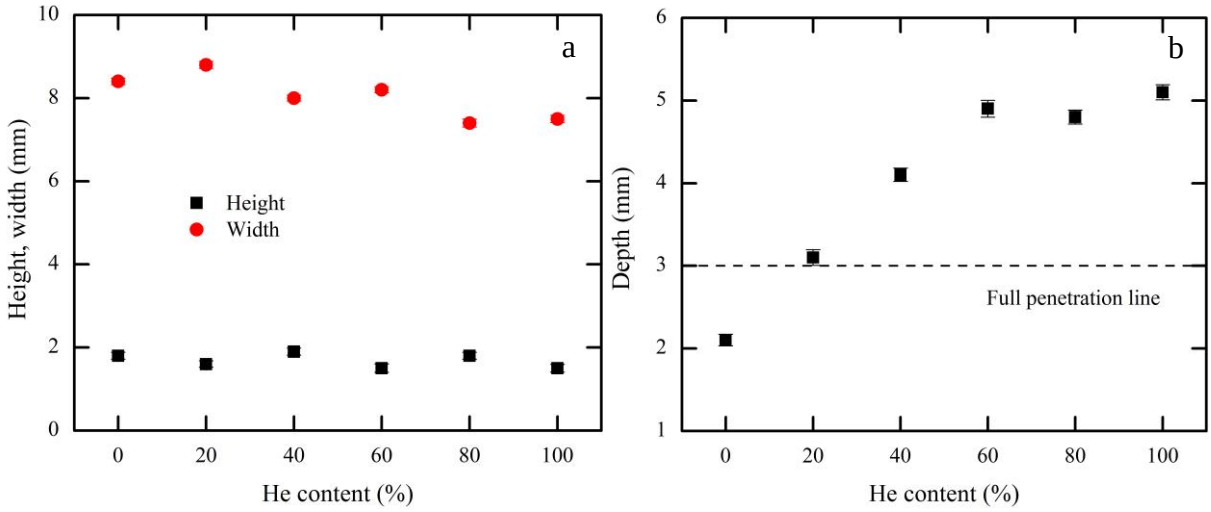

Figure 4-33 The cross-sectional dimensions of the weld bead in Ar-He mixtures: (a) Height and width; (b) Depth.

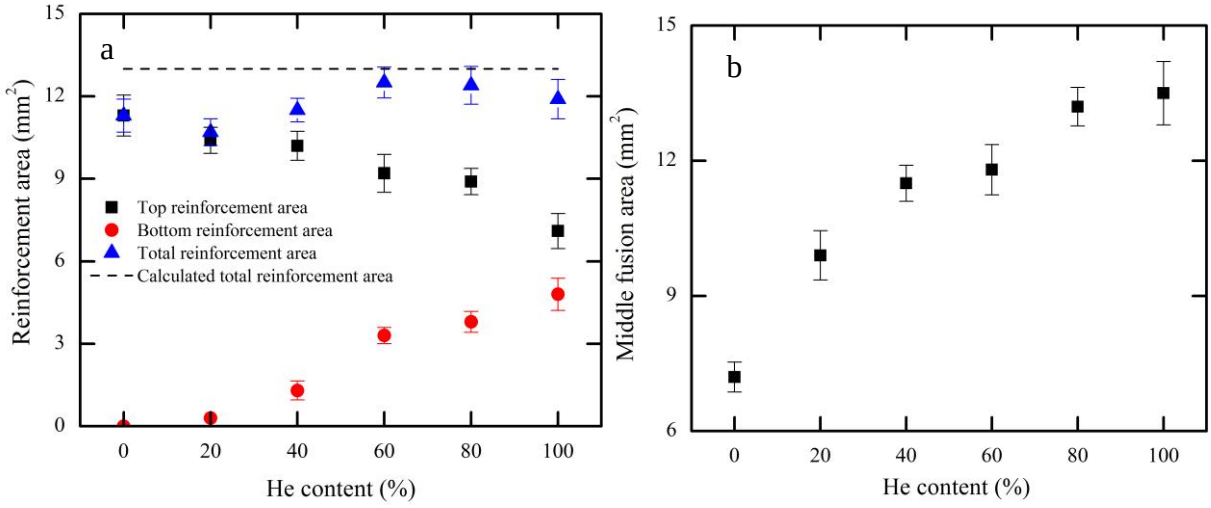

Figure 4-34 The cross-sectional area of the weld bead in Ar-He mixtures: (a) Reinforcement area; (b) Middle fusion area.

Argon, helium and CO_2

The cross-sections of the weld beads in Ar+3.3% CO_2 and Ar+40% He+3.3% CO_2 are presented in Figure 4-35. Comparing Figure 4-35 a with Figure 4-32 a, the weld bead gets fully penetrated with the presence of CO_2. Besides, by comparing Figure 4-35 b with Figure 4-32 c, it can be seen that 3.3% CO_2 makes more materials flow through the workpiece and reach the bottom side. In Figure 4-36, the weld bead geometry in Ar+3.3% CO_2 and Ar+40% He+3.3% CO_2 are quantified. For the convenience of comparison, the cases of Ar and Ar+40% He are presented again. In Figure 4-36 a, it is shown that with 3.3% CO_2 added in the gas mixtures, the weld beads become lower but deeper. In Figure 4-36 b, it can be found that both the bottom reinforcement area and the middle fusion area are enlarged by addition of 3.3% CO_2.

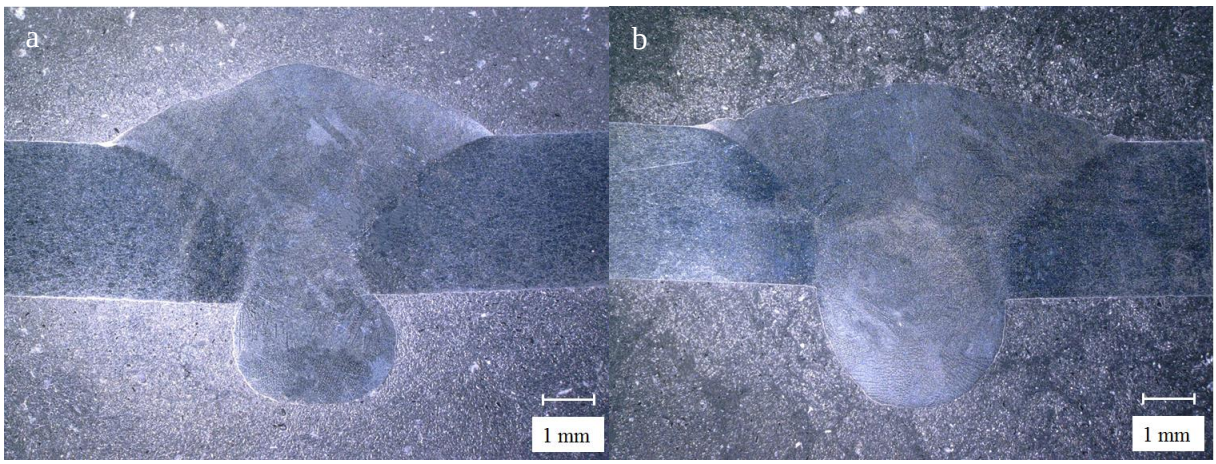

Figure 4-35 The cross-sections of the weld beads in (a) Ar+3.3% CO_2; (b) Ar+40% He+3.3% CO_2.

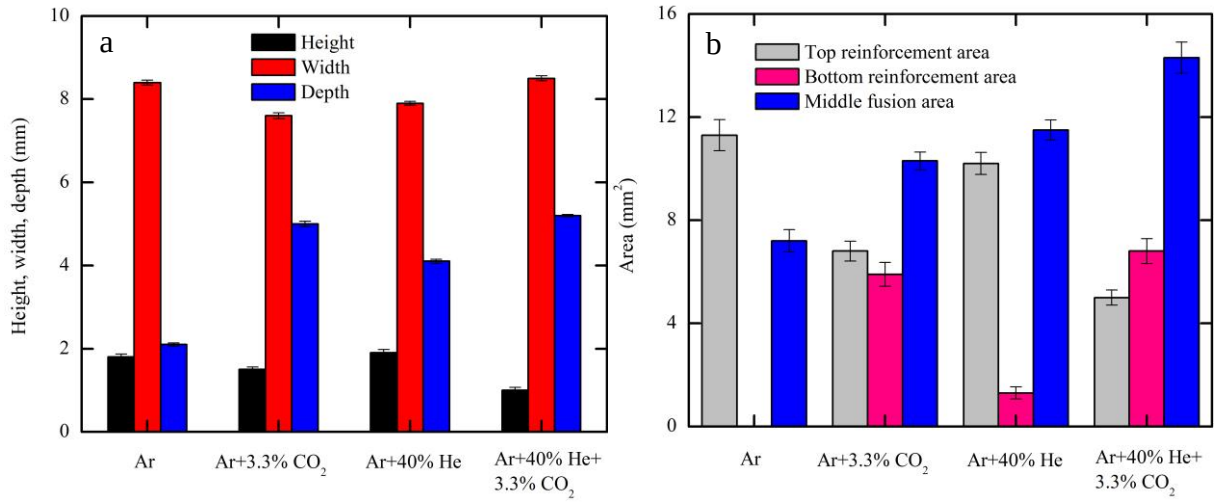

Figure 4-36 The cross-sectional geometry of the weld beads in Ar, Ar+3.3% CO_2, Ar+40% He and Ar+40% He+3.3% CO_2: (a) Dimensions; (b) Area.

Chapter 5. Discussion

In this chapter, attempts are made to explain the experimental results. General features of the short-circuit GMAW of Inconel625 alloy are described. The effects of argon, helium and carbon dioxide on the welding process and weld bead geometry are emphasised.

5.1 Features of the short-circuit GMAW of Inconel625 alloy

Irrespective of the shielding gas composition, some characteristics of short-circuit GMAW of Inconel625 alloy are described and explained in this section. As shown in Figure 4-2, Figure 4-3 and Figure 4-4, short-circuit GMAW is a dynamic process along with the periodical change of voltage and current. The voltage in the arc period is higher than that in the short-circuit period. The welding current keeps growing in the short-circuit period and a maximum is reached, while in the arc period the current drops from the peak to a low value.

In Figure 4-14 and Figure 4-16, it can be seen that the duration of the arc period is larger than that of the short-circuit period. At the wire feed rate of 6 m min^{-1}, the arc period is approximately four times longer than the short-circuit period. Besides, the duration and voltage drop of the short-circuit period are not influenced by the shielding gas composition and the wire feed rate applied (Figure 4-6, Figure 4-10 a, Figure 4-14 and Figure 4-16 a). The effect of the shielding gas composition on short-circuit GMAW is mainly concentrated on the arc period (Figure 4-8 and Figure 4-11).

Figure 4-14 shows that with the wire feed rate increased, the arc period gets shortened while the short-circuit period almost keeps the same. The duration of the entire short-circuit cycle is reduced. Consequently, the short-circuit frequency is increased as shown in Figure 4-15. This can be attributed that as the filler wire is fed at a higher speed, *i.e.* more metal needs to be deposited on the workpiece per unit time, the frequency of the metal transfer becomes higher. The standard deviations of the arc time and the short-circuit time in all the short-circuit cycles can be used to indicate the process regularity. In Figure 4-17, it is shown that with an increase of the wire feed rate, the standard deviation of the arc time drops while that of the short-circuit time stays nearly unchanged. Thus, it is demonstrated that as the wire feed rate is increased, the similarity among all the arc periods is increased which means the process becomes more regular.

5.2 Argon-helium shielding gas

In this section, some remarkable results obtained in Ar, He and Ar-He shielding gas mixtures are analysed. The comparison between Ar and He is always made under the same welding parameters and configuration.

5.2.1 Arc voltage

Comparing Figure 4-6 a with Figure 4-6 b or seeing Figure 4-28, it can be found that at the same wire feed rate, the arc voltage of He is higher than that of Ar. This is because the first ionisation energy of He is 24.58 eV, much larger than that of Ar (15.75 eV) [25]. To achieve ionisation, He requires more energy than Ar. A higher ionisation energy of He also means that a higher arc voltage is necessary for He to trigger and maintain the arc plasma.

However, it should be noted that in arc welding, the arc voltage is directly related to the arc length for a specific shielding gas composition. In other words, for a certain shielding gas, an increased arc length can also lead to an increased arc voltage. With regard to the results in Figure 4-6, it can be argued that besides the higher ionisation potential, the higher arc voltage obtained in He may be also attributed that the arc in He is longer than that in Ar. Therefore, it is necessary to clarify the influence of the change of arc length. In short-circuit GMAW, a short-circuit cycle consists of an arc period and a short-circuit period. In the arc period, it can be thought that the filler wire is fed in a constant speed and the arc length gets shortened gradually (Figure 5-1). The maximal arc length can be roughly calculated by multiplying the wire feed rate by the arc time.

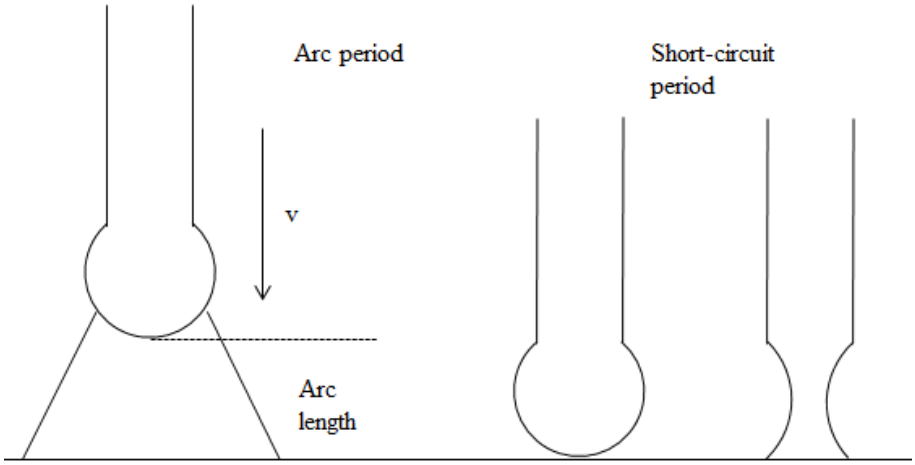

Figure 5-1 Schematic presentation of the local arc area.

As shown in Figure 4-14 a and b, in the bead-on-plate welding at the wire feed rate of 6 m min^{-1}, the arc time in Ar is 18.1 ms while the arc time in He is 17.3 ms. The maximal arc length in Ar is approximately 1.81 mm while that in He is approximately 1.73 mm. It means that in this case, the arc length of He is approximately equal to that of Ar. In Figure 4-6, at the wire feed rate of 6 m min^{-1}, the arc voltage of He is 24.9 V while that of Ar is 15.9 V. It can be demonstrated that compared with Ar, the higher arc voltage of He is due to the higher ionisation potential rather than the change of arc length. Moreover, the results from the butt welding can lead to the same statement. In the butt welding at the wire feed rate of 6 m min^{-1}, the arc voltage of He is 24.1 V while that of Ar is 15.3 V (Figure 4-28 a). The arc time of all the Ar-He mixtures is close to 16.5 ms (Figure 4-30 a), which means the arc length in the Ar-He gas mixtures are similar. The influence of the arc length on the arc voltage can be neglected in this case.

5.2.2 Fusion area

In Figure 4-22 b, it can be seen that at the same wire feed rate, the fusion area of He is larger than that of Ar. This is attributed that in comparison with Ar, the higher arc voltage of He leads to more energy produced by the He arc plasma (Figure 4-9). However, it should be mentioned that what largely determines the size of the fusion zone is the amount of heat transferred to the workpiece rather than the amount of heat generated by the arc plasma. The amount of heat entering the workpiece is equal to the product of the heat generated by the arc and the arc/process efficiency η_p. To verify that more heat is transferred from the He arc to the workpiece, the temperature measurement was performed. In Figure 4-13 a and b, it can be seen that the maximal temperature of the workpiece bottom in He (1146.7±2.2 °C) is higher than that in Ar (1024.3±2.2 °C). Therefore, it can be demonstrated that compared with Ar, more heat is transferred from the He arc to the workpiece which makes the fusion area larger.

5.2.3 Angle θ_1 and θ_2

In the beginning, it should be stated that the angle θ_1 can serve as an important indication of the weld quality. In multi-pass welding, if θ_1 is less than 90° in the root pass, there is a high chance of defects such as porosity and cracks in the subsequent passes. In Figure 4-25 a, it can be seen that at the wire feed rate of 6 and 7 m min^{-1}, θ_1 in Ar are 66° and 75° while those in He are 88° and 96° respectively. It means that at a relatively low wire feed rate, the risk of defects in Ar is higher than that in He. With regard to the angle θ_2, it can indicate the magnitude of the heat transferred from the heat source to the workpiece to some extent. As shown in Figure 4-19 and Figure 4-25 b, θ_2 in Ar stays at 180°. It means that the heat input in Ar is low. As the liquid flow from the centre of the weld pool to the edge, the liquid solidifies immediately and the base metal under the edge of the weld pool is not melted.

Nevertheless, θ_2 in He is smaller than 180° and reduced as the wire feed rate is elevated (Figure 4-20 and Figure 4-25 b). As the liquid flows to the fringe of the weld pool, the base metal is melted. It is indicated that in comparison with Ar, the heat input in He is higher.

5.3 Argon-carbon-dioxide shielding gas

In this section, the experimental results obtained in Ar-CO_2 gas mixtures are analysed. The comparison between Ar and Ar-CO_2 mixtures is always made under the same welding parameters and configuration.

5.3.1 Arc voltage

In Figure 4-10 a, it can be seen that in the bead-on-plate welding at the wire feed rate of 8 m min^{-1}, the arc voltage in Ar+3.3% CO_2 is 20.7 V, higher than that of Ar (16.8 V). This is because at about 3500 K, CO_2 molecule can dissociate and release carbon monoxide and free oxygen atoms. The dissociation requires extra energy, which results in a higher arc voltage in Ar-CO_2 arc plasma compared with the Ar arc plasma. To clarify the influence of the arc length on the arc voltage, the duration of the arc period needs to be considered. In Figure 4-16 a, it can be seen that in the bead-on-plate welding at the wire feed rate of 8 m min^{-1}, the arc time in Ar+3.3% CO_2 is 10.2 ms while that in Ar is 11.0 ms. The calculated maximal arc length in Ar+3.3% CO_2 is approximately 1.36 mm which is slightly lower than that in Ar (1.45 mm). It should be mentioned again that for a specific shielding gas, an increase of the arc length results in an increased arc voltage. Although the arc in Ar+3.3% CO_2 is slightly shorter than that in Ar, the arc voltage in Ar+3.3% CO_2 is nearly 4 V larger than that in Ar. It can be demonstrated that compared with Ar, the higher arc voltage of Ar+3.3% CO_2 is due to the extra dissociation energy of CO_2 rather than the change of arc length.

5.3.2 Penetration and fusion area

As shown in the results of both the bead-on-plate welding (Figure 4-24) and butt welding (Figure 4-36), two tendencies are distinct. Firstly, the penetration of the weld bead in the Ar-CO_2 gas mixture is much deeper than that in Ar. Secondly, with the presence of 3.3% CO_2, the fusion area gets enlarged. A direct reason for them is that comparing the Ar-CO_2 arc with the Ar arc, more energy is transferred from the heat source to the workpiece. As indicated in the temperature measurement (Figure 4-13 a and c), more heat in Ar+3.3% CO_2 reaches the bottom of the workpiece. Moreover, it can be found in Figure 4-12 that relative to the Ar arc, more heat is generated by the Ar-CO_2 arc.

A potential reason can be the presence of oxygen dissociated from CO_2 molecules. It has been stated by many researchers that the surface active elements such as O, S, Se and Te can significantly reduce the surface tension of the liquid metal, which can change the direction of the Marangoni convection from outward and upward to inward and downward (Section 2.4.2) [30, 62, 71, 74, 79-81]. The major elements in the Inconel625 alloy are nickel and chromium. Keene *et al.* [82, 83], Sahoo *et al.* [77] and SanSoucie *et al.* [84] reported the surface tension of the pure nickel and the nickel-oxygen system. Sahoo *et al.* [77] reported the surface tension of the pure chromium and the chromium-oxygen system. It was found that the surface tension of both nickel and chromium could be significantly reduced by oxygen and the temperature gradient of the surface tension would be changed from negative to positive. As a result, the inward, downward Marangoni convection appears.

As a certain amount of heat reaches the top surface of the workpiece, it will be transferred through the workpiece via conduction and convection [55]. The convections driven by the surface tension force, the electromagnetic force, the impingement of the droplets *etc.* can carry the liquid metal of high temperature to the place of low temperature, which greatly improves the efficiency of the heat transfer. Consequently, the heat distribution in the weld pool and the geometry of the weld bead can be influenced. Back to the cases of Ar and Ar+3.3% CO_2, it can be thought that the inward, downward Marangoni convection induced by CO_2 promotes the hotter liquid on the top surface of the weld pool to flow down to the bottom. Consequently, the penetration is deepened and the fusion area is enlarged.

It should be mentioned that with the presence of CO_2, the decrease of surface tension is not directly verified in this study. Nevertheless, the influence of the inward, downward Marangoni flow which is schematically shown in Figure 5-2 can be indicated by the geometry of the weld bead cross-section. In Figure 4-24 a, it can be found that the weld bead with the presence of CO_2 is higher but narrower than that without CO_2. It is evident that the inward Marangoni convection impedes the liquid to flow from the centre of the weld pool to the edge. Moreover, comparing Figure 4-23 with Figure 4-19 c or seeing Figure 4-26, it can be found that the angle θ_1 in both Ar+3.3% CO_2 and Ar+6.7% CO_2 are 41° and 59° respectively, much smaller than that in Ar (89°). This result can also indicate that with the presence of CO_2, the wetting behaviour gets weakened due to the existence of the inward Marangoni convection.

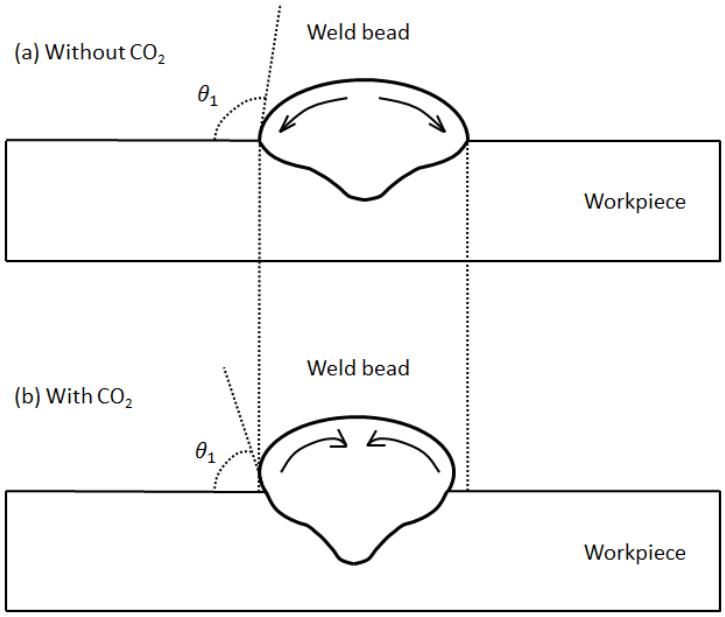

Figure 5-2 Schematic presentation of the influence of CO_2 on the width, height and θ_1.

5.3.3 Short-circuit frequency

Another interesting finding is that with the presence of CO_2, the arc time decreases while the short-circuit frequency is raised (Figure 4-16 and Figure 4-31). This can be attributed that the surface tension of the molten metal is reduced when a certain amount oxygen is dissolved into the liquid droplets. It has been stated that the metal transport is determined by several driving forces such as the surface tension force, electromagnetic force, gravity, the vapour jet force exerted by the arc plasma and the viscous dragging force exerted by the shielding gas flow. In comparison to the globular and spray GMAW, the welding current in short-circuit GMAW is relatively low and the external forces which play a dominant role in the metal transport are the surface tension force and the gravity [85, 86]. Moreover, the gravity acts as the detaching force while the surface tension force tends to hold the droplets against the detachment. As a certain amount of oxygen is dissolved into the liquid droplets, the magnitude of the surface tension force drops which facilitates the droplets to be detached from the electrode and contact the weld pool (Figure 5-3, the dot line). As a consequence, the short-circuit frequency is increased.

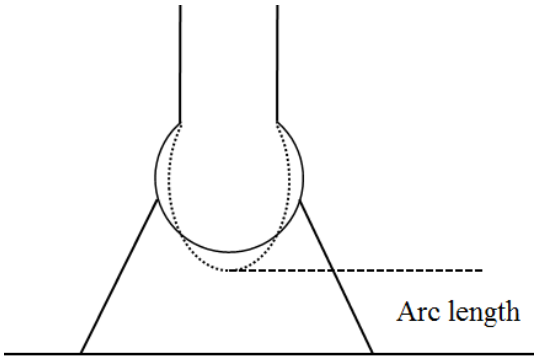

Figure 5-3 Schematic representation of the influence of CO_2 on the droplets.

5.4 Shielding gas selection

Since the effects of Ar, He and CO_2 on the welding process and the geometry of the weld bead cross-section have been revealed, two questions are raised:

1) How to select an appropriate shielding gas during short-circuit GMAW of Inconel625 alloy?
2) How does a pipeline production company benefit from this research?

To answer these two questions, a rough calculation is made. It should be stated at the beginning that the calculation below still needs further validation in the environment of the offshore pipeline production.

As discussed before, an increase of the He content in the shielding gas can lead to a more powerful heat source while the presence of CO_2 can improve the efficiency of the heat transfer from the top surface of the weld pool to the bottom. In Figure 4-32 b and Figure 4-33 b, it can be seen that the joint is fully penetrated and no extra metal flows down by using Ar+20% He. The nominal power of the heat source is $1424\ W$ and the travel/welding speed is 4.3 $mm\ s^{-1}$. The heat generated per unit length of the weld can be calculated:

$$\boldsymbol{H = \frac{P}{V_{travel}} = \frac{1424\ W}{4.3\ mm\ s^{-1}} = 331\ J\ mm^{-1}} \tag{5.1}$$

this calculation indicates that if the heat input is greater than or equal to this critical value ($331\ J\ mm^{-1}$), the weld bead can be fully penetrated. In Figure 4-28 c, it is shown that the maximal power of the heat source can be achieved at $1644.6\ W$ by using Ar+60% He. In Figure 4-32 d and Figure 4-33 b, it can be observed that the weld gets fully penetrated and a certain amount of material even goes down. So, the travel speed can be increased:

$$V_{travel} = \frac{P}{H} = \frac{1645\,W}{331\,J\,mm^{-1}} = 5\ \text{mm}\ s^{-1} \tag{5.2}$$

this calculation indicates that by using Ar+60% He, the travel speed can be increased from 4.3 $mm\ s^{-1}$ to 5 $mm\ s^{-1}$ and the weld can still be fully penetrated. The 16.3% increase of the travel speed means that the welding time can be reduced by 14.0%. It is known that a vessel operation cost is in the order of thousands of euro per day [12]. Some cost can be saved by a decrease of the welding time. In Figure 5-4, the travel speed is plotted as a function of the He content.

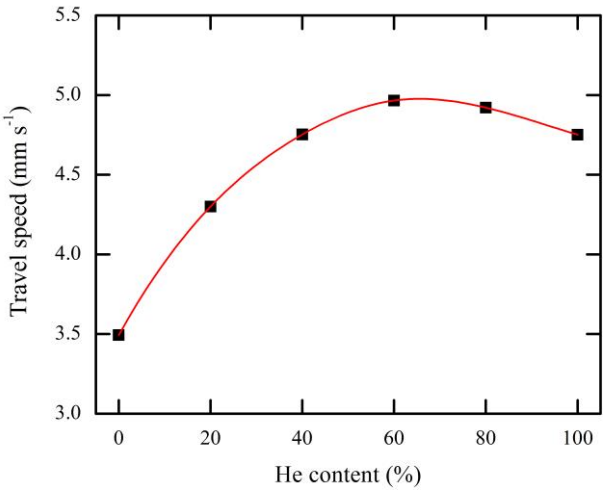

Figure 5-4 The travel speed as a function of the He content at a constant heat input of 331 J mm^{-1}.

Moreover, it is mentioned in Section 1.1 that during welding the Inconel625 lining of the CRA pipes in the root pass, the weld bead is protuberant (Figure 1-1) and an additional grinding procedure is required which is time-consuming and expensive. The cause of the protuberant weld bead is that due to a low travel speed, the metal deposition per unit length of the weld is too high which results in a large top reinforcement area ($A_{reinforcement}$). The top reinforcement area can be calculated by

$$A_{reinforcement} = \frac{V_{wire} \cdot A_{wire} \cdot t}{V_{travel} \cdot t} = \frac{\pi r^2 \cdot V_{wire}}{V_{travel}} \tag{5.3}$$

where V_{wire} is the wire feed rate ($mm\ s^{-1}$), A_{wire} is the cross-sectional area of the filler wire (mm^2), t is the welding time (s), V_{travel} is the travel speed ($mm\ s^{-1}$) and r is the radius of the filler wire (mm). In this thesis, the wire feed rate is 100 $mm\ s^{-1}$ and the radius of the filler wire is 0.5 mm. Equation 5.3 can be simplified as

$$A_{reinforcement} = \frac{78.5}{V_{travel}} \tag{5.4}$$

It can be found that with a constant heat input ($331\ J\ mm^{-1}$), an increased travel speed can lead to a decreased top reinforcement area as described in Figure 5-5. It means that the material deposition per unit length of the weld is reduced while the full penetration can still be achieved. Accordingly, the weld bead can be flattened to a certain extent and the additional grinding procedure is possible to be omitted. Besides, the calculation above which only considers the influence of the He content is a conservative estimation. With a small amount of CO_2 (3.3%), the efficiency of the heat transfer from the top surface of the weld pool to the bottom can be greatly enhanced which means that the travel speed can be increased further.

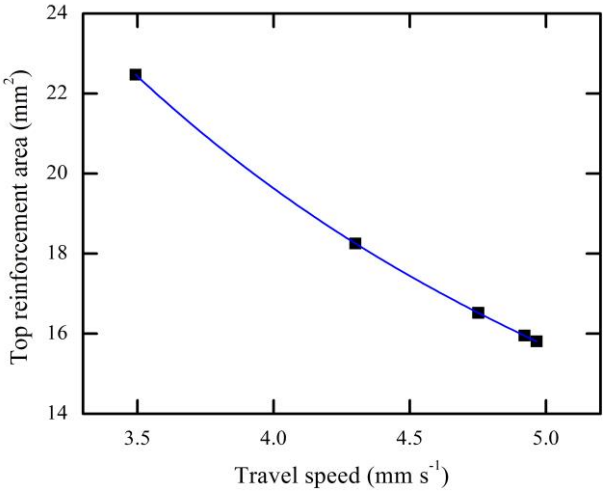

Figure 5-5 The relationship between the top reinforcement area and the travel speed at a constant heat input of 331 J mm^{-1}.

Chapter 6. Conclusions and recommendations

6.1 General conclusions

In this work, the influence of different shielding gas (Ar, He and CO_2) compositions on the welding process and the resultant weld bead geometry during short-circuit GMAW of Inconel625 alloy is studied. On the basis of the results and discussion, the following conclusions can be drawn:

1) Short-circuit GMAW which consists of an arc period and a short-circuit period is a highly dynamic process along with the periodical change of voltage and current. Both average voltage and duration of the arc period are larger than those of the short-circuit period while the average current of arc period is relatively lower. The influence of the change of the shielding gas composition is mainly focused on the arc period but very limited during the short-circuit period.
2) In short-circuit GMAW, wire feed rate is a critical process parameter. With other variables fixed, it determines the material deposition rate and the welding current. The regularity of the short-circuit process can also be greatly influenced by the wire feed rate. An increase of the wire feed rate can lead to a higher regularity.
3) During short-circuit GMAW of Inconel625 alloy with a constant-voltage power source (Fronius^{TM} Transpuls Synergic 5000) used, it is demonstrated that the shielding gas composition can make a great influence on the arc voltage, power of the welding arc, flow motion in the weld pool and the geometry of the weld bead. In the Ar-He shielding gas mixtures, it is found that with an increase of the He content, the arc voltage is elevated. As a result, the heat source (the welding arc) becomes more powerful and more heat is transferred to the workpiece. A larger fusion area is created.
4) For the Ar-CO_2 shielding gas mixtures, it is found that a small quantity of CO_2 (3.3%) can make a great difference on the weld bead geometry. The influence of CO_2 is reflected in two aspects, both of which contribute to a deep penetration and a large fusion area. Firstly, a certain amount of CO_2 can also increase the arc voltage and the power of the welding arc. More importantly, the presence of the surface active element, oxygen which is dissociated from CO_2 can largely reduce the surface tension of the liquid metal. As a consequence, the temperature gradient of the surface tension can be changed from negative to positive and the direction of the Marangoni convection which is driven by the surface tension force will be changed from outward and upward to inward and downward. The efficiency of the heat transfer from the surface of the weld pool to the bottom can be enhanced.

6.2 Recommendations for future work

To begin with, it should be stated that the shielding gas plays an important role in innovations of the arc welding. Depending on the application, an appropriate selection of the shielding gas composition can help to increase the productivity. In this research, some interesting and beneficial finding has been reported. Nevertheless, some questions about the shielding gas still remains which require the further research. It has been demonstrated that the heat input to the joint can be greatly changed by applying different shielding gas composition. In the metallurgical perspective, the microstructure and quality of the welds can be influenced to some extent and defects may be caused. Accordingly, investigation of the effect of the shielding gas composition on the microstructure turns out to be meaningful.

Bibliography

1. Norrish, J., *Advanced welding processes*. 2006: Elsevier.
2. Palmer, A.C. and R.A. King, *Subsea pipeline engineering*. 2004: PennWell Books.
3. Jenney, C. and A. O'Brien, *AWS Welding Handbook, Second Edition.* 2011. **Volume 2**.
4. Murphy, A., et al., *A computational investigation of the effectiveness of different shielding gas mixtures for arc welding.* Journal of Physics D: Applied Physics, 2009. **42**(11): p. 115205.
5. Jönsson, P., T. Eagar, and J. Szekely, *Heat and metal transfer in gas metal arc welding using argon and helium.* Metallurgical and Materials Transactions B, 1995. **26**(2): p. 383-395.
6. Kou, S., *Welding metallurgy, Second Edition*. 2003: Cambridge Univ Press.
7. Murphy, A.B., et al., *Modelling of thermal plasmas for arc welding: the role of the shielding gas properties and of metal vapour.* Journal of Physics D: Applied Physics, 2009. **42**(19): p. 194006.
8. Weman, K., *Welding processes handbook*. 2011: Elsevier.
9. Jones, L., T. Eagar, and J. Lang, *Images of a Steel Electrode in Ar-2% O~ 2 Shielding during Constant Current Gas Metal Arc Welding.* WELDING JOURNAL-NEW YORK-, 1998. **77**: p. 135-s.
10. Kim, Y. and T. Eagar, *Metal transfer in pulsed current gas metal arc welding.* Welding Journal, 1993. **72**(7): p. 279s-287s.
11. Praveen, P., P. Yarlagadda, and M.-J. Kang, *Advancements in pulse gas metal arc welding.* Journal of Materials Processing Technology, 2005. **164**: p. 1113-1119.
12. Yudodibroto, B., *Liquid metal oscillation and arc behaviour during welding*. 2010: TU Delft, Delft University of Technology.
13. Lancaster, J.F., *The physics of welding.* Physics in technology, 1984. **15**(2): p. 73.
14. Hermans, M.J.M., *A study of short circuiting arc welding*. 1997: TU Delft, Delft University of Technology.
15. Kim, I., et al., *A study on relationship between process variables and bead penetration for robotic CO 2 arc welding.* Journal of Materials Processing Technology, 2003. **136**(1): p. 139-145.
16. Karadeniz, E., U. Ozsarac, and C. Yildiz, *The effect of process parameters on penetration in gas metal arc welding processes.* Materials & design, 2007. **28**(2): p. 649-656.
17. Gery, D., H. Long, and P. Maropoulos, *Effects of welding speed, energy input and heat source distribution on temperature variations in butt joint welding.* Journal of Materials Processing Technology, 2005. **167**(2): p. 393-401.
18. Rampaul, H., *Pipe welding procedures*. 2003: Industrial Press.

19. Lu, F., et al., *Analysis of energy flow in gas metal arc welding processes through self-consistent three-dimensional process simulation.* International Journal of Heat and Mass Transfer, 2014. **68**: p. 215-223.
20. Tanaka, M., S. Tashiro, and J. Lowke, *Predictions of weld formation using gas tungsten arcs for various arc lengths from unified arc-electrode model.* Science and Technology of Welding and Joining, 2007. **12**(1): p. 2-9.
21. Dong, W., et al., *GTAW liquid pool convections and the weld shape variations under helium gas shielding.* International Journal of Heat and Mass Transfer, 2011. **54**(7): p. 1420-1431.
22. Liao, M. and W. Chen, *The effect of shielding-gas compositions on the microstructure and mechanical properties of stainless steel weldments.* Materials chemistry and physics, 1998. **55**(2): p. 145-151.
23. Ebrahimnia, M., et al., *Study of the effect of shielding gas composition on the mechanical weld properties of steel ST 37-2 in gas metal arc welding.* Materials & Design, 2009. **30**(9): p. 3891-3895.
24. Irving, B., *Shielding gases are the key to innovations in welding.* Welding journal, 1999. **78**(1): p. 37-41.
25. Williams, M., *CRC Handbook of Chemistry and Physics.* Occupational and environmental medicine, 1996. **53**(7): p. 504.
26. Tanaka, M., et al., *Numerical study of a free-burning argon arc with anode melting.* Plasma Chemistry and Plasma Processing, 2003. **23**(3): p. 585-606.
27. Murphy, A.B., *Transport coefficients of helium and argon-helium plasmas.* Plasma Science, IEEE Transactions on, 1997. **25**(5): p. 809-814.
28. Tanaka, M., et al., *Influence of shielding gas composition on arc properties in TIG welding.* Science and Technology of Welding and Joining, 2008. **13**(3): p. 225-231.
29. Vesel, A., et al., *Dissociation of CO 2 molecules in microwave plasma.* Chemical Physics, 2011. **382**(1): p. 127-131.
30. Mills, K., et al., *Marangoni effects in welding.* Philosophical Transactions-Royal Society of London Series A Mathematical Physical and Engineering Sciences, 1998: p. 911-926.
31. Zhao, C., et al., *The effect of oxygen on transitional Marangoni flow in laser spot welding.* Acta Materialia, 2010. **58**(19): p. 6345-6357.
32. Wang, L., et al., *Effects of shielding gas composition on arc profile and molten pool dynamics in gas metal arc welding of steels.* Journal of Physics D: Applied Physics, 2014. **47**(46): p. 465202.
33. Pires, I., L. Quintino, and R. Miranda, *Analysis of the influence of shielding gas mixtures on the gas metal arc welding metal transfer modes and fume formation rate.* Materials & design, 2007. **28**(5): p. 1623-1631.

34. Hermans, M. and G. Den Ouden, *Process behavior and stability in short circuit gas metal arc welding.* WELDING JOURNAL-NEW YORK-, 1999: p. 137-s.
35. Maruo, H., Y. Hirata, and N. Goto, *Bridging transfer phenomena of conductive pendent drop.* YOSETSU GAKKAI RONBUNSHU., 1992. **10**(2): p. 43-50.
36. Adolfsson, S., et al., *On-line quality monitoring in short-circuit gas metal arc welding.* WELDING JOURNAL-NEW YORK-, 1999. **78**: p. 59-s.
37. Goldsmid, H.J., *Introduction to thermoelectricity*. Vol. 121. 2009: Springer Science & Business Media.
38. Murphy, A.B., *A self-consistent three-dimensional model of the arc, electrode and weld pool in gas–metal arc welding.* Journal of Physics D: Applied Physics, 2011. **44**(19): p. 194009.
39. Hu, J. and H.-L. Tsai, *Heat and mass transfer in gas metal arc welding. Part II: The metal.* International Journal of Heat and Mass Transfer, 2007. **50**(5): p. 808-820.
40. Haidar, J. and J. Lowke, *Predictions of metal droplet formation in arc welding.* Journal of Physics D: Applied Physics, 1996. **29**(12): p. 2951.
41. Waszink, J.H. and L. Graat, *Experimental investigation of the forces acting on a drop of weld metal.* Welding Journal, 1983. **62**(4): p. S108-S116.
42. Rhee, S. and E. Kannatey-Asibu, *Observation of metal transfer during gas metal arc welding.* WELDING JOURNAL-NEW YORK-, 1992. **71**: p. 381-s.
43. Jones, L., T. Eagar, and J. Lang, *Magnetic forces acting on molten drops in gas metal arc welding.* Journal of Physics D: Applied Physics, 1998. **31**(1): p. 93.
44. Suban, M., *Determination of stability of MIG/MAG welding processes.* Quality and Reliability Engineering International, 2001. **17**(5): p. 345-353.
45. Fridman, A., *Plasma chemistry*. 2008: Cambridge university press.
46. Hoyaux, M.F., *Arc physics*. Vol. 8. 2013: Springer Science & Business Media.
47. Heberlein, J., J. Mentel, and E. Pfender, *The anode region of electric arcs: a survey.* Journal of Physics D: Applied Physics, 2009. **43**(2): p. 023001.
48. Hu, J. and H.-L. Tsai, *Heat and mass transfer in gas metal arc welding. Part I: The arc.* International Journal of Heat and Mass Transfer, 2007. **50**(5): p. 833-846.
49. Murphy, A., *Diffusion in equilibrium mixtures of ionized gases.* Physical Review E, 1993. **48**(5): p. 3594.
50. Rao, Z., et al., *Modeling of the transport phenomena in GMAW using argon–helium mixtures. Part I–The arc.* International Journal of Heat and Mass Transfer, 2010. **53**(25): p. 5707-5721.
51. Nemchinsky, V.A., *The effect of the type of plasma gas on current constriction at the molten tip of an arc electrode.* Journal of Physics D: Applied Physics, 1996. **29**(5): p. 1202.
52. Tanaka, M., et al., *CO 2-shielded arc as a high-intensity heat source.* Vacuum, 2006. **80**(11): p. 1195-1198.

53. Oreper, G. and J. Szekely, *Heat-and fluid-flow phenomena in weld pools.* Journal of Fluid Mechanics, 1984. **147**: p. 53-79.
54. Kou, S. and Y. Wang, *Weld pool convection and its effect.* Weld. J, 1986. **65**(3): p. 63s-70s.
55. Kou, S. and D. Sun, *Fluid flow and weld penetration in stationary arc welds.* Metallurgical Transactions A, 1985. **16**(2): p. 203-213.
56. Fan, H., H.-L. Tsai, and S. Na, *Heat transfer and fluid flow in a partially or fully penetrated weld pool in gas tungsten arc welding.* International Journal of Heat and Mass Transfer, 2001. **44**(2): p. 417-428.
57. Hu, J., H. Guo, and H.-L. Tsai, *Weld pool dynamics and the formation of ripples in 3D gas metal arc welding.* International Journal of Heat and Mass Transfer, 2008. **51**(9): p. 2537-2552.
58. DebRoy, T. and S. David, *Physical processes in fusion welding.* Reviews of Modern Physics, 1995. **67**(1): p. 85.
59. Oreper, G., T. Eagar, and J. Szekely, *Convection in arc weld pools.* Welding journal, 1983. **62**(11): p. 307-312.
60. Wang, Y. and H.-L. Tsai, *Impingement of filler droplets and weld pool dynamics during gas metal arc welding process.* International Journal of Heat and Mass Transfer, 2001. **44**(11): p. 2067-2080.
61. Tsai, M. and S. Kou, *Weld pool convection and expansion due to density variations.* Numerical heat transfer, 1990. **17**(1): p. 73-89.
62. Zhao, C., *Measurements of fluid flow in weld pools*. 2011: TU Delft, Delft University of Technology.
63. Eisazadeh, H., D.J. Haines, and M. Torabizadeh, *Effects of gravity on mechanical properties of GTA welded joints.* Journal of Materials Processing Technology, 2014. **214**(5): p. 1136-1142.
64. Tsai, M. and S. Kou, *Electromagnetic-force-induced convection in weld pools with a free surface.* Welding Journal, 1990. **69**(6): p. 241s-246s.
65. Limmaneevichitr, C. and S. Kou, *Experiments to simulate effect of Marangoni convection on weld pool shape.* WELDING JOURNAL-NEW YORK-, 2000. **79**(8): p. 231-S.
66. Tsai, M. and S. Kou, *Marangoni convection in weld pools with a free surface.* International Journal for Numerical Methods in Fluids, 1989. **9**(12): p. 1503-1516.
67. Zhang, W., *Probing heat transfer, fluid flow and microstructural evolution during fusion welding of alloys*. 2004, The Pennsylvania State University.
68. Tseng, K.-H. and C.-Y. Hsu, *Performance of activated TIG process in austenitic stainless steel welds.* Journal of Materials Processing Technology, 2011. **211**(3): p. 503-512.
69. Wang, Y. and H.-L. Tsai, *Effects of surface active elements on weld pool fluid flow and weld penetration in gas metal arc welding.* Metallurgical and Materials Transactions B, 2001. **32**(3): p. 501-515.

70. Lu, S., H. Fujii, and K. Nogi, *Arc ignitability, bead protection and weld shape variations for He–Ar–O 2 shielded GTA welding on SUS304 stainless steel.* Journal of materials processing technology, 2009. **209**(3): p. 1231-1239.
71. Lu, S., H. Fujii, and K. Nogi, *Marangoni convection and weld shape variations in Ar–O 2 and Ar–CO 2 shielded GTA welding.* Materials science and engineering: A, 2004. **380**(1): p. 290-297.
72. Rodrigues, A. and A. Loureiro, *Effect of shielding gas and activating flux on weld bead geometry in tungsten inert gas welding of austenitic stainless steels.* Science and Technology of Welding and Joining, 2005. **10**(6): p. 760-765.
73. Aidun, D. and S. Martin, *Effect of sulfur and oxygen on weld penetration of high-purity austenitic stainless steels.* Journal of Materials Engineering and Performance, 1997. **6**(4): p. 496-502.
74. Heiple, C. and J. Roper, *Mechanism for minor element effect on GTA fusion zone geometry.* Welding journal, 1982. **61**(4): p. 97.
75. Kuo, M., Z. Sun, and D. Pan, *Laser welding with activating flux.* Science and Technology of Welding & Joining, 2013.
76. Tanaka, M., *Effects of surface active elements on weld pool formation using TIG arcs.* Welding international, 2005. **19**(11): p. 870-876.
77. Sahoo, P., T. DebRoy, and M. McNallan, *Surface tension of binary metal—surface active solute systems under conditions relevant to welding metallurgy.* Metallurgical Transactions B, 1988. **19**(3): p. 483-491.
78. Lippold, J.C., S.D. Kiser, and J.N. DuPont, *Welding metallurgy and weldability of nickel-base alloys*. 2011: John Wiley & Sons.
79. Heiple, C., et al., *Surface active element effects on the shape of GTA, laser and electron beam welds.* Weld. J., 1983. **62**(3): p. 72.
80. Heiple, C. and P. Burgardt, *Effects of SO2 shielding gas additions on GTA weld shape.* Welding journal, 1985. **64**(6): p. 159-162.
81. Jonsson, P., A. Murphy, and J. Szekely, *The influence of oxygen additions on argon-shielded gas metal arc welding processes.* Welding Journal-Including Welding Research Supplement, 1995. **74**(2): p. 48s.
82. Keene, B., *Review of data for the surface tension of pure metals.* International Materials Reviews, 1993. **38**(4): p. 157-192.
83. Keene, B., *Review of data for the surface tension of iron and its binary alloys*. International Materials Reviews, 2013.
84. SanSoucie, M., et al., *Effects of Environmental Oxygen Content and Dissolved Oxygen on the Surface Tension and Viscosity of Liquid Nickel.* International Journal of Thermophysics, 2016. **37**(7): p. 1-11.

85. Kim, Y. and T. Eagar, *Analysis of metal transfer in gas metal arc welding*. WELDING JOURNAL-NEW YORK-, 1993. **72**: p. 269-s.
86. Choi, J.H., J. Lee, and C.D. Yoo, *Dynamic force balance model for metal transfer analysis in arc welding*. Journal of Physics D: Applied Physics, 2001. **34**(17): p. 2658.